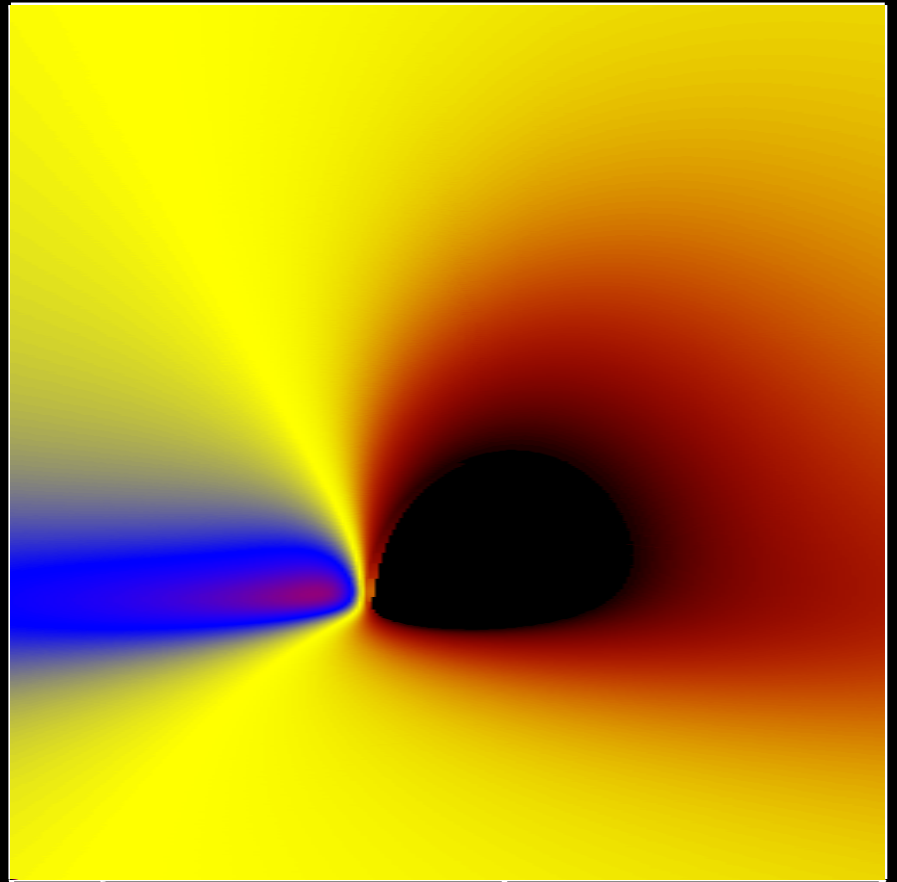

THEORETICAL MODELING OF BROAD EMISSION LINES

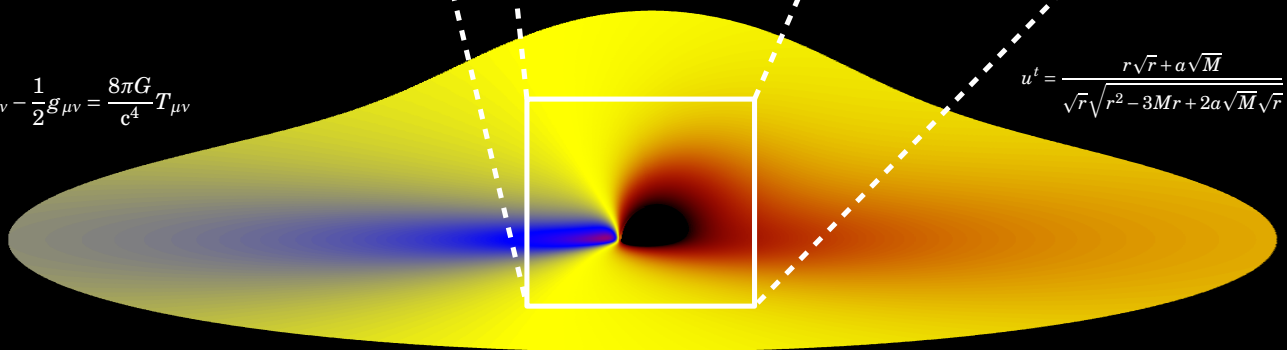
Thomas Dauser

$$ds^2 = \Sigma d\theta^2 - \left(1 - \frac{2Mr}{\Sigma}\right) dt^2$$
$$+ \frac{\Sigma}{\Delta} dr^2 - \frac{4aMr \sin^2 \theta}{\Sigma} dt d\varphi$$
$$+ \left(r^2 + a^2 \frac{2a^2 Mr \sin^2 \theta}{\Sigma}\right) \sin^2 \theta d\varphi^2$$



$$R_{\mu\nu} - \frac{1}{2}g_{\mu\nu} = \frac{8\pi G}{c^4} T_{\mu\nu}$$

$$u^t = \frac{r\sqrt{r} + a\sqrt{M}}{\sqrt{r}\sqrt{r^2 - 3Mr + 2a\sqrt{M}\sqrt{r}}}$$





Dr. Karl Remeis Sternwarte Bamberg
Astronomisches Institut der Universität Erlangen-Nürnberg

DIPLOMARBEIT

THEORETICAL MODELING OF BROAD EMISSION LINES

Thomas Dauser

supervised by
Prof. Dr. Jörn Wilms

Bamberg, 20.12.2010



ERLANGEN CENTRE
FOR ASTROPARTICLE
PHYSICS

**Friedrich-Alexander-Universität
Erlangen-Nürnberg**



Image on the Titlepage: *Simulation of an accretion disk as seen by a distant observer under an inclination angle of $\theta_o = 80^\circ$. The disk is rotating around a maximally fast spinning black hole. The color scheme reflects the direction of the energy shift, i.e., red illustrates a shift to lower energies and blue a shift to higher energies, respectively. The blue shifted left part of the disk moves towards the observer, whereas the right part recedes from the observer. Note how the light bending serves to virtually flip the disk behind the black hole upwards. The asymmetries are due to relativistic light bending.*

CONTENTS

Deutsche Zusammenfassung	1
Abstract	2
1 Introduction to Black Hole Physics	3
1.1 Different Appearances	4
1.2 Accretion	5
1.3 The Spin of a Black Hole	7
1.3.1 Measuring the Spin	8
1.3.2 Current Observational Constraints	8
1.3.3 Negative Spin	9
1.4 The Aim of this Work	11
2 Basic Theory on Spinning Black Holes	12
2.1 Spacetime around Rotating Black Holes	12
2.1.1 The Kerr Metric	12
2.1.2 General Properties	13
2.2 General Equations of Motion	14
2.2.1 The Accretion Disk	16
2.2.2 Photon Trajectories	18
3 Emission from a Thin Accretion Disk	21
3.1 Transfer Function	21
3.1.1 Radiation Transport	21
3.1.2 Transfer Function of Cunningham	24
3.1.3 Numerical Calculation	25
3.2 Imaging the Accretion Disk	27
3.3 Understanding the Line Profile	29
3.4 Negatively Spinning Black Holes	32
3.5 Different Models	35
3.5.1 The laor Model	36
3.5.2 The kyrline Model	37
3.5.3 The kerrdisk Model	37
4 The rcelline Model	39
4.1 Numerical Implementation	39
4.2 Usage in Data Analysis	42
4.3 Comparison to other Models	43
5 The Lamp-Post Geometry	45
5.1 The Equation of Motion	46
5.1.1 Basic Equations	46
5.1.2 Numerical Methods	48

5.2	Photon Trajectories	49
5.3	Disk Illumination	51
5.3.1	Comparison to Flat Space	51
5.3.2	The Energy Shift	54
5.3.3	The Incident Angle	55
6	Conclusions, Ongoing and Future Work	57
6.1	The Broad Emission Line in Cygnus X-1	57
6.2	Constraining Negative Spin	59
6.3	Broad Emission Lines as a Probe for Black Hole Spin	59
6.4	A Self-Consistent Model	61
	Acknowledgments	62
	List of Figures	63
	References	64
	Declaration	67

DEUTSCHE ZUSAMMENFASSUNG

Obwohl Schwarze Löcher sehr exotische Objekte sind, können sie durch nur zwei Parameter beschrieben werden: Ihre Masse und ihren Spin. Wie in dieser Arbeit gezeigt wird, ist die Bestimmung des Spins eine schwierige Aufgabe, deshalb gibt es bis jetzt nur eine Handvoll verlässlicher Messungen. Auch wenn die Bestimmung schwierig ist, spielt der Spin eines Schwarzen Lochs in Theorien zur Galaxienentwicklung und der Entstehung von extrem relativistischen Jets eine wichtige Rolle. Die Verdrillung der Raumzeit durch das sich drehende Schwarze Loch spiegelt sich im beobachteten Photonenspektrum wieder, weshalb man durch spektrale Analyse daraus die Rotation bestimmen kann. Diese Arbeit konzentriert sich auf "relativistisch verbreiterte Emissionslinien" in den Spektren zur Messung des Spins. Diese Emissionslinien entstehen durch Reflektion harter Röntgenstrahlen, die auf die Akkretionsscheibe strahlen und dort fluoreszente Emission hervorrufen. Durch die relativistische Rotation der Akkretionsscheibe bekommt die dünne Emissionslinie eine breite und asymmetrische Form. Diese sehr charakteristische Form hängt von unterschiedlichen Parametern des Systems ab, unter anderem der Inklination, dem Emissionort der harten Röntgenstrahlung, und dem Spin des Schwarzen Lochs.

In dieser Arbeit stelle ich die grundlegenden Gleichungen der Allgemeinen Relativitätstheorie vor, die rotierende Schwarze Löcher in der Kerr Metrik beschreiben. Mit den daraus abgeleiteten Gleichungen können die Bewegung der Teilchen in einer einfachen Akkretionsscheibe und Photon Bahnen numerisch beschrieben werden. Um die relativistischen Effekte die diesen Gleichungen zu eigen sind besser zu veranschaulichen wurden Bilder einer Akkretionsscheibe aus der Sicht eines entfernten Beobachters simuliert. Die Analyse der Linienprofile zeigt, dass sich bei Änderung der Inklination, des Intensitätsprofils der Akkretionsscheibe oder des Spin, sich die Linienform charakteristisch ändert und deshalb theoretisch diese Parameter aus Beobachtungen bestimmt werden können. Außerdem wurden Systeme untersucht, in denen die Akkretionsscheibe entgegen dem Schwarzen Loch rotiert. Emissionslinien solcher Systeme sind systematisch schmaler, obwohl sie trotzdem als breite Linien detektierbar sind. Simulationen zur Beobachtbarkeit ergeben, dass es zukünftigen Weltraumteleskopen wie dem *International X-ray Observatory* möglich sein wird negativen Spin zu detektieren. Bei dem Vergleich bekannter Modelle zur Berechnung breiter Emissionslinien zeigen sich größere Unterschiede: Wohingegen das `laor` Modell größere Probleme hat die korrekte Linienform vorherzusagen, berechnet das `kyrline` Modell ohne Probleme exakte Linienprofile. Da keines der verfügbaren Modelle negativen Spin berücksichtigt, wurde das `relline` Modell erstellt. Es wurde dabei ein flexibler Ansatz mit Greens Funktionen benutzt, der es erlaubt eine beliebige Radial- und Winkelabhängigkeit der emittierten Strahlung zu benutzen. Mit den numerischen Techniken zur Berechnung der Linienformen wurde außerdem eine Quelle der harten Röntgenstrahlung auf der Rotationsachse des Schwarzen Lochs untersucht. Die Simulation ergab, dass die Photon Bahnen umso stärker auf die Akkretionsscheibe fokussiert werden, je niedriger die Quelle der primären Strahlung ist. Des weiteren werden die Photonen um ein Vielfaches ihrer Energie verschoben werden. Außerdem wurde das `relline` Modell verwendet, um eine Beobachtung von Cygnus X-1 zu analysieren. Die vorläufigen Ergebnisse deuten auf ein schnell rotierendes Schwarzes Loch hin.

ABSTRACT

Although black holes are very exotic objects, they can be described by only two parameters: Their mass and their spin. As will be demonstrated in this work, determining the spin of black holes is a difficult task. That is why only few trustworthy measurements exist up to now. Despite all difficulties in detecting it, the spin of a black hole might play an important role in explaining yet not fully understood effects like galaxy evolution or the formation of the most powerful jets. Using the signature that the twisted strong gravity imprints on photons, which are emitted in the vicinity of the black hole, the spin can be determined by spectral analysis. This work focuses on determining the black hole's rotation via the spectral features of "broad emission lines". These emission lines are created when hard X-rays irradiate the accretion disk and induce fluorescent emission of atoms in the disk. Due to the relativistically fast rotation of the accretion disk and the effects of strong gravity, the intrinsically narrow emission line gets broadened and asymmetric. This very characteristic shape depends on several parameters such as the inclination of the system, the location of the hard X-ray source or the spin of the black hole.

In this work I present the basic equations for rotating black holes by solving General Relativity in the Kerr metric. Employing the derived relations, the motion of particles in a simple accretion disk and photon trajectories are calculated, using numerical techniques. In order to illustrate the relativistic effects inherent in the equations, images of an accretion disk as seen by a distant observer are simulated. Interpreting the calculated line profiles, it is shown that varying the inclination angle, the intensity profile of the disk, or the spin of the black hole strongly changes their shape and hence would in principle allow to determine all these parameters from observation. Motivated by galaxy evolution models and theories explaining the most powerful jets, the case of "negative spin", i.e., a counterrotating accretion disk, is analyzed. Emission lines from negatively spinning systems will be narrower, but nevertheless detectable as broad emission lines. Observability simulations show that future X-ray satellites like the *International X-ray Observatory* will be able to detect systems with negative spin. A comparison of popular models for calculating these line shapes shows a large discrepancy: Whereas the commonly used `laor` model has major problems in predicting the correct line shape, the `kyrline` model easily produces accurate profiles for all parameter combinations. As none of the available models is capable of calculating emission lines for systems with negative spin, a new model, `relline`, was implemented. A more flexible approach using Green's functions was chosen, which allows to take an arbitrary angular and radial dependence of the emitted radiation into account. Additionally, the number of precalculated values is reduced by making use of strong interpolation. Employing the numerical techniques developed for calculating the line profiles, a hard X-ray source located on the rotational axis of the black hole, i.e. the "lamp-post" geometry, is analyzed. It is shown that the simulated photon trajectories are focused more strongly onto the accretion disk for decreasing height of the source and are shifted to several times their energy. Furthermore the `relline` model was used to analyze simultaneous *XMM-Newton* and *RXTE* observations of Cygnus X-1. Preliminary results suggest a rapidly rotating black hole.

CHAPTER 1

INTRODUCTION TO BLACK HOLE PHYSICS

Black holes belong to the most fascinating and exotic objects of the Universe. Although they have only been accepted to exist recently, they were first predicted almost a century ago. Shortly after Albert Einstein published his theory on General Relativity in 1916, Schwarzschild (1916) found the first solution for it. It describes the gravitational field of a point mass. The most interesting part of this solution is the existence of a region around this central point, where the effect of gravity is so strong that not even photons can escape beyond it. As this implies that nothing else, no information which ever gets beyond this radius, can escape, it is called the “Event Horizon” and the object itself a “Black Hole”. The horizon scales linearly with the mass contained inside this radius, also called “Schwarzschild radius”, according to

$$r_S = \frac{2GM}{c^2} \approx 3 \text{ km} \frac{M}{M_\odot} \quad , \quad (1.1)$$

where M_\odot is the mass of our Sun. Hence, it is in principle possible for any object to become a black hole, one only needs to find a way to compress it to a size smaller than its event horizon. For our Sun this would imply squeezing it to a radius of 3 km, which is only 0.0004 % of its current size. Thus it is understandable that people were doubtful about the existence of such black holes in our Universe.

The first black hole was not discovered before people began observing the sky with X-ray detectors. The reason as we know now is simple: Some black holes are not “black”, but emit X-rays due to a process called “accretion”. How this process works will be explained in Sec. 1.2. As our atmosphere is not transparent for X-rays, people needed to find a way to bring the detectors in large heights to be able to observe X-rays. The first black hole, Cygnus X-1, was observed more than 40 years ago with *Aerobee* rockets (Bowyer et al., 1965), but without identifying it as such an object. First hints on its true origin came from balloon experiments by Dolan (1970), who discovered variabilities in flux on extremely short timescales. But in order to really quantify this behavior, the first X-ray satellite *UHURU* (Giacconi et al., 1972) was needed, which provided the first long-term observations of the X-ray sky. From the fact that a large amount of the flux was observed to vary on 70 ms timescales, Oda et al. (1971) calculate that the emitting region is smaller than 1 Astronomical Unit¹ (AU). Because the pulsations were persistent, they concluded that rotation has to be the driving mechanism for these variations. Therefore Oda et al. (1971) suggested that the radiation has to originate from a rapidly

¹ 1 AU $\approx 1.5 \cdot 10^8$ km

rotating “X-ray star”, containing either a neutron star or a black hole, as any star would have to collapse due to such an extreme rotation. Still many uncertainties remained, such as the identification of the optical counterpart of the X-ray source feeding it with energy. Radio measurements of Cygnus X-1 determined its position more accurately than X-ray observations (Braes & Miley, 1971; Hjellming & Wade, 1971) and allowed to identify the optical companion by extensive optical monitoring (Murdin & Webster, 1971; Bolton, 1972) to be HDE 226868. With radial velocity measurements of the companion star, Webster & Murdin (1972) finally identified the whole system to be a spectroscopy binary and the X-ray source to have at least twice the mass of the Sun. Based on these results, the authors speculated that this source might indeed be a black hole. In the following years this picture of Cygnus X-1 slowly got accepted by the astronomical community (see, e.g., Shipman, 1975). Thanks to modern space telescopes like *Chandra*, *XMM-Newton* and *Suzaku*, many black holes are nowadays known and most astronomers consider their existence to be proven.

1.1 DIFFERENT APPEARANCES

Although it is stated above that any mass compressed strongly enough can become a black hole, there are mainly two different kinds of black holes known. This can simply be explained with the enormous necessary for creating black holes, making it hard to find a suitable mechanism. Galactic black holes (GBHs), like Cygnus X-1, usually have only a few solar masses. They are created, when a massive star explodes in a supernova at the end of its life. The GBHs are mainly observed in binary systems, i.e., they orbit a companion star, which feeds them with matter they can accrete. Additionally, both types of black holes can also be seen indirectly when they pass in front of a luminous background object. In this case the black hole acts as a “gravitational lens” and distorts the image of the background source, as the photons are deflected when passing by close to the gravitating object (Einstein, 1936). The distorted image allows to derive properties of the lensing object, i.e., the black hole in this case.

The other group of black holes are called the supermassive black holes (SMBHs), as they are found to have a million to billion times the solar mass. The black hole at the center of our Galaxy, identified with the radio source Sgr A*, belongs to this group. All of the SMBHs have been found in the center of galaxies. Some of these black holes exhibit a bright high-energy output, and are therefore called Active Galactic Nuclei (AGN). In contrast to black holes like Sgr A*, these are usually very bright all over the electromagnetic spectrum from radio to TeV energies and can be observed even at very large distances. How SMBHs are created is not as well known as for their galactic companions. At least there is strong evidence that the mass of the black hole scales with luminosity of the host galaxy’s bulge and therefore the formation and evolution of the galaxy and the black hole is closely linked (Ferrarese & Merritt, 2000). As the most luminous AGNs are found at redshift $z \approx 2$ and not today (Richards et al., 2006) and not many candidates for intermediate mass black holes are known, a linear hierarchical growth from stellar mass black holes to SMBH seems to be unlikely. Either the SMBHs holes are formed from GBHs in runaway processes of different kinds (Rees, 1984; Begelman et al., 2006) or the deep gravitational potentials of dark matter clumps, originating from density fluctuations after the Big Bang, trigger the formation of supermassive black holes. Recent simulations like the “Millenium Simulation” (Springel et al., 2005) result at least in universes with structures very similar to our own, by simulating the cosmic dark matter evolution after the Big Bang.

Despite their huge difference in mass, the GBHs and the SMBHs have a lot in common (see

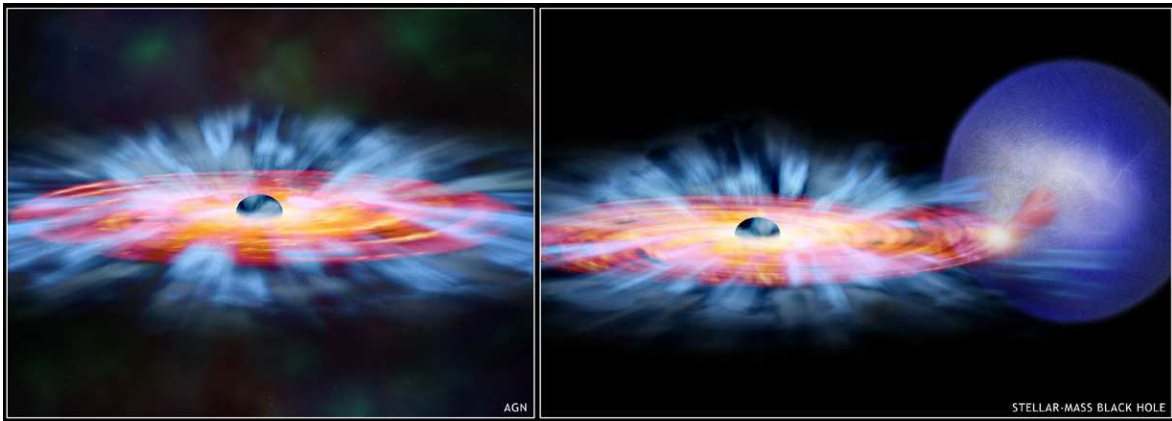


Fig. 1.1: An artist’s impression of an AGN (left) and a GBH (right). It illustrates the similarity between these two objects, although the mass and therefore the length scales are a million times greater in the left image. (Credits: <http://chandra.harvard.edu/>)

Fig. 1.1 for an illustration). First, they are described both by the same mathematical solution of Einstein’s Field Equation. Moreover the “no-hair theorem” of General Relativity predicts that black holes can be described by very few parameters, namely only the mass, the spin, and the electric charge (Carter, 1971; Misner et al., 1973). As our Universe is observed to be almost electromagnetically neutral, the only two parameters that characterize a black hole are its mass and its angular momentum. Therefore the largest apparent difference between the galactic and the supermassive black holes is a (large) factor in mass². But as the solution is valid for both types, we would not expect the physics and the processes in these objects to differ. A greater mass of the black hole only implies that the event horizon grows by the same factor. It is expected that the variability timescales are larger by an equal factor. Hence, we would expect average spectra of GBHs and SMBHs to be very similar. Clearly, there exist some effects (e.g., warm absorbers in AGNs or wind from the companion star in GBHs) only due to the different environment in binary systems and active galaxies, but in general, the same effects are observed.

1.2 ACCRETION

The process of accretion is responsible for the energy release in GBHs (Shakura & Sunyaev, 1973) and AGN (Rees, 1984). The following facts and more details can be found, e.g., in Frank et al. (2002). In the process of accretion, matter from the environment or a companion star falls onto the black hole and gains potential energy. For black holes in binary systems the mass originates usually from a companion star. Although most of the facts explained in the following are valid for accretion in binary systems in general, i.e., also for compact objects such as neutron stars or white dwarfs, we will focus on black holes systems, as this thesis focuses especially on the effects in these systems. The detailed behavior depends on the type of the system. In binary systems with a low mass star, the low mass X-ray binaries (LMXB), the mass usually just flows to the compact object via the Roche-Lobe overflow when the star’s radius gets large enough. For high mass X-ray binaries (HXMB), the companion star is more massive and can develop a strong stellar wind, which is then accreted by the compact object.

²The effects of the spin of a black hole will be treated in detail in Sec. 1.3.

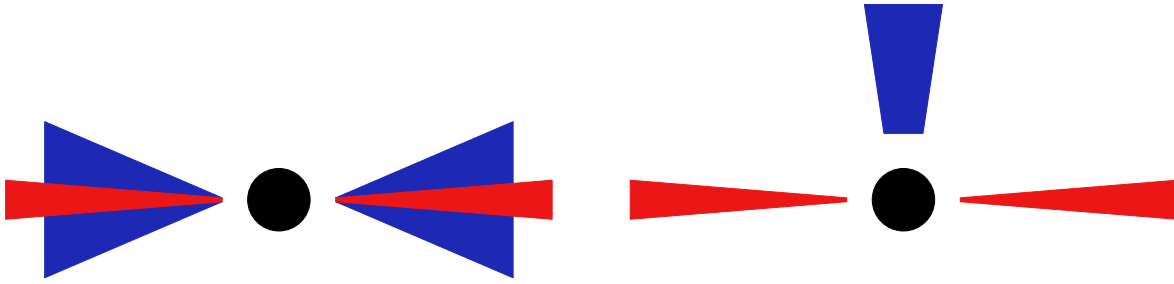


Fig. 1.2: *Different geometries for the source of hard X-rays: A corona of hot electrons around the inner parts of the disk (left panel) or the base of a relativistic jet (right panel). The hard X-ray source is drawn in blue and the accretion disk in red.*

As the gravitational potential is very deep, the amount of energy released can be up to 30% of the rest mass of the particle (Thorne, 1974). Additionally the matter usually has angular momentum and therefore cannot fall directly onto the black hole, but forms a so called “accretion disk” around it. In fact, if the matter would be cold and at initially at rest, it would fall directly into the black hole without any energy release, making it impossible to observe such a system (Zeldovich & Novikov, 1971). In order to be accreted, the angular momentum has to be transported outwards. Magneto-Hydrodynamic simulations show that shear forces due to small magnetic fields and turbulences in the disk might be able to create an effective viscosity (see, e.g., Krolik, 1999). Due to this viscous interaction in the disk, the matter is able to spiral inwards slowly. This can heat up the disk to million degrees of Kelvin, which means most of its energy is radiated in X-rays.

From the viscous heating of the accretion disk due to the inspiraling matter, a stretched black body spectrum would be expected, as the temperature for an optically thick disk decreases with $r^{-3/4}$ (Shakura & Sunyaev, 1973). Observations show that a component in the hard X-rays usually dominates the spectrum. The shape resembles a power law $E^{-\Gamma}$ with the photon index Γ and an exponential cutoff at high energies. Such a contribution could be created by up-scattering of the soft thermal photons by inverse Comptonization in a corona of hot electrons (Sunyaev & Trümper, 1979). The corona is assumed to be enclosing the inner regions of the accretion disk. The cutoff originates at the point where the photon energies are close to the temperature of the hot electrons, and hence cannot be supplied with more energy (Titarchuk & Hua, 1995). Alternative possibilities to explain the hard X-ray spectrum is that it originates from the base of a jet, the relativistic outflow seen in GBHs and AGN (Markoff & Nowak, 2004; Markoff et al., 2005). The different geometries of the system in the case of a hard X-ray source in form of a corona or a jet base are illustrated in Fig. 1.2. Chapter 5 discusses the model of the jet base in greater detail.

Some of these hard X-rays, either from the corona or a jet-base, can now irradiate the relatively cold accretion disk. Depending on the ionization of the disk, this leads to a spectrum of several emission lines. Figure 1.3 shows the result of a Monte Carlo simulation of a spectrum from a neutral disk which is irradiated by photons, distributed according to a power law. Higher ionized disks show less emission features and stronger absorption edges up to no signatures at all for fully ionized disks (Ross et al., 1999; Ross & Fabian, 2007). Due to the large abundance of Fe and its fluorescent yield, the Fe $K\alpha$ transition with an energy of 6.4 keV is usually the strongest (Reynolds & Nowak, 2003) and therefore often the only emission line detected in the X-ray spectrum.

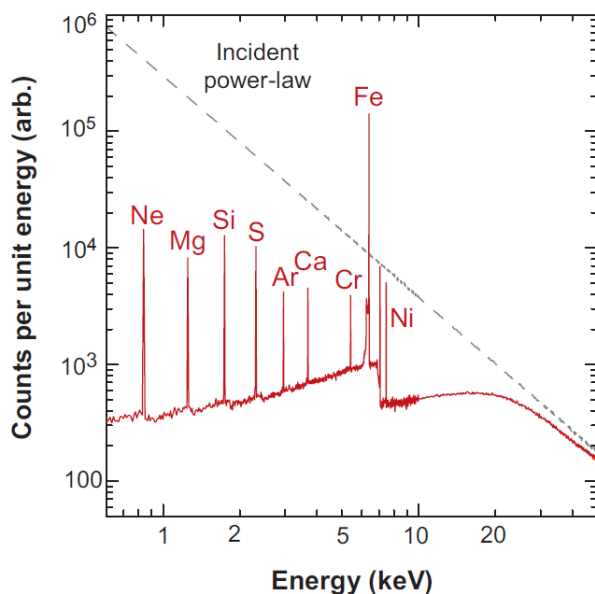


Fig. 1.3: A Monte Carlo simulation of a spectrum from a neutral disk which is irradiated by photons distributed according to a power law. The figure is taken from Miller (2007), who adapted it from Reynolds (1996).

1.3 THE SPIN OF A BLACK HOLE

The X-ray photons are emitted very close to the black hole, where the temperature is highest. Hence the special characteristic of spacetime is imprinted in the photon spectrum by curved trajectories and shifted energies. As General Relativity (GR) tells us how the spacetime should be curved, we are in principle able to look for deviations from its predictions and thus test the theory (Reynolds & Nowak, 2003). Up to now, GR is only tested for small curvature, i.e. only minor changes to flat spacetime (see proceedings of the 261th Symposium of the IAU³).

On the other hand, if we assume that General Relativity is also valid for strong curvature, we can learn more about the black hole itself by analyzing photons emitted close to the black hole. In the solution by Schwarzschild (1916), the mass is the only free parameter. Varying it does not alter the actual shape of spacetime, but can be interpreted as only changing the length scales. Hence we need to analyze a different parameter of the black hole, which actually deforms spacetime. It has already been stated that besides its mass, the second important parameter of an astrophysical black hole is its spin. Spinning black holes are described by the more complicated Kerr (1963) solution of General Relativity. A detailed description of the specialties of the metric, including equations for photon and particle orbits, is presented in Chap. 2. In order to quantify the value of the spin, the dimensionless spin parameter $a = J/M$ is commonly used, where J is the angular momentum of the black hole. In principle it can range from $a = -1$ (maximally negatively spinning) to $a = 1$ (maximal positive spin). Negatively spinning means that the accretion disk is counterrotating with respect to the black hole. Hence, such systems will often be called to have “negative spin” in the following. Section 1.3.3 deals with the question if such systems really exist and why their existence might be important.

Taking into account the black hole’s interaction with thermal photons from the accretion disc, its spin is restricted to $a \leq a_{\max} < 1$ as capturing photons with negative angular momentum (with respect to the movement of the disc) becomes more likely for increasing a and thus prevents a spin up to the extreme value of $a = 1$ (Thorne, 1974). Assuming that a negatively spinning system is created by flipping the spin of a system with $a > 0$ (see Sec. 1.3.3 for a

³<http://journals.cambridge.org/action/displayIssue?jid=IAU&volumeId=5&seriesId=0&issueId=S261>

motivation) sets the lower limit of the spin at $a \geq -a_{\max}$, as infalling matter from the counter-rotating disc decreases the absolute value of the spin with time. We choose $a_{\max} = 0.998$, which has been calculated by Thorne (1974) and is commonly used.

With increasing absolute value of the spin, spacetime is twisted and very close to the black hole even dragged with the rotation. The inner regions of the accretion disk and photons passing by close to the event horizon are affected by this deformation. Methods for measuring the spin are explained in the following.

1.3.1 MEASURING THE SPIN

In general, there are two methods to infer the spin of a black hole from spectroscopic analysis. One possibility is to analyze the thermal X-ray continuum. It makes use of the radial luminosity dependence $L(r)$ of the accretion disk. This function was analytically derived by Novikov & Thorne (1973) for a non-rotating black hole, and Riffert & Herold (1995) extended it to rotating black holes by introducing correction factors to the previous solution. Modeling the radial dependent effects of the Kerr metric allows to draw conclusions about the spin. For more details see (McClintock et al., 2006) and references therein.

The second approach for measuring the spin is using the relativistically broadened emission lines (such as the $K\alpha$ line), seen in many X-ray spectra (e.g. Fabian et al., 1989; Tanaka et al., 1995; Martocchia et al., 2002b; Miller et al., 2004). Although being a narrow line in the rest frame of the disk, the extremely fast rotation of the accretion disk and the effects of spacetime render the fluorescent emission line to be broad and asymmetric in the observer frame. Hence the spin of the black hole is encoded in the shape of this “broad emission line”. The value of the spin can then be estimated by comparing the observed line profile carefully with predictions of theoretical models. As the shape also depends on the emissivity, i.e., the radial and angular dependence of the emitted intensity $I_e(r_e, \theta_e)$, and the inclination of the surrounding accretion disk, broad emission lines have a very high diagnostic power. Figure 1.4 shows the best observed broad emission lines for a GBH and an AGN.

This thesis focuses on the method of broad emission lines for the spin measurement and its theoretical modeling. Therefore line profiles are calculated with great precision and compared to commonly used models for data analysis. As none of these models covers a retrograde rotation of the accretion disk with respect to the black hole, i.e., a black hole with negative spin, a new model code based on a Greens function approach is developed (Chap. 4).

1.3.2 CURRENT OBSERVATIONAL CONSTRAINTS

The skew-symmetric, broadened Fe $K\alpha$ emission lines have already been seen in many AGN such as the Seyfert galaxy MCG–6-30-15 (Tanaka et al., 1995; Wilms et al., 2001; Miniutti et al., 2007), 1H0707–495 (Fabian et al., 2009), and others (Nandra et al., 2007), galactic BHs such as GX 339-4 (Miller et al., 2004; Caballero-García et al., 2009), Cyg X-1 (Fabian et al., 1989; Miller et al., 2002), or GRS 1915+105 (Martocchia et al., 2002b; Blum et al., 2009), and neutron star systems (di Salvo et al., 2009; Cackett et al., 2008, 2009; Shaposhnikov et al., 2009).

Figure 1.5 shows a compilation of published spin measurements of black hole systems⁴, also including the method by fitting the thermal continuum. If the measurements are to be trusted, all values of the spin are possible and almost equally likely. In some cases there exist more than one spin measurement for one source, which even contradict each other. A special case is

⁴Neutron star systems are assumed to have spins close to zero, due to the magnetic coupling of neutron star and accretion disk.

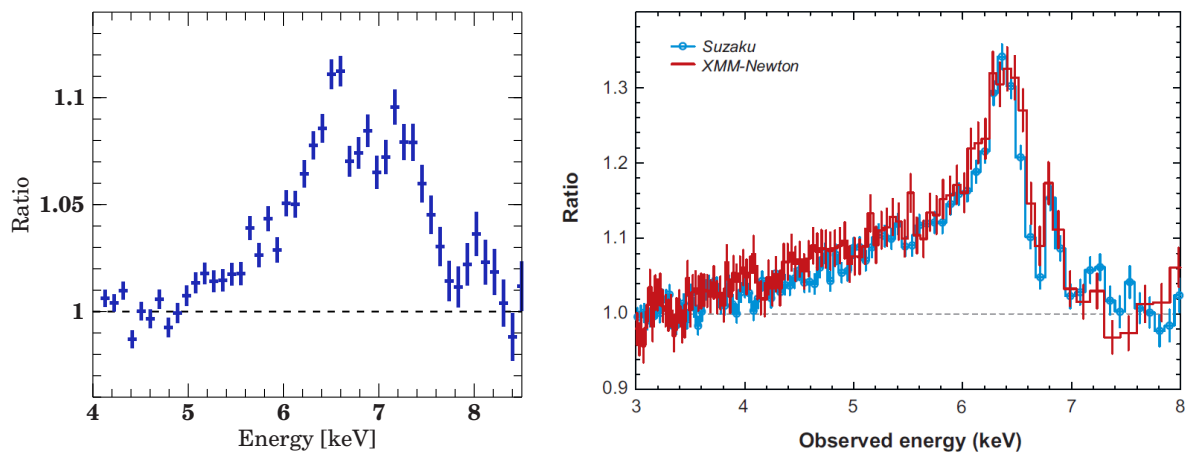


Fig. 1.4: The best signal to noise observations of a relativistic iron line in a X-ray binary (Cyg X-1, left) and an AGN (MCG-6-30-15, right). Cyg X-1 was observed for 17.4 ksec with XMM-Newton (Duro et al., in prep.) and the plot of MCG-6-30-15 shows a Suzaku and a XMM-Newton observation and was taken from Miller (2007), adapted from Miniutti et al. (2007) and Reeves et al. (2006). In order to emphasize the line profile, the spectrum was fitted by excluding the iron line region in both plots.

GRS 1915+105: Three different measurements of the spin, which range from $0 < a < 1$, exist in literature, although recent developments (McClintock et al., 2010) seem to favor a rapidly spinning black hole. This and other examples in the table shed some doubt on the exactness of the spin measurements. At least the formally small uncertainties point at the presence of systematic effects in the line measurements due to the high count rate of Galactic sources (Yamada et al., 2009; Done & Diaz Trigo, 2010) and due to the uncertainty of the parameters of the underlying continuum (e.g., Ross & Fabian, 2007; Reynolds & Fabian, 2008). On the other hand there are examples like MCG-6-30-15, where the spin measurement is more robust. By using a sophisticated analysis of the underlying continuum and assuming no emission between the inner radius of the accretion disk and the event horizon, Brenneman & Reynolds (2006) could show that MCG-6-30-15 harbors a fast spinning black hole and explicitly ruled out the case of a slowly or negatively rotating black hole.

Although the amount of measurements show that spin can be measured, the discrepancy between the results points towards the issue that different models might predict different shapes of the relativistic emission line. For example, many observations still use the laor model (Laor, 1991), which calculates the line profile by interpolating a sparsely sampled table for $a = 0.998$. Therefore Sec. 3.5 is dedicated to the comparison of currently used models for relativistic emission lines to new simulations of highly resolved line profiles.

1.3.3 NEGATIVE SPIN

Observations of AGN in the XMM-Newton and Chandra deep fields prove that broadened iron lines already occurred at high redshifts, z , (Comastri et al., 2004; Streblyanska et al., 2005, but see Corral et al. 2008). Although recent studies seem to exclude that these broad lines are a common feature (Longinotti et al., 2008), observations of such lines could therefore be used to study the expected evolution of black hole spin with z . For example, strong changes in amplitude and direction for the central black hole are predicted in stochastic evolution models

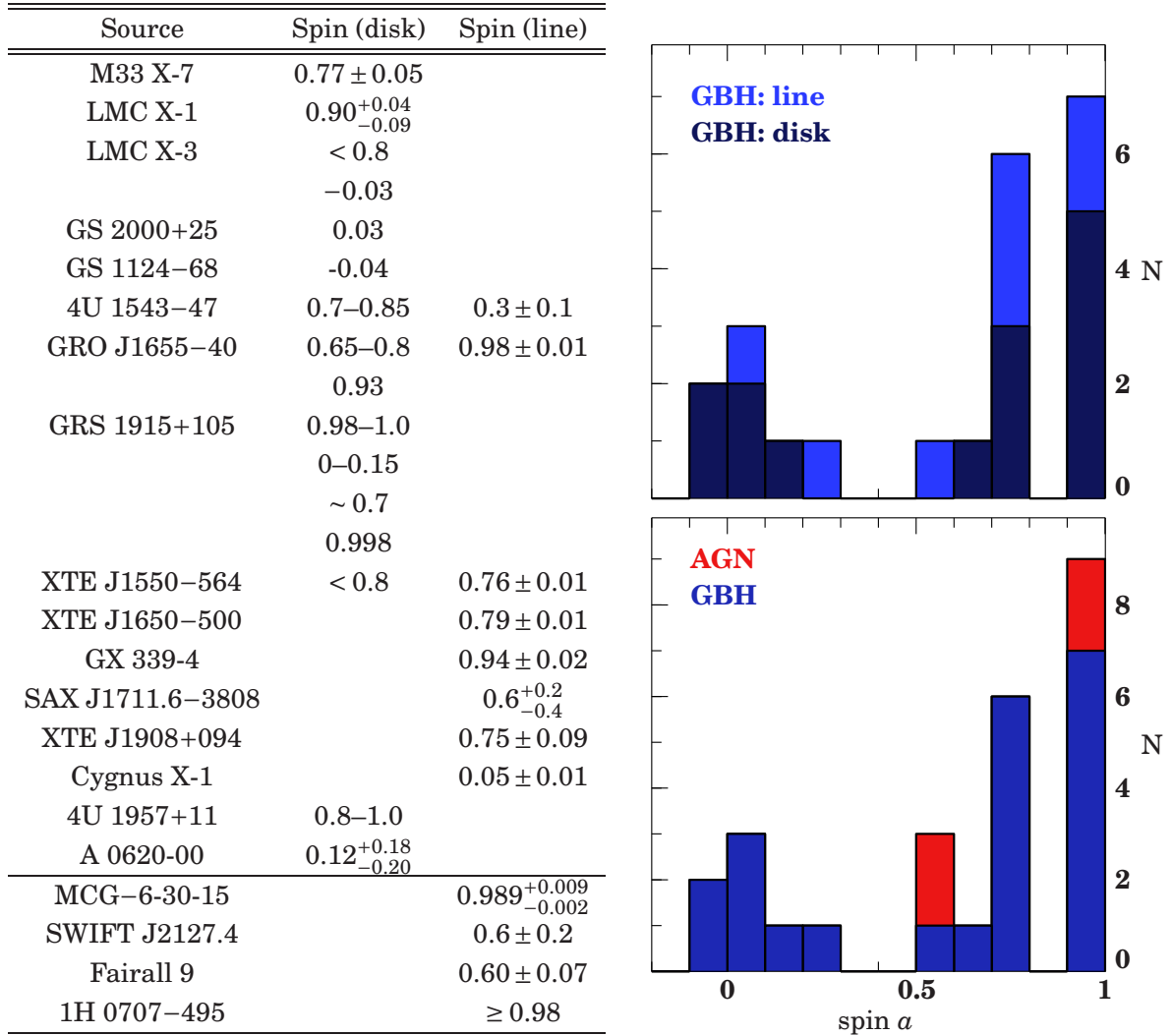


Fig. 1.5: Compilation of published spin measurements, distinguishing if the spin was determined by fitting the thermal continuum or the fluorescent emission line from the reflected spectrum. The table is taken from Fender et al. (2010), where also references for all single measurements can be found. All values (not upper limits) are plotted in the histograms in the right panel.

(King et al., 2008; Volonteri et al., 2005). Observations of cavities in nearby galaxy clusters are also evidence for spin evolution (Wise et al., 2007; Fabian et al., 2000). In galactic binary systems, the initial kick during the formation of a stellar-mass black hole in a supernova can lead to a strong misalignment between the disk and the black hole (Brandt & Podsiadlowski, 1995).

Depending on the mode of accretion, it is possible in all of these scenarios that the angular momenta of black hole and accretion disk become antiparallel, i.e., the black hole has “negative spin”. As shown by King et al. (2005), both parallel and antiparallel alignments of the disk and black hole angular momenta are stable configurations; misaligned disks will evolve to one of them. It is therefore not unlikely that a configuration with antiparallel spins exists in nature. In fact, accretion onto rapidly-spinning retrograde black holes may be of some importance for

understanding the properties of powerful radio-loud AGN. Employing the flux-trapping model of Reynolds et al. (2006), Garofalo (2009) argues that an accretion disk around a retrograde black hole is a particularly potent configuration for generating powerful jets. Moreover this interpretation might also explain why only 10% of the AGN are radio-loud (Garofalo et al., 2010). It is tantalizing that the broad iron line in the powerful radio-loud AGN 3C120 implies a truncation of the accretion disk at $r \sim 10GM/c^2$ (Kataoka et al., 2007), very close to the innermost stable circular orbit (ISCO) for a rapidly-rotating retrograde black hole.

1.4 THE AIM OF THIS WORK

This work aims at exploring the possibilities of broad emission lines for probing strong gravity and measuring the spin of black holes. Therefore it is necessary to understand the implications of General Relativity for the environment around a rotating black hole. Chapter 2 presents all basic and relevant equations to describe the necessary photon and particle trajectories around rotating black holes. Using the model of a thin accretion disk, which is made out of many particles orbiting the black hole in circles, Chap. 3 presents the necessary formalism and numerical techniques to describe photon trajectories emitted from a thin disk to the observer. Images of the accretion disk for important parameters like the energy shift and the emission angle of the photon are simulated in Sec. 3.2 in order to get a better understanding of the relativistic effects close to the black hole. Integrating over the disk assuming mono-energetic emission leads to broad emission lines. Sec. 3.3 explains the origin of the shape of these emission lines and explores the influence of parameters like the spin on the line profile. As the implications of a counterrotating accretion disk on the line profile were never treated in detail before, Sec. 3.4 explicitly shows and explains the differences one would expect in this case. Finally, I compare popular line models used in data analysis in Sec. 3.5. As none of the currently available models allow to analyze systems with negative spin, a new model was developed providing this possibility. The numerical details and usage of the model is presented in Chap. 4. Having treated the emission from the accretion disk in detail, Chap. 5 analyzes the irradiation of the disk for the case of the jet-base geometry, as current correlations between the radio and X-ray flares (Markoff et al., 2005; Wilms et al., 2007) make it a very favorable model. Chapter 6 presents the conclusions and an outlook of future work.

CHAPTER 2

BASIC THEORY ON SPINNING BLACK HOLES

In this chapter the fundamental equations for spinning black holes are motivated and partly derived. This is necessary to be able to describe photon and particle trajectories close to the black hole. Coming from the point that the observed broad emission lines are somehow due to the strong gravity in the vicinity of the black hole, these equations establish the connection between the observed broad emission features and the spin we want to measure. In the following all formula are given in units such that the gravitational constant and the velocity of light are equal to one ($G \equiv c \equiv 1$).

2.1 SPACETIME AROUND ROTATING BLACK HOLES

2.1.1 THE KERR METRIC

In General Relativity (GR), a spinning black hole can be described by the Kerr metric (Kerr, 1963), which is a solution of the Einstein equation for a spinning, spherical mass. It is fully determined by the mass M and the angular momentum J , which will be parametrized by the dimensionless parameter $a = J/M$. To prevent an unphysical naked singularity, its value is restricted to $|a| \leq 1$. The line element reads

$$ds^2 = -\left(1 - \frac{2Mr}{\Sigma}\right) dt^2 - \frac{4aMr \sin^2 \theta}{\Sigma} dt d\varphi + \frac{\Sigma}{\Delta} dr^2 + \Sigma d\theta^2 + \left(r^2 + a^2 \frac{2a^2 Mr \sin^2 \theta}{\Sigma}\right) \sin^2 \theta d\varphi^2, \quad (2.1)$$

where $\Delta = r^2 - 2Mr + a^2$ and $\Sigma = r^2 + a^2 \cos^2 \theta$. It is given in the Boyer-Lindquist coordinate system (Boyer & Lindquist, 1967), where the angle φ is measured in the plane of the disk, and the black hole's angular momentum points towards $\theta = 0$. This coordinate system can be related to Cartesian coordinates (see, e.g., Carroll, 2004) by

$$\begin{aligned} x &= \sqrt{r^2 + a^2} \sin \theta \cos \varphi \\ y &= \sqrt{r^2 + a^2} \sin \theta \sin \varphi \\ z &= r \cos \theta \end{aligned} \quad (2.2)$$

See Fig. 2.1 for a plot in Cartesian coordinates, where surfaces of constant r and θ illustrate the relation to Boyer-Lindquist coordinates.

In the case of a non-rotating black hole, this solution can easily be reduced to the Schwarzschild metric (1916) by setting $a = 0$:

$$ds^2 = -\left(1 - \frac{2Mr}{\Sigma}\right) dt^2 + \left(1 - \frac{2Mr}{\Sigma}\right)^{-1} dr^2 + r^2 d\theta^2 + r^2 \sin^2 \theta d\varphi^2 \quad (2.3)$$

As the Kerr metric is axis-symmetric and stationary, there exist two Killing vectors which characterize the conserved quantities (Carroll, 2004). As expected from classical mechanics, where the conserved energy originates from invariance under time translation, the time-like Killing vector $K^\mu = (\partial_t)^\mu$ in GR can be used to define the total energy of stationary system E_R (the Komar energy). It is straightforward to show (Carroll, 2004) that the Komar energy is equal to the mass $E_R = M$ given in Eq. 2.1. In analogy, the conserved angular momentum J_R can be defined using the rotational Killing vector $R^\mu = (\partial_\varphi)^\mu$ due to the axis-symmetry. This leads to $J_R = aM = J$ and confirms the above interpretation of J as angular momentum.

2.1.2 GENERAL PROPERTIES

A stationary observer sitting at a point (r, θ) should not feel any changes of the metric by definition. For our choice of coordinates this definition implies that (s)he has to rotate with angular velocity

$$\Omega = \frac{d\varphi}{dt} = \frac{u^\varphi}{u^t} \quad (2.4)$$

with respect to an observer who rests at infinity. Here the definition of the four-velocity is $u^\mu = dx^\mu/d\tau$, where τ is the proper time of a co-moving observer. The total four velocity of this observers then becomes

$$\vec{u} = u^t \partial_t + u^\varphi \partial_\varphi = u^t (\partial_t + \Omega \partial_\varphi) \quad (2.5)$$

Since $\vec{u}^2 = -1$ leads to

$$\begin{aligned} -1 &\stackrel{!}{=} u^\mu u_\mu \\ &= (u^t)^2 [(\partial_t)^\mu (\partial_t)_\mu + 2(\partial_\varphi)^\mu (\partial_t)_\mu + (\partial_\varphi)^\mu (\partial_\varphi)_\mu] \\ &= (u^t)^2 (g_{tt} + 2\Omega g_{t\varphi} + g_{\varphi\varphi}) \quad , \end{aligned} \quad (2.6)$$

the velocity in t -direction must be

$$u^t = \frac{1}{\sqrt{-g_{tt} - 2\Omega g_{t\varphi} - g_{\varphi\varphi}}} \quad (2.7)$$

This equation shows nicely that $u^t > 0$, which means that \vec{u} lies in the future light cone. Moreover, the expression under the root has to be positive. This sets an additional constraint on the angular velocity:

$$\Omega_{\min} = \frac{1}{g_{\varphi\varphi}} [-g_{t\varphi} - \sqrt{g_{t\varphi}^2 - g_{tt}g_{\varphi\varphi}}] < \Omega < \frac{1}{g_{\varphi\varphi}} [-g_{t\varphi} + \sqrt{g_{t\varphi}^2 - g_{tt}g_{\varphi\varphi}}] = \Omega_{\max} \quad (2.8)$$

For a non spinning black hole, this inequality restricts particles to move slower than c . Taking a closer look at Ω_{\min} reveals that it becomes zero at a radius

$$r_0 = \left(1 + \sqrt{1 - a^2 \cos^2 \theta}\right) r_g \quad , \quad (2.9)$$

called the “static limit”. This means that static observers ($\Omega = 0$), which are closer than this radius to the black hole, are forbidden. Here and throughout the work we use the “gravitational radius” $r_g = GM/c^2$ to quantify length scales.

Moving closer to the black hole, the event horizon is finally reached where there is only one possible value, with $\Omega_{\min} = \Omega_{\max}$. Following Carroll (2004), the event horizon at a radius r_H is uniquely characterized by the condition $g^{rr}(r_H) = 0$. In the case of the Kerr metric this means $\Delta \stackrel{!}{=} 0$, which results in a radius of

$$r_{\pm} = \left(1 \pm \sqrt{1 - a^2}\right) r_g \quad . \quad (2.10)$$

Another specialty of the Kerr spacetime is that unlike in the Schwarzschild metric the curvature singularity does not occur at $r = 0$, but rather at $\Sigma = 0$ (Carroll, 2004). As $\Sigma = r^2 + a^2 \cos^2 \theta$, this is only fulfilled for

$$r = 0 \quad \text{and} \quad \theta = \frac{\pi}{2} \quad . \quad (2.11)$$

Remembering that $r = 0$ is not a point in space but rather a disk (see Eq. 2.2), the above equation specifies the ring at the edge of this disk. Careful analytic calculations (Carroll, 2004) show that inside this ring another asymptotically flat spacetime exists, similar to the spacetime outside the ring, which can be connected by using $r < 0$.

Figure 2.1 shows the Kerr geometry projected onto the x - z plane for $a = 0.99$. The ring singularity (Eq. 2.11), which lies in the x - y -plane, is illustrated by the red points. Additionally the surfaces for $\theta = \text{const.}$ are drawn (gray dashed lines), in order to emphasize the point that the Cartesian coordinates are related to the Boyer-Lindquist coordinates (where r and θ are defined) via an elliptical transformation. Note that the horizons r_{\pm} , which are surfaces with $r = \text{const.}$, do have the shape of an ellipse. The region between the event horizon r_+ and the static limit r_0 is called the “ergosphere”. As explained above, an observer in this region has no choice but to rotate in the direction of the black hole. This phenomena is called “dragging of inertial frames” and leads to strange consequences such that it is indeed possible to dive into this zone and extract energy from the black hole. For further details on that see Carroll (2004).

2.2 GENERAL EQUATIONS OF MOTION

Determining the motion of particles and photons means calculating the evolution of $x^\mu(\lambda)$, described by the Geodesic Equation (see, e.g., Krolik, 1999):

$$\frac{d^2 x^\mu}{d\lambda^2} + \Lambda_{\rho\sigma}^\mu \frac{dx^\rho}{d\lambda} \frac{dx^\sigma}{d\lambda} = 0 \quad (2.12)$$

Equivalent to classical mechanics, it is possible to achieve the same relations more elegantly by using the Lagrangian or Hamiltonian formalism. As Krolik (1999) shows, the relativistic generalization can be done by redefining the action

$$S = \int_{A^\mu}^{B^\mu} \mathcal{L} d\lambda = \int_{A^\mu}^{B^\mu} d\lambda \left[g_{\mu\nu} \frac{dx^\mu}{d\lambda} \frac{dx^\nu}{d\lambda} \right]^{-\frac{1}{2}} \quad . \quad (2.13)$$

Minimizing it along the path by means of variation leads to the geodesic equation, which confirms that the Lagrangian describes the same movement. For massive particles one can set

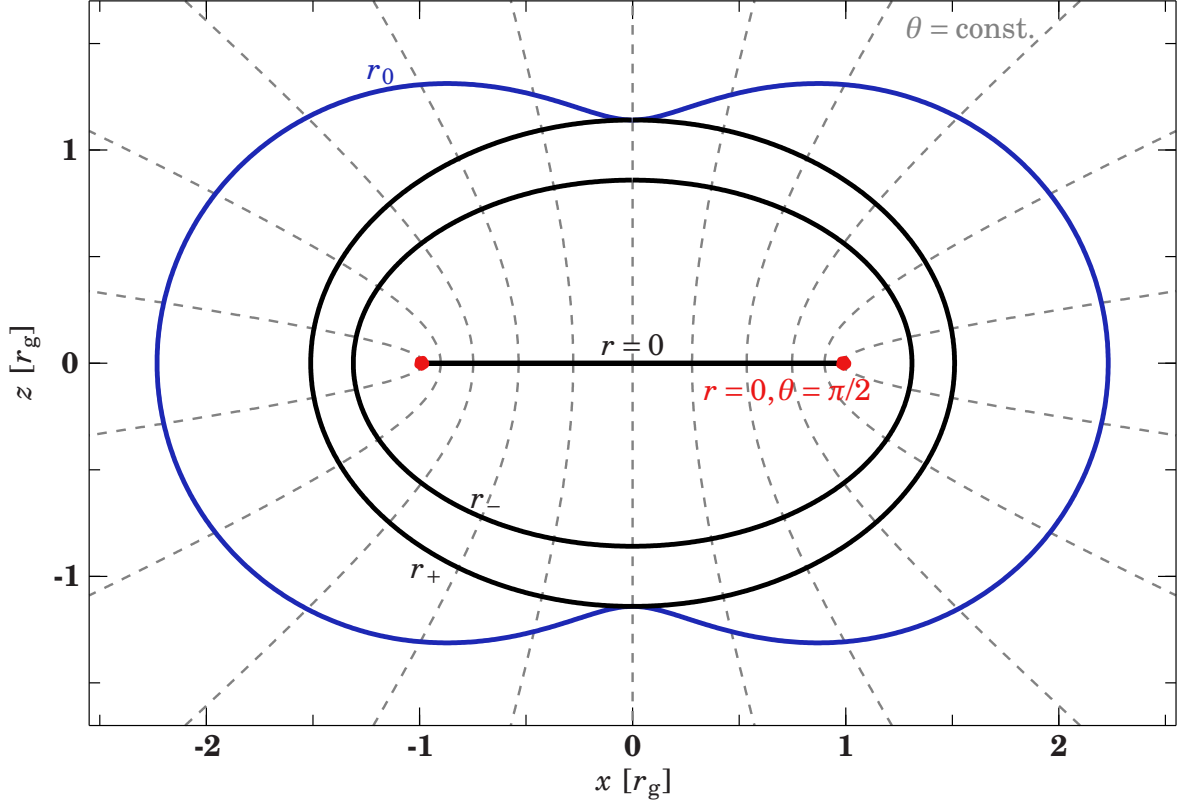


Fig. 2.1: The Kerr metric projected onto the x - z plane for a spin $a = 0.99$ in Cartesian coordinates. The area between the outer event horizon r_+ and the static limit r_0 is called ergosphere. The red dots for $r = 0$ and $\theta = \pi/2$ are part of the ring-like singularity in the x - y -plane. Additionally surfaces of constant θ are indicated by dashed gray lines.

$\lambda = \tau$ and easily see that the Lagrangian is constant along the path, which is a crucial requirement. This cannot be done for a photon, as its proper time is zero. Following Krolik (1999), choosing $\tau = \lambda\mu$ and an effective Lagrangian

$$\mathcal{L}_{\text{eff}} = \frac{1}{2} g_{\mu\nu} \dot{x}^\mu \dot{x}^\nu \quad , \quad (2.14)$$

solves this problem and leads to the same dynamical equations. As λ is an arbitrary parameter, we now can describe photons by $\mu = 0$ and massive particles by $\mu = 1$.

As we reduced our problem to a known formalism, calculating the Hamiltonian $H = p_\mu \dot{x}^\mu - \mathcal{L}_{\text{eff}}$ and the momentum $p_\mu = \frac{\partial \mathcal{L}}{\partial \dot{x}^\mu} = g_{\mu\nu} \dot{x}^\nu$ is now straightforward:

$$H = \frac{1}{2\Sigma} \left(\Delta p_r^2 + p_\theta^2 - \frac{(r^2 + a^2)^2 - a^2 \Delta \sin^2 \theta}{\Delta} p_t^2 + \frac{\Delta - a^2 \sin^2 \theta}{\Delta \sin^2 \theta} p_\varphi^2 - \frac{4Mar}{\Delta} p_t p_\varphi \right) \quad (2.15)$$

where

$$\begin{aligned}
 p_t &= -\left(1 - \frac{2Mr}{\Sigma}\right)\dot{t} - 2Mar\frac{\sin^2\theta}{\Sigma}\dot{\varphi} \\
 p_r &= \frac{\Sigma}{\Delta}\dot{r} \\
 p_\theta &= \Sigma\dot{\theta} \\
 p_\varphi &= \left(r^2 + a^2 + 2Ma^2r\frac{\sin^2\theta}{\Sigma}\right)\sin^2\theta\dot{\varphi} - 2Mar\frac{\sin^2\theta}{\Sigma}\dot{t}
 \end{aligned} \tag{2.16}$$

The derivations of the Hamiltonian $\partial_\mu H = -\dot{p}_\mu$ with respect to t and φ are zero, which immediately lead to the conserved energy $p_t = -E$ and angular momentum $p_\varphi = L$. Additionally the constancy of the Hamiltonian describes the conservation of the test particles rest mass

$$H = -1/2\mu^2 \quad . \tag{2.17}$$

A last conserved quantity

$$\mathcal{Q} = p_\theta^2 + \cos^2\theta \left[a^2(\mu^2 - p_t^2) + p_\varphi^2/\sin^2\theta \right] \tag{2.18}$$

was found by Carter (1968), which can be derived by making a separation ansatz in the Hamilton-Jacobi formalism with respect to θ and r . Now the equations of motion are fully determined and lengthy algebraic calculations (see Bardeen et al., 1972) lead to

$$\begin{aligned}
 \Sigma\dot{t} &= -a(aE\sin^2\theta - L) + (r^2 + a^2)\frac{T}{\Delta} \\
 \Sigma\dot{r} &= \pm\sqrt{V_r} \\
 \Sigma\dot{\theta} &= \pm\sqrt{V_\theta} \\
 \Sigma\dot{\varphi} &= -\left(aE - \frac{L}{\sin^2\theta}\right) + a\frac{T}{\Delta} \quad ,
 \end{aligned} \tag{2.19}$$

for which we defined

$$\begin{aligned}
 T &= E(r^2 + a^2) - aL \\
 V_r &= T^2 - \Delta(\mu^2 + r^2 + (L - aE)^2 + \mathcal{Q}) \\
 V_\theta &= \mathcal{Q} - \cos^2\theta \left[\frac{L^2}{\sin^2\theta} + a^2(\mu^2 - E^2) \right] \quad .
 \end{aligned} \tag{2.20}$$

The signs in Eq. 2.19 can be chosen independently and account for the direction of the particle. The upper sign means a movement with increasing r , θ and the lower sign stands for the opposite behavior, respectively. Thus they can be chosen arbitrarily, but change, e.g., when a turning point occurs.

2.2.1 THE ACCRETION DISK

Having developed the general equations of motion in the Kerr metric, we now want to apply them to describe a thin accretion disk, which lies in the equatorial plane of the black hole. This implies that

$$\theta = \pi/2 \quad \text{and} \quad \dot{\theta} = 0 \quad , \tag{2.21}$$

and therefore $\mathcal{Q} = 0$. The accretion disk itself is most easily modeled by particles which move on infinitely many circular orbits of different radii. This means that the velocity and the acceleration in r -direction has to vanish:

$$\dot{r} = 0 \xrightarrow{\text{Eq. 2.19}} V_r(r) = 0 \quad \text{and} \quad \ddot{r} = 0 \xrightarrow{\text{Eq. 2.19}} \frac{dV_r(r)}{dr} = 0 \quad (2.22)$$

Additionally we want the accretion disk to be stationary, because the equations we calculated before are only valid in this case. These constraints are sufficient to fully determine the trajectories of the particles, which has been done in detail by Bardeen et al. (1972). The results will be motivated in the following.

Bardeen et al. (1972) first calculated the explicit expressions of E and L :

$$\frac{E}{\mu} = \frac{r\sqrt{r} - 2M\sqrt{r} + a\sqrt{M}}{r^{3/4}\sqrt{r\sqrt{r} - 3M\sqrt{r} + 2a\sqrt{M}}} \quad (2.23)$$

$$\frac{L}{\mu} = \frac{\sqrt{M}(r^2 - 2a\sqrt{M}\sqrt{r} + a^2)}{r^{3/4}\sqrt{r\sqrt{r} - 3M\sqrt{r} + 2a\sqrt{M}}} \quad (2.24)$$

Using these results, the angular velocity of the stationary accretion disk becomes

$$\Omega = \frac{d\varphi}{dt} = \frac{\sqrt{M}}{r\sqrt{r} + a\sqrt{M}} \quad , \quad (2.25)$$

Note that the fact that particles can be on pro- and retrograde orbits with respect to the spinning direction of the black hole is already correctly taking into account: In our interpretation the accretion disk always rotates in the same direction, but the black hole changes the direction ($a < 0$).

Assuming stable orbits of the particles in order to form an accretion disk additionally imposes that

$$\frac{d^2V_r(r)}{dr^2} \leq 0 \quad , \quad (2.26)$$

which is sufficient for stability as $V_r(r) \geq 0$. Solving this system of equations reveals that only radii $r \geq r_{\text{ms}}$ are stable, with

$$r_{\text{ms}}(a) = M \left(3 + Z_2 - \text{sgn}(a)\sqrt{(3 - Z_1)(3 + Z_1 + 2Z_2)} \right) \quad , \quad (2.27)$$

where

$$\begin{aligned} Z_1 &= 1 + (1 - a^2)^{1/3} \left[(1 + a)^{1/3} + (1 - a)^{1/3} \right] \\ Z_2 &= \sqrt{3a^2 + Z_1^2} \quad . \end{aligned} \quad (2.28)$$

This means that the accretion disk only extends down to a certain radius of ‘‘marginal stability’’, which, e.g., is given by

$$r_{\text{ms}} = \begin{cases} 1.24 r_g & \text{for } a = 0.998 \\ 6 r_g & \text{for } a = 0 \\ 8.994 r_g & \text{for } a = -0.998 \end{cases} \quad (2.29)$$

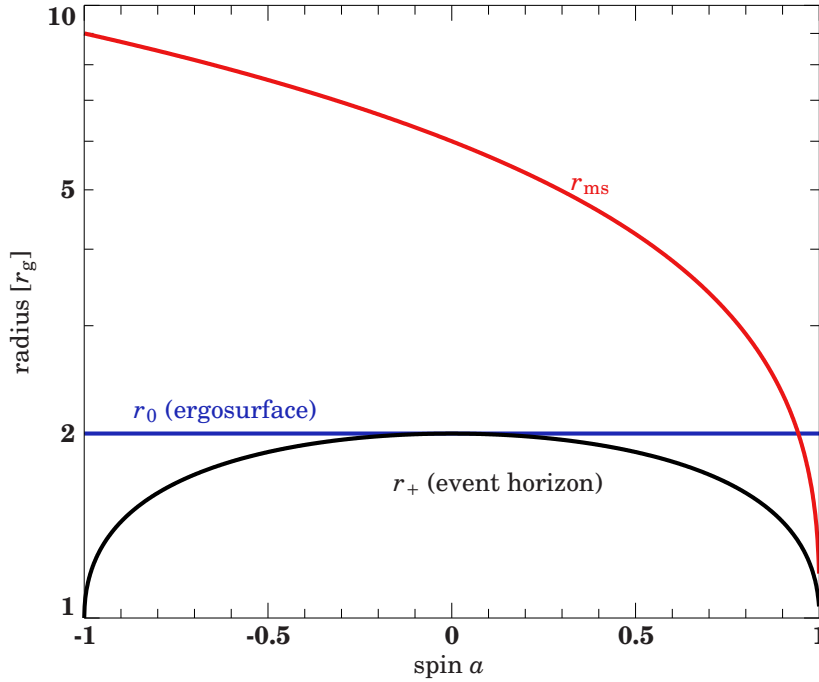


Fig. 2.2: This plot shows the evolution of all important surfaces around rotating black holes with respect to their angular momentum a . The ergosurface r_0 is plotted for $\theta = \pi/2$, as this is the plane of the accretion disk.

Often the radius of marginal stability is also called the radius of the “innermost stable circular orbit” (ISCO). Fig. 2.2 shows a summary of the evolution of all important radii mentioned above with respect to a .

Using Eq. 2.5, the four-velocity of the particles making up the accretion disk can be derived as

$$\vec{u}_d = u^t (\partial_t + \Omega \partial_\varphi), \quad \text{with } u^t = \frac{r\sqrt{r} + a\sqrt{M}}{\sqrt{r}\sqrt{r^2 - 3Mr + 2a\sqrt{M}\sqrt{r}}}. \quad (2.30)$$

Clearly it is also possible to extract the trajectories for $r \leq r_{\text{ms}}$ from the equations above. As the orbits are not stable, the particles fall towards the event horizon with the energy $E(r_{\text{ms}})$ and angular momentum $L(r_{\text{ms}})$ they have at the radius of marginal stability. This implies that the particles might have a non-zero velocity and acceleration in r -direction and therefore their total four-velocity is given by $\vec{u} = u^t \partial_t + u^r \partial_r + u^\varphi \partial_\varphi$. As we will not need these trajectories in the following and the equations are rather lengthy they are not written here. Interested readers can find them in Chandrasekhar (1983).

2.2.2 PHOTON TRAJECTORIES

Having described the location and frame where the photons are emitted, we now want to follow their way to the observer. Due to the large distance to the black hole system, we will only see photons which travel exactly in our direction. In other words, by looking at the system under different angles we will measure different photons and obtain different results for the line shape. Thus it is only important to consider photons which travel at infinity in the same direction. This section follows the detailed descriptions of Chandrasekhar (1983).

The photons originate from the stationary and axis-symmetric accretion disk, which implies that we only have to consider the (r, θ) -plane simply because of the symmetry. This leaves us with only two equations of motion from Eq. 2.19. Integrating over the path from the point of

emission at the accretion disk $(r_e, \pi/2)$ to the observer at infinity (∞, θ_o) leads to

$$\int_{r_e}^{\infty} \frac{dr}{\sqrt{V_r}} = \int_{\pi/2}^{\theta_o} \frac{d\theta}{\sqrt{V_\theta}} . \quad (2.31)$$

Additionally one has to take into account that the photons might have turning points in r and θ -direction. This means that the integration has to be split into several parts. The final solution will be a combination of these parts, which accounts for the different paths the photon can take to reach the distant observer.

Examining the possible parameter space of Eq. 2.31 quickly leads to the conclusion that the roots require

$$V_r(r) \geq 0 \quad \text{and} \quad V_\theta(\theta) \geq 0 \quad (2.32)$$

for a real solution. The limits determined by these conditions can be identified with the turning points r_t and η_t (see Chandrasekhar, 1983, for details). Moreover these conditions restrict $q^2 > 0$ for reasonable photon orbits, which can in principle reach the observer (Chandrasekhar, 1983). Taking into account that the sign changes at the turning point, the trajectories of the photons can be derived. Without any turning points the integration of Eq. 2.31 can now be performed

$$\int_{r_e}^{\infty} \frac{dr}{\sqrt{V_r}} = - \int_0^{\eta_o} \frac{d\eta}{\sqrt{V_\eta}} , \quad (2.33)$$

where we defined $V_\eta := \sin^2\theta V_\theta$ and substituted $\eta = \cos\theta$. Considering a turning point in θ -direction splits the integration over η in two parts:

$$\int_{r_e}^{\infty} \frac{dr}{\sqrt{V_r}} = - \int_0^{\sqrt{\eta_t^2}} \frac{d\eta}{\sqrt{V_\eta}} + \int_{\sqrt{\eta_t^2}}^{\eta_o} \frac{d\eta}{\sqrt{V_\eta}} . \quad (2.34)$$

Looking at the case of the r -integration in a rough geometrical picture reveals that the turning point can only occur if the black hole is between the point of emission and the observer. Otherwise the turning point of the photon would be closer to the black hole than the location where it was emitted, which can be considered as highly unlikely. Moreover a photon emitted behind the black hole requires in this picture a turning point in θ -direction in order to be seen by the observer. Thus we only need one last equation with a turning point for each direction:

$$- \int_{r_e}^{r_t} \frac{dr}{\sqrt{V_r}} + \int_{r_t}^{\infty} \frac{dr}{\sqrt{V_r}} = - \int_0^{\sqrt{\eta_t^2}} \frac{d\eta}{\sqrt{V_\eta}} + \int_{\sqrt{\eta_t^2}}^{\eta_o} \frac{d\eta}{\sqrt{V_\eta}} \quad (2.35)$$

Solving these equations for a specific E and L now fully determines the movement of the photon. For means of easier calculation it is convenient to choose new integrals of motion

$$\lambda = \frac{L}{E} \quad \text{and} \quad q^2 = \frac{\mathcal{Q}}{E^2} , \quad (2.36)$$

and multiply $V_{r,\eta}$ with E^{-2} . This leads to

$$V_r = r^4 + (a^2 - \lambda^2 - q^2)r^2 + 2M((a - \lambda)^2 + q^2)r - a^2q^2 \quad (2.37)$$

$$V_\eta = -a^2\eta^4 + (a^2 - \lambda^2 - q^2)\eta^2 + q^2 \quad . \quad (2.38)$$

The momentum of the photon expressed in the most convenient way then reads

$$\begin{aligned} p_t &= -E \\ p_r &= \pm \frac{E}{\Delta} \sqrt{V_r} \\ p_\theta &= \pm E \sqrt{V_\theta} \\ p_\varphi &= E\lambda \quad . \end{aligned} \quad (2.39)$$

CHAPTER 3

EMISSION FROM A THIN ACCRETION DISK

In the previous chapter we derived all important equations to be able to describe the particle orbits for a thin accretion disk in the equatorial plane and the relevant photon orbits around a rotating black hole. These results allow us finally to simulate the photon spectrum observed from mono-energetic emission from the accretion disk, which leads to the broad emission lines. This chapter captures all major effects that influence photons on the way to the observer. The numerical approach chosen in Sec. 3.1 allows us to calculate and analyze relativistically distorted images of the accretion disk in Sec. 3.2. Finally, line profiles and the influence of parameters like the spin or the viewing angle on their shape are examined in great detail (Sec. 3.3). Although every equation was calculated for a spin $-1 < a < 1$, Sec. 3.4 is dedicated to highlight the characteristics of broad lines for negatively spinning black holes. In addition, popular models describing these broad emission feature are compared in Sec. 3.5.

3.1 TRANSFER FUNCTION

By solving Eq. 2.31, we are able to describe single photons that are emitted at the disk and are detected under a view angle θ_o . Before getting to the numerical details of solving this equation, we will first try to describe the emission from the whole accretion disk, based on the model of a thin disk described in Sec. 2.2.1.

3.1.1 RADIATION TRANSPORT

For an observer far away from the system, the black hole is a point source. This means that (s)he can only see the whole disk at once and thus to calculate the observed intensity $I_E^{\text{obs}}(\theta_o)$, the locally emitted intensity $I_{E_e}(r_e, \theta_e)$ has to be integrated. The specific intensity I_{E_e} emitted at the disk at energy E_e depends only the radius r_e and the emission angle θ_e , due to the symmetry of the system. It is defined as intensity of photons with energies between E and $E + dE$ according to

$$I_E = \frac{E dN}{dA dE d\Omega dt} \quad , \quad (3.1)$$

where dN is the number of photons in the solid angle $d\Omega$ with energy, which flow through the area dA in the time dt . As these variables are clearly not Lorentz invariant, I_E is not a good quantity and will vary depending on the chosen frame of reference. We therefore need to find

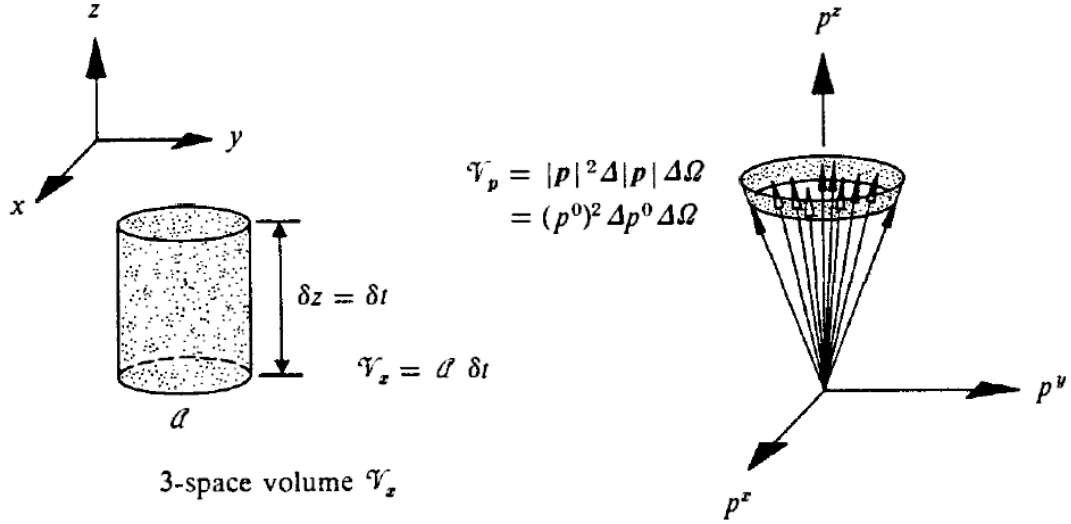


Fig. 3.1: A drawing of volumes of the phase space $V_x V_p$, for the momentum space V_p and the normal space V_x , necessary to calculate the number density of trajectories \mathcal{N} in curved space. (adapted from Misner et al., 1973)

a way to convert the emitted intensity I_{E_e} at the accretion disk to the measured intensity I_{E_o} . Following Misner et al. (1973), it can be shown that the number density, $\mathcal{N} = \delta N / (V_x V_p)$, of photons is an invariant, as

$$\frac{d\mathcal{N}}{d\lambda} = 0 \quad . \quad (3.2)$$

Here $V_x V_p$ is the phase space volume of N identical particles. Equation 3.2 is the collisionless Boltzmann equation in curved space, which can be easily derived from the general “Liouville theorem”. Explicit considerations (see Fig. 3.1) lead to $V_x = A dt$ and $V_p = d\Omega E^2 dE$. As we required all particles to be the same, the relation $\vec{p}^2 = m^2$ dictates the four-momenta to lie on a hyperboloid. Now we can identify the specific intensity with the conserved number density and we get

$$\frac{I_E}{E^3} = \mathcal{N} = \text{const.} \quad (3.3)$$

Now we finally obtained a connection between the observed and the locally emitted intensity. The integration over the whole accretion disk is easily performed, after the disk is projected onto a plane perpendicular to the line of sight, spanned by the impact parameters α and β (see Eq. 3.16), which are connected to the solid angle through (Cunningham & Bardeen, 1973)

$$d\alpha d\beta = d^2 d\Omega \quad , \quad (3.4)$$

where d is the distance to the system. Using this relation, the observed intensity becomes

$$I_E^{\text{obs}} = \int \left(\frac{E}{E_e} \right)^3 I_{E_e}(r_e, \theta_e) d\alpha d\beta \quad . \quad (3.5)$$

The ratio E/E_e between observed and emitted energy is exactly the energy shift g of the photon. For a non-rotating black hole, this energy shift can be easily calculated from the Schwarzschild

metric (see e.g. Carroll, 2004) to be

$$g(a=0) = \sqrt{1 - \frac{2M}{r_e}} . \quad (3.6)$$

Taking into account that the observer measures in a flat Minkowski space and using the expressions for the four-momentum of the photon in the Kerr metric, the expression of the general relativistic Doppler shift becomes

$$g = \frac{E}{E_e} = -\frac{E}{p_e^\mu u_\mu} = \frac{\sqrt{r_e} \sqrt{r_e^2 - 3Mr_e + 2a\sqrt{Mr_e}}}{r_e \sqrt{r_e + a\sqrt{M}} - \beta(\alpha)\sqrt{M}\lambda} . \quad (3.7)$$

Note that λ depends on the direction of the black hole's rotation, i.e., that the sign changes in the case of negative spin, as the photon does not change its direction. This is taken into account by the function

$$\beta(\alpha) = \begin{cases} +1 & \text{for } \alpha \geq 0 \\ -1 & \text{for } \alpha < 0 \end{cases} . \quad (3.8)$$

The introduction of $\beta(\alpha)$ is required, as a change in the direction of the rotation implicitly requires a flip of the coordinate system, but we do not want the photon to change direction. In principle this would be taken into account correctly by the sign of the spin, but in the case of $\alpha = 0$ one coordinate system has to be chosen. Figure 3.2 shows the energy shift of a complete accretion disk as seen by a distant observer, illustrating the effects of gravitational redshifting, Doppler boosting, and light bending. Note that for the special case of viewing the accretion disc from top ($\theta_0 = 0$, leading to $\lambda = 0$), the purely gravitational redshift for a negative spin is slightly higher than for positive a.

Moreover Eq. 3.7 implies that if we know at which energy the photon is emitted from the disk and how its energy is shifted, we can calculate the energy at which it should be observed. For simplification of the calculation, we create a homogeneous parameter space by redefining g . Using the maximal and minimal value of g , we define for each gas ring and inclination angle the parameter

$$g^* := \frac{g - g_{\min}}{g_{\max} - g_{\min}} , \quad 0 \leq g^* \leq 1 . \quad (3.9)$$

Due to symmetry, there can be up to two solutions for a specific g^* and a certain radius. The reason for the existence of these two solutions can be easily visualized, as one obviously has two possibilities on a circle to get from the minimum to the maximum value of the energy shift. As g is a steady function, each value in between the extreme values appears twice.

The only unknown quantity left is the emission angle θ_e . Due to the effects of strong gravity in the vicinity of the black hole, the photons do not travel on a straight path and will in general be observed under an angle different from the one under which they are emitted. Nevertheless, the emission angle is already totally defined by the four-momentum of the emitted photon. With the normal vector to the disk \vec{n} and the energy of the photon $-p_e^\mu u_\mu$, these quantities are related by

$$\cos(\theta_e) = \frac{\vec{p}_{e\perp}}{|\vec{p}_e|} = -\frac{p_e^\mu n_\mu}{p_e^\mu u_\mu} = -\frac{p_e^\mu n_\mu}{E} g , \quad (3.10)$$

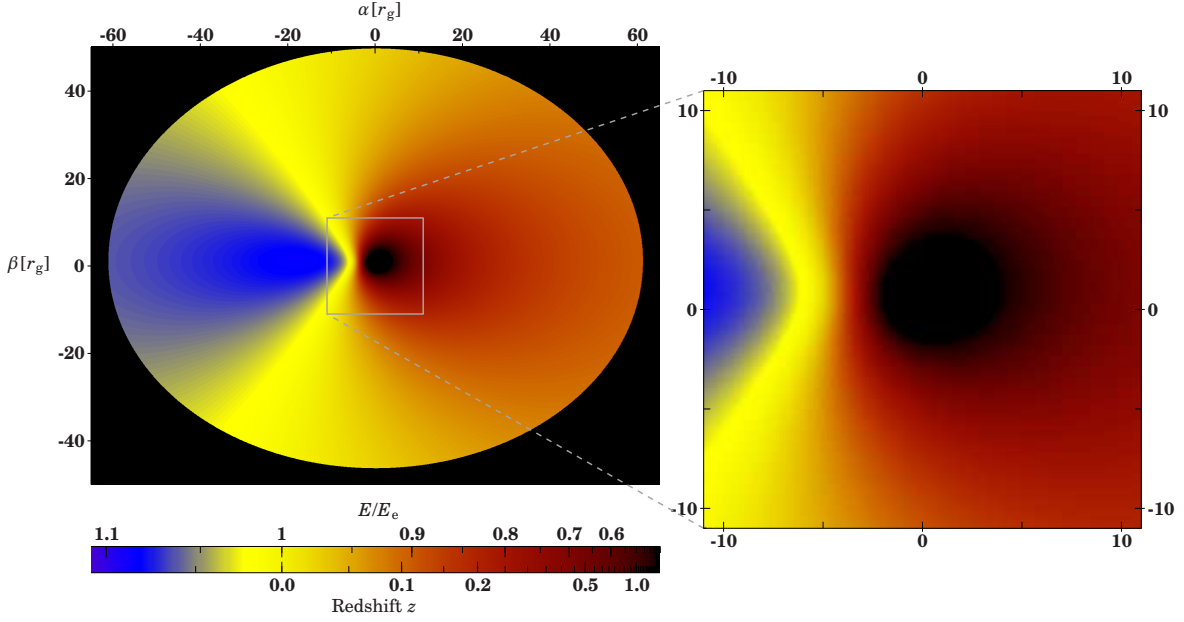


Fig. 3.2: Map of an accretion disk around a maximally spinning black hole ($a = 0.998$) as seen from a distant observer at an inclination angle of $\theta_o = 40^\circ$. The disk ranges from the marginally stable radius ($r_{\text{in}} = 1.24 r_g$) to $r_{\text{out}} = 60 r_g$. α and β are the coordinates defined on the plane of the sky (i.e., perpendicular to the line of sight; see Eq. 3.16). The color code shows the energy shift of the photons, asymmetries are due to relativistic light bending. The blue-shifted left part of the disk moves towards the observer, whereas the right part recedes from the observer.

where we used Eq. 3.7 for the last equality. Furthermore the normal vector can be expressed by

$$\vec{n} = \frac{1}{\Sigma} \partial_\theta \Big|_{\theta=\pi/2}, \quad (3.11)$$

as it is defined as a spatial vector perpendicular to the accretion disk. Using the four-momentum of the photon from Eq. 2.39, the fact that $\eta^2|_{\pi/2} = 0$, and the expression for V_η (Eq. 2.37), the angle becomes

$$\cos(\theta_e) = \frac{qg}{r_e}. \quad (3.12)$$

3.1.2 TRANSFER FUNCTION OF CUNNINGHAM

For means of calculation, Cunningham (1975) defined the *Transfer Function* f

$$f(g^*, r_e, \theta_0) = \frac{1}{\pi r_e} g \sqrt{g^*(1-g)} \left| \frac{\partial(\alpha, \beta)}{\partial(g^*, r_e)} \right|. \quad (3.13)$$

Using the relations derived above, the total observed intensity then reads

$$I_E^{\text{obs}} = \int_{r_{\text{ms}}}^{\infty} \int_0^1 4\pi^2 r_e \frac{g^2}{g^*(1-g^*)} f(g^*, r_e, \theta_0) I_{E_e}(r_e, \theta_e) dr_e dg^* \quad (3.14)$$

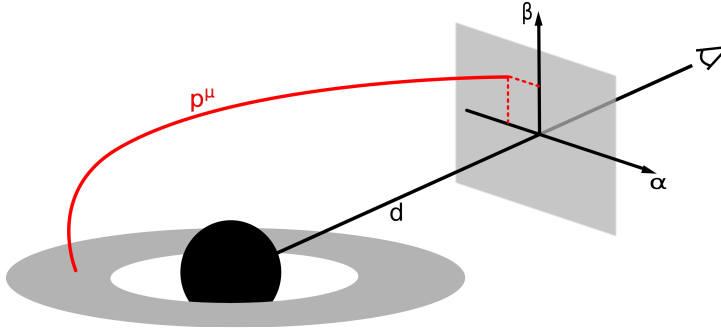


Fig. 3.3: The impact parameters α and β for a photon with momentum p^μ . They describe how a distant observer would see photons emitted around the black hole, which are projected perpendicular to his line of sight.

Here we parametrized the accretion disk in (r_e, g^*) space. Because this parametrization leads to the conserved quantities λ and q , the motion is still defined properly.

In models for describing broad emission lines, the specific intensity I_{E_e} is commonly parametrized by

$$I_{E_e} \propto r_e^{-\alpha} \cdot \epsilon(\theta_e) \quad . \quad (3.15)$$

Thus the radial dependence is described by a power law characterized by the emissivity index α . Usually values of $\alpha = 2-3.5$ are observed. Furthermore the intensity might depend on the emission angle. The angular dependency is described by $\epsilon(\theta_e)$.

3.1.3 NUMERICAL CALCULATION

For the numerical evaluation of the transfer function we use a Fortran 77 code developed by Speith et al. (1995). Therein the emission from the accretion disk is modeled by a grid in the (r_e, g^*) -space. As explained above, this approach is sufficient to describe the motion of the photons.

In order to evaluate the derivation of the impact parameters α and β (Eq. 3.4) in the transfer function (Eq. 3.13), we need to express them in terms of the photon momentum. Fig. 3.3 illustrates the definition of the impact parameters.

Now we express the impact parameters by the four momentum using simple geometric considerations as

$$\alpha = -d \frac{p^{(\varphi)}}{|p^{(\mu)}|} = -d \frac{p_\mu [e^{(\varphi)}]^\mu}{p_\mu [e^{(t)}]^\mu} \quad \text{and} \quad \beta = d \frac{p^{(\theta)}}{|p^{(\mu)}|} = d \frac{p_\mu [e^{(\theta)}]^\mu}{p_\mu [e^{(t)}]^\mu} \quad . \quad (3.16)$$

The coordinates of the momentum in the equation above are written in brackets in order to show that they are the coordinates of the observer in a flat Minkowski space. Following Misner et al. (1973), (s)he aligns his/her tetrads¹

$$\vec{e}_{(t)} = \vec{u} \quad , \quad \vec{e}_{(i)} = \vec{e}_{(i)}^\mu \partial_\mu \quad \text{and} \quad \vec{e}_{(i)}^\mu \vec{e}_{(i)}^\nu g_{\mu\nu} = \eta_{(i)(j)} \quad , \quad (3.17)$$

where $\eta_{\mu\nu}$ is the Minkowski metric. Applying these conditions, the tetrads of an observer at

¹In GR the tetrads are an orthonormal set of four vector fields. For more information see, e.g., Misner et al. (1973)

rest can be constructed. In spherical coordinates they read:

$$\begin{aligned}
\vec{e}_{(t)} &= \sqrt{\frac{\Sigma}{\Sigma - 2Mr}} \partial_t \\
\vec{e}_{(r)} &= \sqrt{\frac{\Delta}{\Sigma}} \partial_r \\
\vec{e}_{(\theta)} &= \frac{1}{\sqrt{\Sigma}} \partial_\theta \\
\vec{e}_{(\varphi)} &= -\frac{2Mra}{\sqrt{\Sigma\Delta}} \sqrt{\frac{\sin^2 \theta}{\Sigma - 2Mr}} \partial_r + \sqrt{\frac{\Sigma - 2Mr}{\Sigma\Delta \sin^2 \theta}} \partial_\varphi
\end{aligned} \tag{3.18}$$

Combining the coordinate system of the observer with the four momentum of the emitted photon (Eq. 2.39), we can now derive the impact parameters with Eq. 3.16. As the observer is far away, we take the limit $d \rightarrow \infty$ and obtain

$$\alpha = -\frac{\lambda}{\sin \theta_0} \quad \text{and} \quad \beta = \pm \sqrt{V_\theta} \quad . \tag{3.19}$$

Furthermore the impact parameters are defined such that

$$d\alpha d\beta = \left| \frac{\partial(\alpha, \beta)}{\partial(\lambda, q)} \right| d\lambda dq = \frac{q}{\sin \theta_0 \beta} d\lambda dq \quad . \tag{3.20}$$

In this way we are able to calculate the partial derivative of the solid angle, which appears in the transfer function f (Eq. 3.13), leading to

$$\left| \frac{\partial(\alpha, \beta)}{\partial(g^*, r_e)} \right| = \frac{q(g_{\max} - g_{\min})}{\sin \theta_0 \beta \left| \frac{\partial(g^*, r_e)}{\partial(\lambda, q)} \right|} \quad . \tag{3.21}$$

The exact description of the numerical details are given by Speith et al. (1995). A short summary will be given in the following, focusing on the parts that were changed in order to allow also for negative spin.

At the beginning a certain gas ring with radius r_e is chosen and its minimal and maximal energy shift is calculated. Using Eq. 3.9, the ring is split into parts of different energy shift g^* . For each single value of g^* , λ can be calculated by transforming Eq. 3.7. This is inserted in the integral equations (Eqs. 2.33–2.35), where the only unknown quantity is q . Solving these equations numerically for q in each case, we filter the photons with a certain (g^*, r_e) that actually hit the observer. Now the motions are fully determined and we can calculate the derivative of Eq. 3.21 numerically in order to derive the transfer function. As we build the accretion disk out of many gas rings, we have to repeat this procedure for their different r_e .

All the above steps are calculated using the algorithm provided by Speith et al. (1995), which was adapted for negative values of the spin. Although the effects of negative spin are automatically taken into account correctly in most cases by the sign of a , three minor but important changes were required to the following Fortran functions:

DEFPAR calculates the radius of marginal stability according to Eq. 2.29. It has been adjusted to take the lower sign into account, too, in order to return the correct radius also in the case of negative spin.

GINVRS uses Eq. 3.7 to calculate λ for a certain r_e . It was modified to take the change in coordinates from the transition of positive to negative spin into account, meaning that the function $\beta(a)$ is properly included.

INTGVT integrates the angular part of the equation of motion (Eq. 2.31). The numerical integration chosen by Speith et al. (1995) has to be changed to

$$\text{INTGVT} = \frac{1}{2|a|} \int_{-1}^{+1} \sqrt{d\eta} \sqrt{\eta^2 \eta_{\text{max}}^2 - \eta_{\text{min}}^2} \sqrt{1 - \eta^2} \pm \frac{1}{|a|} \int_0^{\sqrt{\eta_{\text{max}} - \eta_0}} \frac{2d\eta}{\sqrt{(2\eta_{\text{max}} - \eta^2)((\eta_{\text{max}} - \eta^2)^2 - \eta_{\text{min}}^2)}} \quad (3.22)$$

where

$$\eta_{\text{max/min}} = \frac{1}{2a^2} \left[a^2 - q^2 - \lambda^2 \pm \sqrt{(a^2 - q^2 - \lambda^2)^2 + 4a^2 q^2} \right] \quad (3.23)$$

The upper sign of Eq. 3.22 is taken if no turning point in θ -direction exists. In the original version of the code taking the absolute value of a was not necessary, as a was positive by definition.

3.2 IMAGING THE ACCRETION DISK

The above presented equations and numerical techniques now allow to trace any photon from the accretion disk to the observer. Before integrating over all the photons emerging from the disk in order to calculate line profiles, we reconstruct the image of the accretion disk as seen by a distant observer. Hence, we use the α and β parameters (see Eq. 3.16), which are defined on a plane perpendicular to the line of sight (Fig. 3.3). As these parameters are defined in flat space, we obtain an image of the photons after being relativistically distorted and therefore are able to visualize the relativistic light bending effects. Images of this kind and more details on constructing them can already be found in literature, e.g., in Cunningham & Bardeen (1973), Luminet (1979), Hollywood & Melia (1997), Falcke et al. (2000), and Beckwith & Done (2004) to name some. All figures discussed in the following are for an accretion disk with an outer radius of $60r_g$ around a maximally rotating black hole ($a = 0.998$). The inner edge of the disk coincides with the radius of marginal stability, i.e., $r_{\text{in}} = 1.24r_g$.

Figure 3.2 already showed a map of the accretion disk for $\theta_0 = 40^\circ$, in order to illustrate the energy shift and how it varies over the disk. The motion of the accretion disk is clearly visible: the left part, which is blue-shifted, moves towards the observer, whereas the right part recedes, respectively. Additionally slight asymmetries due to light bending can already be observed. When looking close enough on the image, it can be seen that the back of the accretion disk (the upper one in the image) seems to be a little bit larger. This is due to the light bending, which makes this part of the disk look like we would observe it under a smaller inclination angle. This effect is strongly enhanced for an inclination of $\theta_0 = 80^\circ$ (Fig. 3.4). Additionally it reveals that not all of the back of the disk is flipped up equally, but that the photons emitted directly behind the black hole are deflected most. Moreover a slight asymmetry due to the frame-dragging of the black hole's rotation can be observed. This influences the photons at the inner radii of the disk most strongly. In the zoomed image one can see that the black hole actually seems to be situated in the lower left corner inside the disk and clearly not centered.

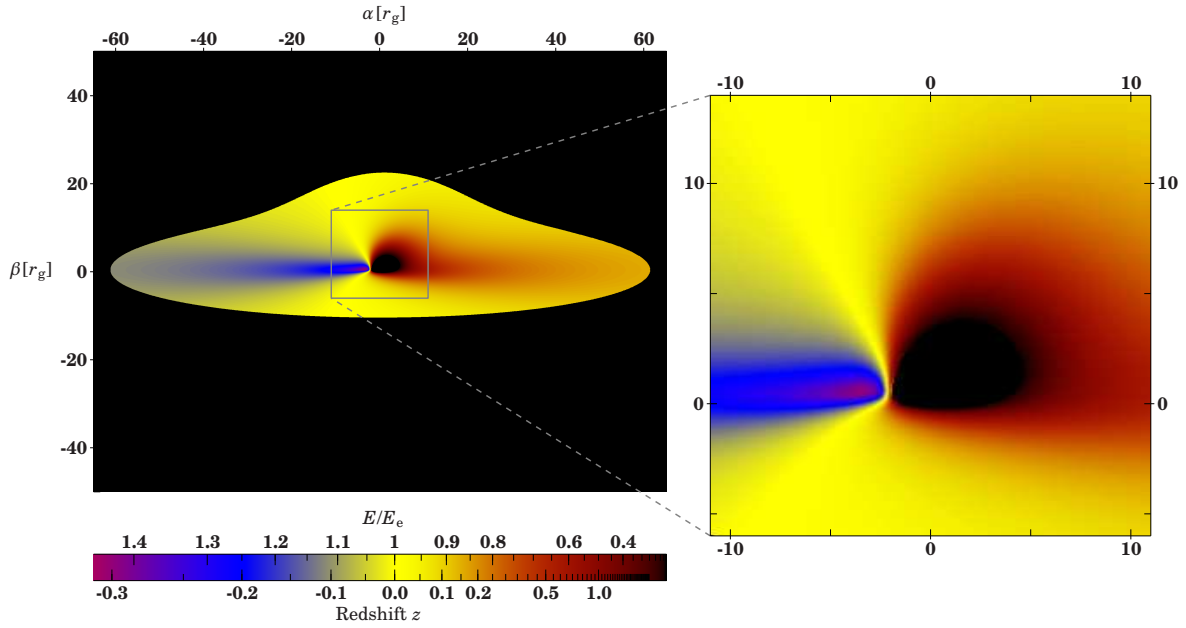


Fig. 3.4: Same as Fig. 3.2, but showing the energy shifts of the photons for an inclination of 80° . The color scheme reflects the direction of the energy shift, i.e., red illustrates a shift to lower energies and blue a shift to higher energies, respectively. Note how the light bending serves to virtually flip the disk behind the black hole upwards.

The energy shift due to Doppler effect is expected to be larger in the case of high inclinations, as the projected velocity of the particles in the disk is higher. And indeed, the maximal energy shifts are $g_{\max}(40^\circ) \approx 1.1$ and $g_{\max}(80^\circ) \approx 1.4$. Note that the absolute values of the energy shift do not coincide with the pure Doppler shift, but gravitational redshift and other spin dependent effects contribute, too. Nevertheless, the change in energy shift with inclination can be compared, as the other effects named above do not depend on the angle. In fact, the gravitational redshift gets extremely strong close to the black hole. As can be seen in Fig. 3.2 and Fig. 3.4, no blue-shifted photons are observed from the very inner part of the accretion disk, despite the relativistic movement of the emitting particles towards the observer.

The other interesting parameter characterizing a photon when emitted from the disk, is the emission angle θ_e (see Eq. 3.10 for a definition). Figure 3.5 shows θ_e for inclinations of $\theta_o = 40^\circ$ and $\theta_o = 80^\circ$. The shape of the disk itself does not deviate from Fig. 3.2 and Fig. 3.4, as the photon trajectories stay the same. Hence, we will only concentrate on the effects of the viewing angle on θ_e . For both inclinations, the emission angle converges towards θ_o at sufficiently large distances from the black hole. This behavior is good, as $\theta_e \approx \theta_o$ implies that the photon flies on a straight trajectory to the observer. Especially for $\theta_o = 40^\circ$, slight differences at larger distances are visible between the left and the right part, because of the rotation of the accretion disk. The rotation plays a role here, as θ_e is measured in the rest frame of the disk and hence also depends of the motion of the particle with respect to the observer. Looking at the zoomed images in Fig. 3.5, the profile varies more strongly close to the black hole and the angle takes almost all values between 0° and 90° . In greater detail, θ_e is much lower than the inclination for photons emitted behind the black hole, as light bending affects the photon trajectories in this case most. Even for $\theta_o = 80^\circ$, the emission angle gets close to 0° for a small part of the disk. Again due to the rotation of the disk and also the rotation of the black hole, this effect is

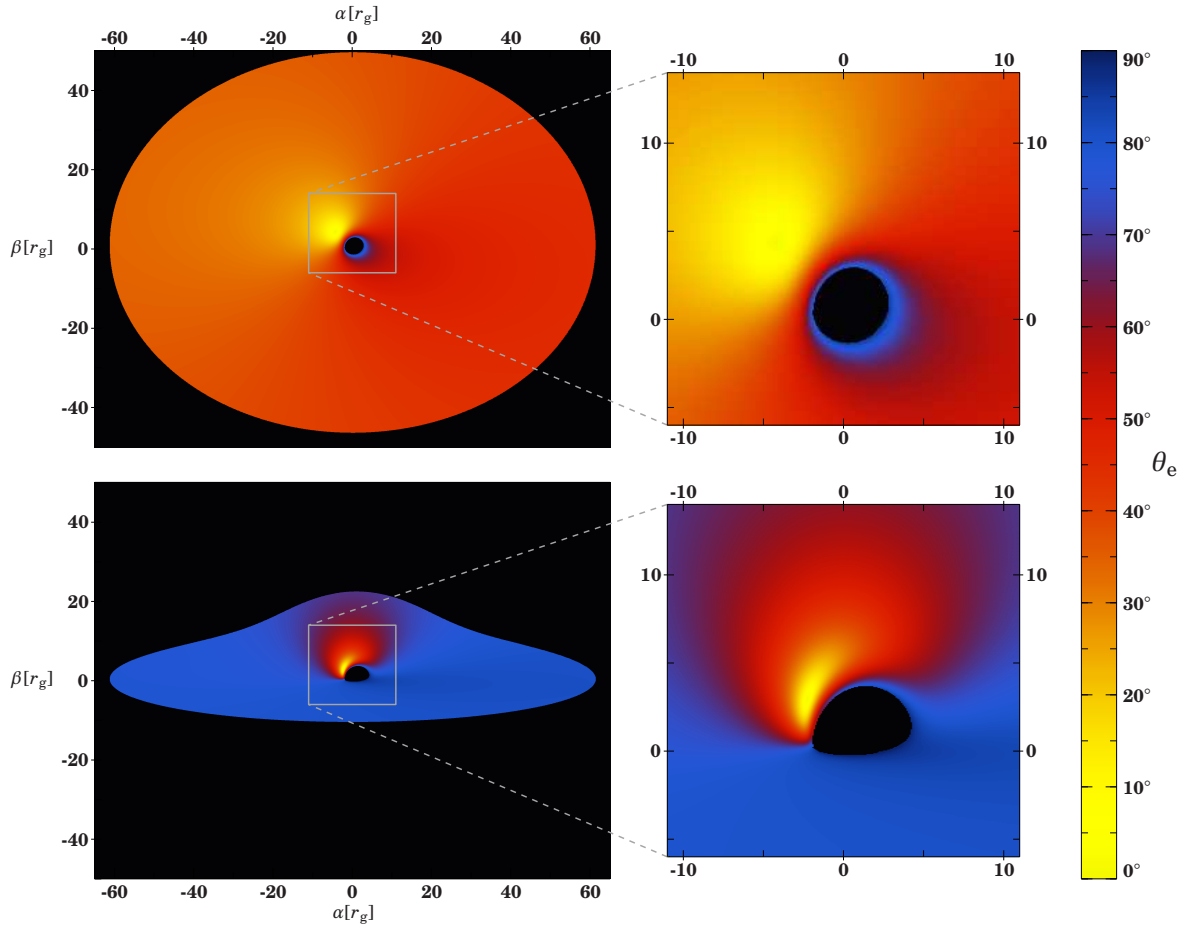


Fig. 3.5: Map of an accretion disk showing the emission angles, θ_e , for which the photons reach the observer under $\theta_o = 40^\circ$ (upper panel) and $\theta_o = 80^\circ$ (lower panel). See also Figs. 3.2 and 3.4, and the text for explanation concerning the distorted shape of the accretion disk.

stronger for particles moving towards the observer and in the rotational direction of the black hole. Therefore the region of low emission angles is in both cases shifted asymmetrically to the left. Additionally there is also a region of relatively high emission angles at the innermost radii of the disk. This is best seen for $\theta_o = 40^\circ$ in form of the blue ring, as in this case the average emission angle is much steeper.

Although most of the emission angles are close to the viewing angle, taking this effect correctly into account is important, as most of the emitted photons originate from the innermost regions of the disk, assuming $I \propto r^{-3}$ for a standard Shakura & Sunyaev (1973) disk. Hence, also the dependency of the intensity on the emission angle needs to be treated thoroughly.

3.3 UNDERSTANDING THE LINE PROFILE

In order to get from the picture of the accretion disk to a line profile, we can use similar numerical techniques. As we are now interested in the intensity, we assume an intrinsic intensity profile of the accretion disk in form of a narrow Gaussian line. Then we are ready to perform the integration over the disk, i.e., solve Eq. 3.14. Fig. 3.6 shows how the resulting line profiles

look like. Additionally, this section should motivate the relation between the line shape and the physical system, consisting of the black hole and the accretion disk. Hence we will examine in detail the changes in shape that parameters like the spin or the inclination angle induce. Moreover the physical reason for the shape is motivated.

All plotted data are simulated for a narrow Gaussian emission line with a width of $0.01E_e$. We assume $E_e = 6.4\text{keV}$ from the neutral $K\alpha$ transition (dashed gray line) in the rest frame of the disk. All emission profiles are chosen to be in the form of $r^{-\alpha}$, as currently available models use this parametrization (e.g., Fabian et al., 1989; Laor, 1991; Dovčiak et al., 2004). The accretion disk extends from the radius of marginal stability up to $50r_g$. All emission lines are normalized to have the same flux, i.e., the area below each curve is the same.

Figure 3.6a shows the line profile for different viewing angles θ_o . Here the emissivity ($\alpha = 0.5$) and the spin of the black hole ($a = 0.998$) are chosen to be constant. What immediately catches the eye is that all lines are somehow double-peaked, i.e., there exists a blue- and a redshifted peak with respect to the rest wavelength. The reason for this is obviously the Doppler effect, as for $\theta_o = 0^\circ$, some part the disk moving towards the observer (photons are blue-shifted) and another part moving away (photons are redshifted). Hence it is clear that for the special case $\theta_o = 0^\circ$ only one peak is visible, as the observer looks face-on onto the disk and no particles are moving in his/her direction. Overall, the lines are shifted to lower energies, as the photons have to escape from the deep gravitational potential induced by the black hole (see Sec. 3.1). Moreover it is quite striking that for higher inclination angles the blue peak is always stronger than the red one. This is also readily explained, as the material in the inner disk moves with relativistic velocities. Hence, we would expect a “boost” in intensity, if the emitter is flying towards the observer. Additionally the distance between the two peaks grows with the viewing angle. Although the speed of the disk is not varied, the observer only notices the effects of the projected velocity of the particles onto the line of sight, which is related to the real velocity by $\cos\theta_o$. Hence, under lower inclination angles the particles seem to move slower and therefore the photon energies are shifted less strongly.

Fig. 3.6b shows how the emissivity of the accretion disk influences the line profile. For clarification some intensity profiles $r^{-\alpha}$ are illustrated in the left panel, where one can clearly see what the emissivity means: For larger values, more photons emerge from the highly relativistic inner regions of the accretion disk. The evolution of the line profile with the emissivity index α in the right panel is dominated by this feature. For increasing emissivities a greater amount of flux is present in the red wing of the emission line. This increase is due to the larger fraction of photons being emitted at the region very close to the black hole, which are all highly redshifted. As can be seen in Fig. 3.2, even photons emitted by particles moving towards the observer are redshifted. Additionally the red peak slowly vanishes and the blue peak gets weak with respect to the rest of the line. All these effects change the line from a double peaked shape, to an asymmetric emission line extending to even lower energies. More generally, the emissivity of the disk depends on the incident spectrum on the accretion disk. The photons also get relativistically distorted after being emitted at the hard X-ray source, which leads to a characteristic spectrum in the rest frame of the disk and therefore a characteristic emissivity. Hence, the strong dependence of the line shape on the emissivity might offer a way to constrain the geometry of the system.

The major effect of the spin on the line profile is its influence on the inner edge of the disk. Other effects due to an influence of the metric itself on the photons will be considered in Sec. 3.4. Figure 3.6c compares profiles for different spins from maximally negative to maximally positive, for an inclination angle of $\theta_o = 40^\circ$ and an emissivity of $\alpha = 3$. This is a very common parameter combination found in observations. The panel on the left hand side illus-

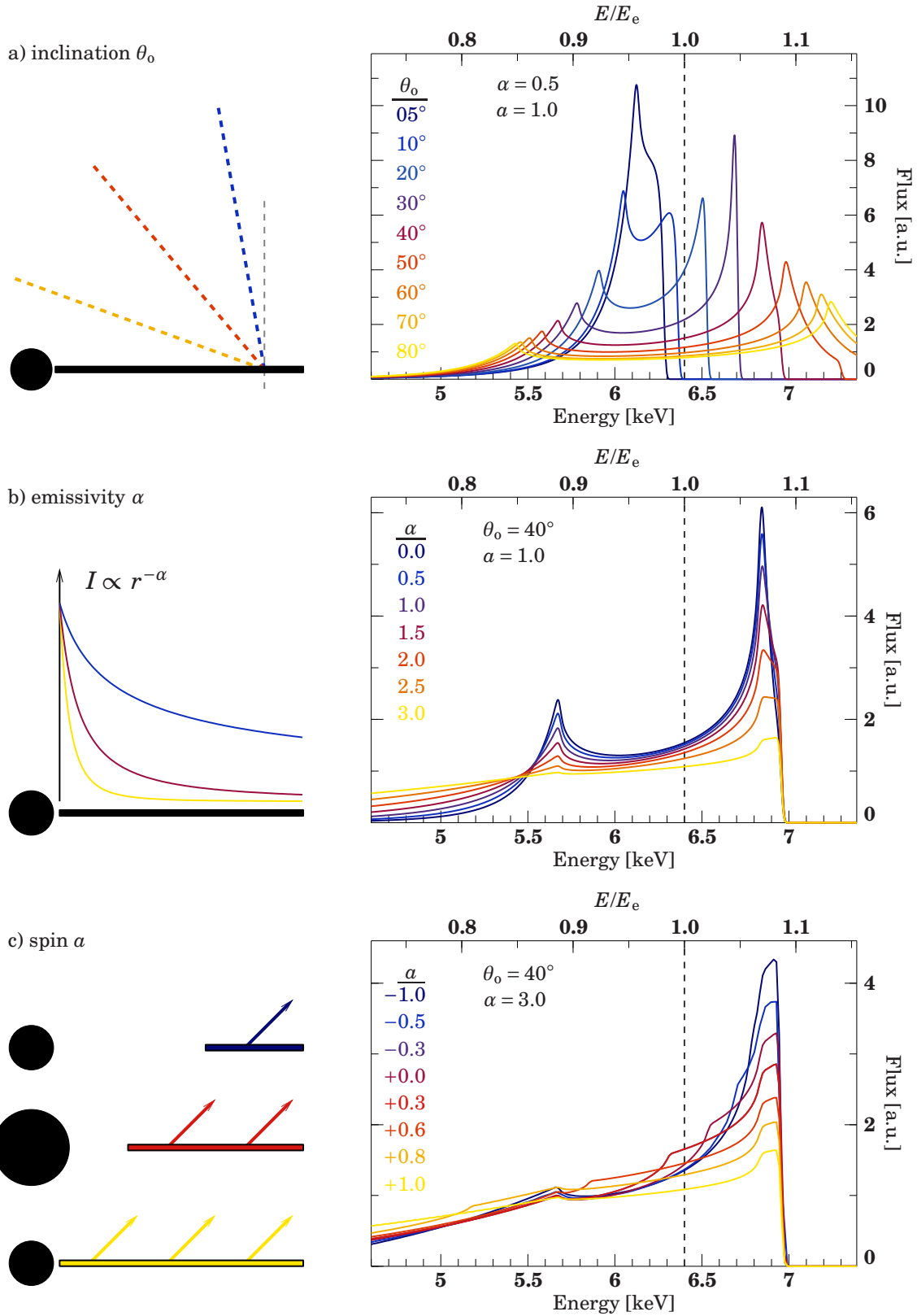


Fig. 3.6: The shape of broad lines for different a) inclinations θ , b) emissivities α , and c) spins a . For each sub figure, the left panel sketches what the variation of the specific parameter means. The label $a = \pm 1.0$ stands for the maximal value of the spin, i.e., in our case $a = \pm 0.998$.

trates how the inner edge moves from $r_{\text{in}}(a = -0.998) \approx 9r_g$ to $r_{\text{in}}(a \approx +0.998) = 1.24r_g$ (see Eq. 2.29). Note how the event horizon of the black hole increases for $|a| \rightarrow 0$. The arrows on the disk should mimic the photons emerging from the disk. It is clearly visible that due to a larger inner radius of the disk, less photons are emitted in the region very close to the black hole. Hence there are less strongly redshifted photons from this emission line present in the spectrum. This explains the evolution towards narrower lines for a highly negatively spinning black hole. Note that the shape and position of the blue peak is unaffected by this process, although its strength increases with respect to the wing of the line. Moreover it should be noted that although the accretion disk might physically reach down to the radius of marginal stability, the broad line only probes the region of fluorescent emission. But if the inner regions are fully ionized, no electrons remain to produce fluorescent emission and therefore we would measure a larger effective inner radius of the accretion disk (see, e.g., Ross & Fabian, 2005). If we have to drop this assumption, the minor effects of the spin only depending on the influence of the metric on the photons are the only ones left to actually measure the spin. Additionally, recent magneto-hydrodynamic simulations show that emission from the “plunging region”, which is the region between the inner edge of the disk and the event horizon, might be enhanced due to trapping of the magnetic flux (Reynolds et al., 2006). Hence, part of the observed emission does not originate from the accretion disk, which again conflicts with the assumption $r_{\text{in}} = r_{\text{ms}}$.

Another effect not so easily visible, but nevertheless necessary for a correct treatment, is the choice of the angular dependency $\epsilon(\theta_e)$ of the emitted intensity from the accretion disk. A careful treatment of this aspect is given by Svoboda et al. (2009a). The baseline is that in general one would expect a slight limb-brightening in typical accretion disks, i.e., emission for high θ_e is more probable. Therefore the limb-darkening used by Laor (1991) and the also limb-brightening suggested by Haardt (1993) give slightly wrong results for the line profile and bias model fitting. As suggested by the simulations of Svoboda et al. (2009a), using isotropic emission for data analysis leads to the least bias in other fitting parameters, as the available limb-brightening of Haardt (1993) overestimates the actual strength of brightening.

Summarizing the effects the different parameters have on the line shape, one notices the huge amount of different parameters the shape depends on. Hence the space for predictions by analyzing such broad line features is enormous. Nevertheless, one would need excellent data quality, which is not available at the moment, to make use of all of these features. As the differences in line shape are quite small for some parameters (e.g., the outer radius), assumptions have to be made in order to be able to obtain reasonable fitting results, e.g., that the disk extends down to the radius of marginal stability. But if we do so, we can get a grip on very important parameters like the spin, the inclination, and the emissivity, and therefore maybe the geometry of the system.

3.4 NEGATIVELY SPINNING BLACK HOLES

In addition to affect the stability of particle orbits (see above), and thus the inner radius of the accretion disk, a negatively spinning black hole also influences the photons directly. This effect solely on the photons can be visualized when simulating the very same accretion disk for different spins. In practice this means setting the inner radius of the accretion disk to $9r_g$, which is the inner edge of an accretion disk around a black hole with maximal negative spin. The following section is a detailed explanation of this topic, which has already been published (Dauser et al., 2010). In Fig. 3.7 we compare the line profiles for a maximally rotating

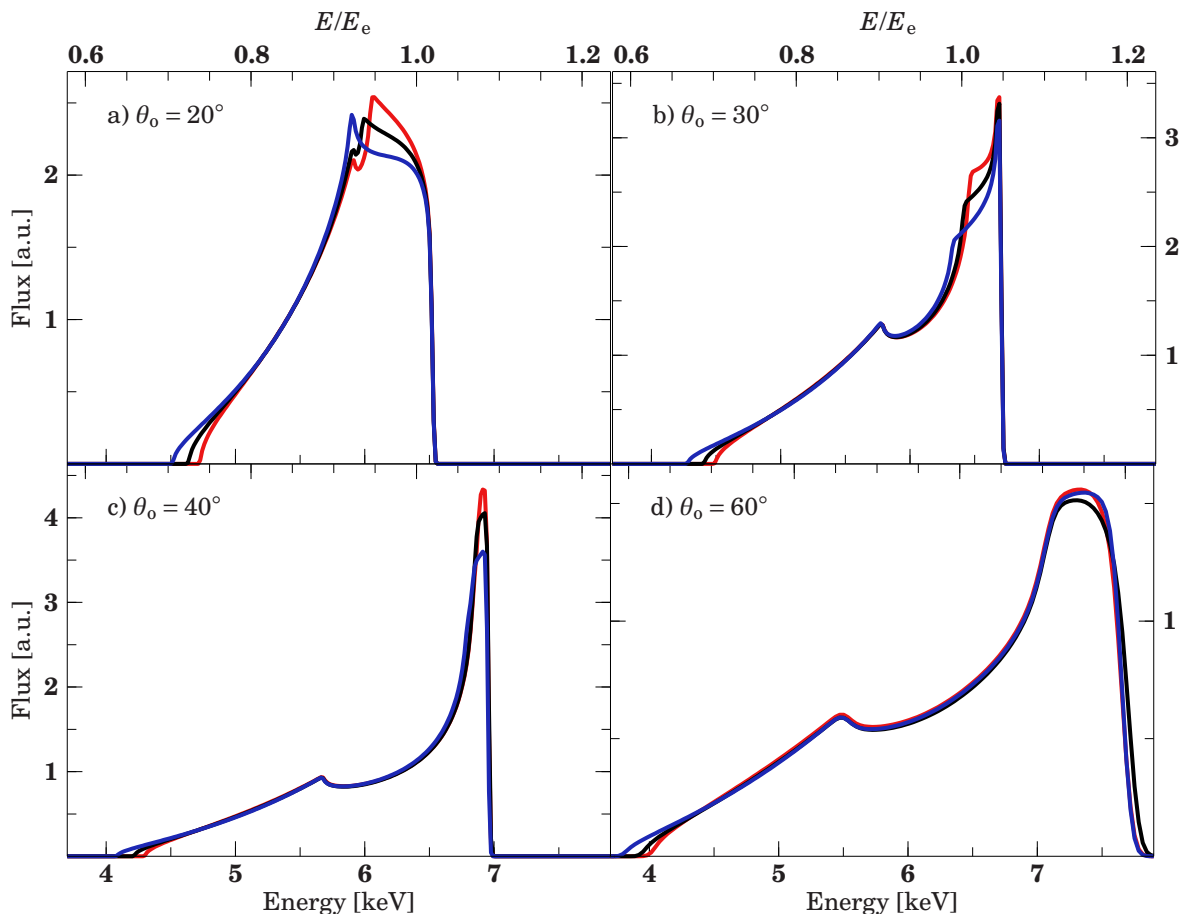


Fig. 3.7: Line profiles of a relativistic iron line emitted at 6.4 keV in the rest-frame of the disk (Dauser et al., 2010, Fig. 3). Typical inclination angles θ_0 are displayed along with an emissivity of r^{-3} . The maximally spinning black hole ($a = +0.998$) is drawn in red, the non-rotating ($a = 0$) in black, and the blue line shows the broad emission line for maximal negative spin ($a = -0.998$). In order to allow for a comparison of the line shapes, the inner edge of the accretion disk was set to $r = 9r_g$ for all profiles.

Kerr black hole, a Schwarzschild black hole, and a black hole which is maximally counter-rotating for several different inclinations. The accretion disk emissivity was assumed to be $I_{E_e} \propto r^{-3}$, i.e., the emissivity obtained from a simple accretion disk in the Newtonian regime (Shakura & Sunyaev, 1973). In order to allow for a comparison of the line shapes with earlier results, we use the limb-darkening law of Laor (1991), even though for lines caused by fluorescence due to the irradiation of a disk with hard X-rays from above, a limb-brightening law would be more appropriate (Svoboda et al., 2009a). The figure shows that the major difference between the different spins for the same accretion disk is the strength of the core of the line relative to the red wing, which decreases with decreasing a . For this case of a large inner radius, the most significant differences in line shape are seen for low values of θ_0 while the red tails are virtually indistinguishable. The slight increase in line flux at the lowest energies is due to the increased Doppler boosting in the case of $a < 0$ (for a given radius, the angular velocity Ω increases with decreasing a , Eq. 2.4).

The difference in energy shift of photons emerging from an accretion disk between maximal

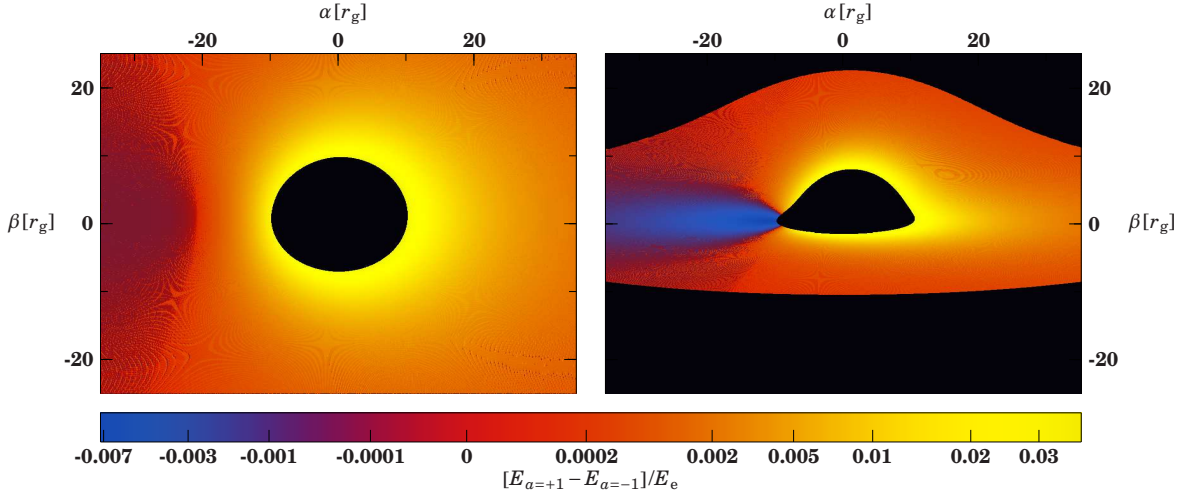


Fig. 3.8: Difference between the energy shifts experienced by photons from a maximally positively and a maximally negatively spinning accretion disk with inner radius $r_{\text{in}} = 9r_g$, viewed under an inclination of 40° (left panel) and 80° (right panel).

positive and maximal negative spin of the black hole is shown in Fig. 3.8. In general these differences are low and reach at maximum of $\approx 0.2\text{keV}$ in the case of the neutral $K\alpha$ line with an energy of $E_e = 6.4\text{keV}$. The largest differences appear close to the inner edge of the accretion disk in a way that the photons from negatively spinning systems are shifted more strongly to lower energies. As these differences are largest close to the inner edge of the disk, a higher emissivity enhances the deviations in the line profiles. In the equation defining the energy shift g (Eq. 3.7), we already derived that photons emitted from a counterrotating disk viewed face-on are less strongly redshifted. Despite this trend, overall these photons are more strongly redshifted for the inclinations shown in the image. Hence the energy shift of the photons has to be dominated by the influence of the effective velocity of the accretion disk, as seen by the observer. In the left part of the disk, which is already mainly blue-shifted due to its movement towards the observer, a slight increase in energy shift is evident for negative spin. Similarly the right part is more strongly redshifted in the case of a negatively spinning black hole. Summarizing, the most important implication of negative spin on the energy shift is a faster rotation of the accretion disk (Eq. 2.4) and therefore a stronger Doppler boost of the emitted photons, compared to a positively spinning black hole. Additionally, the overall energy shift is towards lower energies in the case of a negatively spinning black hole, which can be seen in the increase in flux at the lower end of line profiles, too (Fig. 3.7). As the largest energy shifts take place close to the inner edge of the disk, the differences in line shape between positive and negative spin are enhanced by an increasing emissivity.

Figure 3.9 shows line profiles for different spins of the black hole for the more realistic case that the disk extends down to the marginally stable orbit. Since the inner edge of the disk is closer to the black hole for positively spinning black holes, more strongly redshifted photons emerge. As already noted by Jaroszynski (1997), this leads to broader lines in these systems, especially for disks with an emissivity that is strongly peaked towards r_{in} . Maximally negatively spinning black holes have the smallest width, although the line will still be detectable as being broad even at CCD resolution (depending on inclination, typical widths of the main peak are around 200eV). Lines from counterrotating black holes will therefore be more difficult to detect than lines from positively rotating black holes.

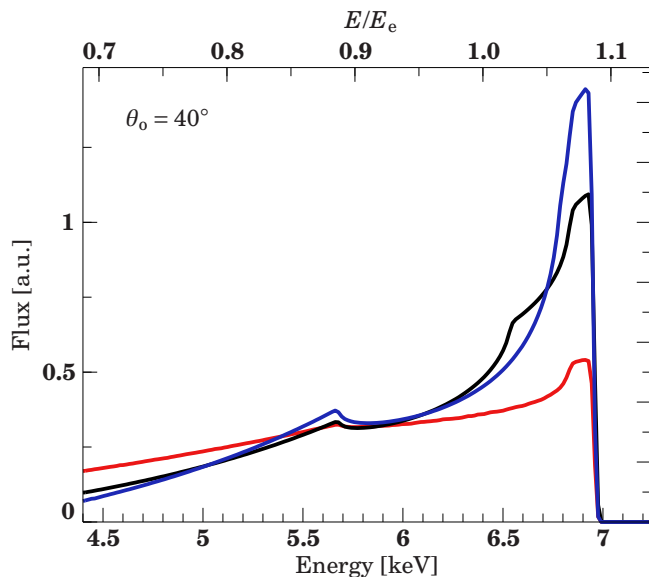


Fig. 3.9: A broadened emission line with $E_e = 6.4\text{keV}$ for different spins of the black hole, emerging from an accretion disk which is assumed to extend down to the marginal stable radius (Dauser et al., 2010, Fig. 5). Common parameters were chosen for the inclination angle ($\theta_0 = 40^\circ$) and the emissivity (r^{-3}). The color code is that of Fig. 3.7, i.e., $a = +0.998$ is drawn in red, $a = 0$ in black, and $a = -0.998$ in blue.

The major difference of line shapes for disks around black holes with $a = 0$ and counterrotating disks (see Fig. 3.9) lies in the strength of the blue peak, since the skew symmetric shape is mainly due to frame dragging effects and the small inner radii. Detecting these lines observationally is therefore more difficult than detecting lines from disks around positively rotating black holes. In addition, as shown by Svoboda et al. (2009a), limb-darkening-/brightening affects the strength of the red wing. For counterrotating black holes, this results in a possible degeneracy, as for different limb-darkening laws similar line shapes might result for $a \sim 0$ and $a = -0.998$. Using a physically motivated limb-darkening law would avoid this degeneracy. The line shapes also become more similar if the assumption that emission down to the radius of marginal stability contributes to the shape is dropped. This assumption might not be justified in some cases, as fluorescent emission only takes place in irradiated parts of the disk which are not fully ionized. Thus the inner radius of the emission becomes larger, which results in a weaker red tail of the line profile. This effect leads to line shapes for different spin that are more similar and closer to the ones in Fig. 3.7.

In order to study the question of observability in greater detail, we have performed simulations of observations of a relativistic line with the planned *International X-ray Observatory* (*IXO*), using response matrices obtained from the *IXO* team (Smith, priv. comm.). We base the simulations on power-law fits to *XMM-Newton* data from MCG-6-30-15 in a typical state, using a power law continuum with a 2–10 keV flux of $2.5 \times 10^{-11} \text{erg cm}^{-2} \text{s}^{-1}$ and photon index $\Gamma = 1.6$, absorbed by a column $N_{\text{H}} = 10^{21} \text{cm}^{-2}$. We set the equivalent width of the line to 350 eV (typical for MCG-6-30-15). Figure 3.10 shows that in a 50 ksec observation the next generation X-ray instrumentation will easily allow to separate even the difficult case of negatively spinning black holes. Note that this is only valid for the assumption that the accretion disk extends down to r_{ms} . If this inner radius and the spin are fitted independently, even long observations by *IXO* will not succeed in constraining the spin.

3.5 DIFFERENT MODELS

In the following section, the different models and their approximations are presented. They are all designed to fit spectra, which sets the upper limit of the duration of one line calculation.

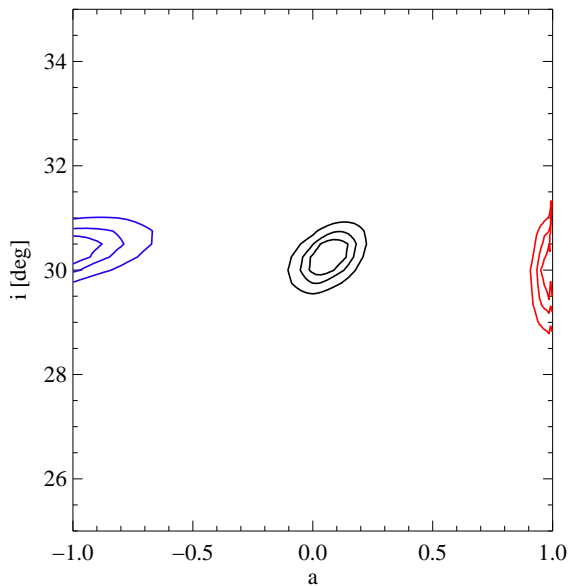


Fig. 3.10: Confidence contours for simulated 50 ksec observations of MCG-6-30-15 with IXO. Confidence contours at 68%, 90% and 99% confidence are shown for three simulations assuming $a = -0.998$, $a = 0$, and $a = +0.998$, respectively (Dauser et al., 2010, Fig. 6).

This is compared to exact simulations of the line shape, which usually last around three orders of magnitude longer. All models are normalized such that the area below each curve for a specific inclination angle is the same. Besides the analytic diskline model (Fabian et al., 1989), which is calculated for the special case of $a = 0$, all other models for broad emission lines use large tables of precalculated values. These are necessary, as solving the equation of motion numerically is a very time-consuming process. Hence the outcome of these simulation is stored in huge tables for various combinations of the desired parameters a , θ_o , and r_e . The relativistic line shape is then calculated by interpolating the values in the table. The models differ in the size of their tables, the interpolation techniques and also in the type of information stored in the table. The most commonly used models will be presented in the following.

A comparison of popular models for different inclination angles and emissivities to exact profiles can be found in Fig. 3.11 and Fig. 3.12, respectively. All profiles are calculated for a maximally rotating black hole ($a = 0.998$). Furthermore photons from the radius of marginal stability $r_{ms} = 1.24 r_g$ down to $r = 50 r_g$ are used when integrating the line profile. Additionally the exact simulation uses a Gaussian emission line at $E_e = 6.4 \text{ keV}$ with a narrow width of $\sigma = 0.01 E_e$ in the rest frame of the disk.

3.5.1 THE LAOR MODEL

The majority of publications for measuring the black hole's spin use the laor-model (Laor, 1991), which was the first model valid for a spinning black hole and was derived for a fixed $a = 0.998$. This assumption clearly limits the possibilities and does not allow for a direct determination of the black hole spin (but see, Svoboda et al., 2009b). Moreover the angular directionality law was taken to be a limb-darkening law. Only a small grid of transfer functions is integrated in the model. Figure 3.11a shows a comparison for different viewing angles θ_o to the exact calculation. Although the line shape seems crude, it at least approximately fits the exact calculation, as the position of the peaks is correct. In contrast to that the model is not able to describe any of the blue peaks correctly. For lower angles, where the peaks become narrower and stronger, the laor model lacks to describe the dynamic features totally. Despite

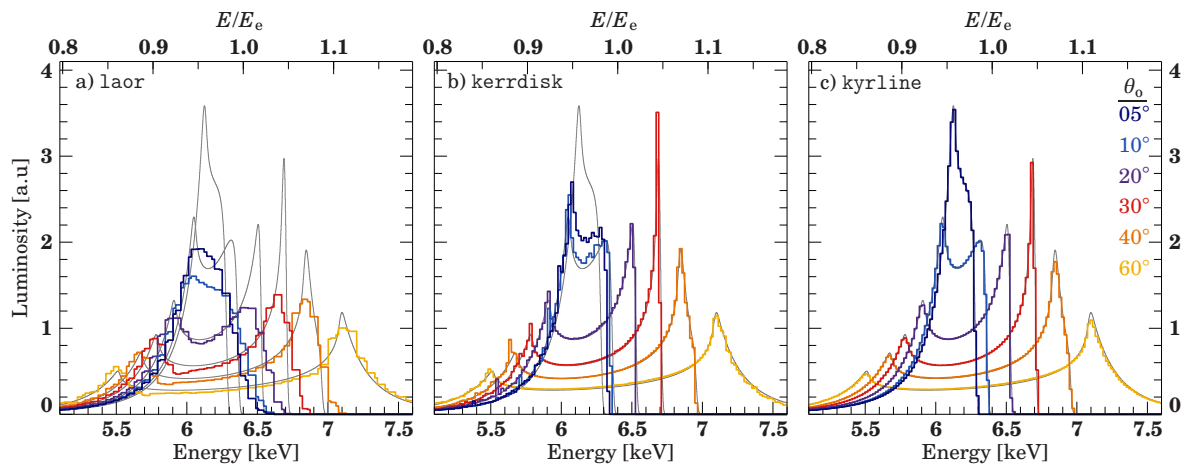


Fig. 3.11: Comparison of models for relativistic lines for different inclination angles θ_0 , with an exact calculation (gray) for an emissivity $\alpha = 0.5$ and spin $a = 0.998$.

strong differences between $\theta = 5^\circ$ and $\theta = 10^\circ$ in the exact model, there is hardly any difference in the model, i.e., a low viewing angle will not be well constrained during fitting and might influence other fitting parameters in the wrong way. Figure 3.12a reveals that for higher emissivities the laor-model is able to describe the overall line profile better, as the line shape gets smoother. Note that although not constrained by the bin size, the sharp edge to the right of the blue peak is predicted too smooth for all emissivities. Because of the above reasons, the laor-model should not be used for fitting high resolution data from *XMM-Newton*, *Chandra*, or *Suzaku*, although it is available in the standard XSPEC package.

3.5.2 THE KYRLINE MODEL

Dovčiak et al. (2004) designed the kyrline model, which uses a huge tables of transfer functions. This approach serves to calculate the line shape quickly, without strong interpolation but with a much higher resolution than laor. Additionally, a is variable for fitting the spin of a black hole from 0 to 1. The comparison for different inclination angles with our calculations can be seen in Fig. 3.11c. The model fits the exact calculation for all inclination angles and even at the narrow peaks very well. Also for all reasonable emissivities, the model perfectly follows the exact line shape, as can be seen in Fig. 3.12c. Moreover kyrline provides different angular directionalities of the emitted radiation, namely isotropic, limb-darkening and limb-brightening. In order to achieve this, a large table for each of them is calculated, as the angular integration is hard-coded in the table. But the comparison proves that the model can be used for fitting high resolution data without restrictions.

3.5.3 THE KERRDISK MODEL

Stating that the kyrline model of Dovčiak et al. (2004) is too large and still not smooth, Brenneman & Reynolds (2006) presented a model, which uses a comparably small sized table and strong interpolation techniques. The fact that the transfer function is very smooth allows them to strongly interpolate it. Moreover a different approach, which is more flexible, is used here: The narrow emission line in the rest frame of the disk is not chosen to be a Gaussian, but approximated by a δ -function. This allows them to perform a greater part of the

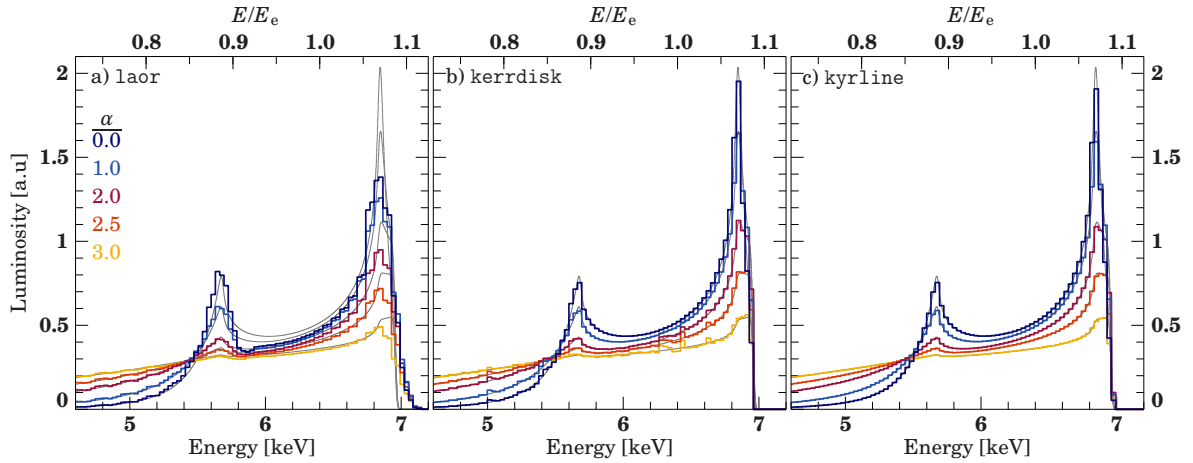


Fig. 3.12: Popular line models for different emissivities α are compared to the exact calculation (gray) for an inclination of $\theta = 40^\circ$ and spin $a = 0.998$.

integration analytically. In the end this means that the angular emissivity law is not encoded in the calculated table, but can even be changed in principle during fitting. All in all this serves to reduce the size of the table to only a fraction of the kyrline-table. The kerrdisk model is plotted in Fig. 3.11b and Fig 3.12b. The line profile does not look as smooth as kyrline, but exhibits spikes which can be seen best in the red wing of the lines. However, if the line is evaluated on an energy grid appropriate for a Silicon detector, these spikes will be averaged out and therefore have no effect on any of the published results. When evaluating the model on an even finer grid, much larger spikes appear (see Fig. 4.3). But as such a fine grid is far beyond any detector's resolution, they are of no importance for data modeling. In contrast to the laor model the overall shape of the emission line fits better and all dynamic features are captured. Not only more values are calculated, but also the peaks are more pronounced. Nevertheless, there are still larger deviations from the exact calculations for low inclination angles (Fig. 3.11b).

CHAPTER 4

THE RELLINE MODEL

As motivated in Sec. 1.3.3, we expect some sources to have negative spin. But although first calculations of line profiles for a negatively spinning black hole were already performed, e.g., by Jaroszynski (1997) and Schnittman (2006), none of the currently available models in X-ray spectral analysis programs like ISIS or XSPEC for relativistic lines such as diskline (Fabian et al., 1989), `laor` (Laor, 1991), `kerrdisk` (Brenneman & Reynolds, 2006), or the `ky`-family of models (Dovčiak et al., 2004), are valid for black holes with retrograde accretion disks. However, a further exploration of this feature requires fully-relativistic broad emission line models that are valid for retrograde black holes as well. Therefore the formalism of Cunningham (1975) employed by many of these models was extended in this work to the case of $-0.998 \leq a \leq +0.998$. The implementation of the model is called `relline` and was already published (Dauser et al., 2010). The following chapter presents a detailed overview of the model.

4.1 NUMERICAL IMPLEMENTATION

The effort to calculate line profiles is almost fully buried in the determination of the transfer function, which depends in general on four parameters (a , θ_o , r_e , and g). In order to allow for a real-time fitting of observational data it is generally necessary to precalculate the transfer function f (Eq. 3.13) or some variant of it. The quality of a given model then depends strongly on the amount of precalculated information. Table sizes can amount up to several hundreds of megabytes.

In most available models, the chosen approach is to precalculate the value of the inner integral in Eq. 3.14 using a Gaussian line shape for I_{E_e} and some prescription of the limb-darkening law, i.e., the dependence of I_{E_e} from θ_e . A disadvantage of this strategy is that any change of the limb-darkening law necessitates a recomputation of the precalculated tables. In order to avoid this problem, we use a Green's function approach to model the specific intensity originating from the disk as purely mono-energetic at E_e ,

$$I_E(r_e, \theta_e, E_e) = \delta(E - E_e) I_{E_e}(r_e, \theta_e) \quad , \quad (4.1)$$

The dependencies of the local intensity on the emission angle θ_e (e.g., limb darkening effects) and the radius r_e are described by $I_{E_e}(r_e, \theta_e)$. This is the same strategy used by the `kerrdisk`-model (Brenneman & Reynolds, 2006). Inserting this into Eq. 3.14 and evaluating the delta

function then gives

$$I_E^{\text{obs}}(\theta_o) = \int_{r_{\text{in}}}^{r_{\text{out}}} \frac{\pi g^3 r_e f(g^*, r_e, \theta_o)}{E_e (g_{\text{max}} - g_{\text{in}}) \sqrt{g^* (1 - g^*)}} I_{E_e}(r_e, \theta_e) dr_e \quad (4.2)$$

where the transfer function f is again calculated using the code of Speith et al. (1995), adapted for negative spin.

As could be seen in Sec. 3.5, the kerrdisk model exhibits “spikes” for special parameter combinations (see also Fig.4.3). The origin of these spikes has now been understood and is a peculiarity of the Green’s function approach. This can be seen when looking closer at the emission of one radius r and its contribution $I_{E_i}^{\text{obs}}(r)$ to a certain energy bin i ranging from E_{l_0} to E_{h_i} . Using Eq. 4.2 this leads to

$$I_{E_i}^{\text{obs}}(r) \propto \int_{E_{l_0}}^{E_{h_i}} \frac{g^3 f(g^*)}{(g_{\text{max}} - g_{\text{min}}) \sqrt{g^* (1 - g^*)}} dE \quad , \quad (4.3)$$

where it can be seen that the integrand diverges at $g^* = 0$ and $g^* = 1$, i.e., at the two points on the ring where the minimum and maximum energy shifts occur with respect to E_e . Hence, for values of g^* very close to 0 or 1 the intensity is overestimated due to a numerical error. As the divergences imply that these points contribute significantly to the overall luminosity, great care has to be taken for the numerical integration. In order to avoid the problems seen in the kerrdisk model, we use a different approach, employing that the dependence of $f(g^*)$ (see Eq. 3.13) close to these points can be calculated analytically as

$$f(g^* \rightarrow 0) \propto \sqrt{1 - g^*} \quad \text{and} \quad f(g^* \rightarrow 1) \propto \sqrt{g^*} \quad . \quad (4.4)$$

This leaves the integrand of Eq. 4.3 with a divergence of the kind $1/\sqrt{x}$ for $x \rightarrow 0$. Assuming that $g \sim \text{const.}$ in this energy bin, the integration can be performed analytically, leading to

$$I_{E_i}^{\text{obs}}(r) \propto 2 \left(\sqrt{E_{h_i}} - \sqrt{E_{l_0}} \right) \quad . \quad (4.5)$$

As the above assumption might not be valid for the whole bin, we define a criterion by choosing a sufficiently small value of h such that it is legitimate to use Eq. 4.5 for $g^* \in [0, h]$ and $g^* \in [1 - h, 1]$. The normalization factors are then determined from $I_h^{\text{obs}}(r)$ and $I_{1-h}^{\text{obs}}(r)$. For $g^* \in [h, 1 - h]$, an adaptive Romberg method is chosen to solve Eq. 4.2 directly. Choosing a value of $h = 2 \cdot 10^{-3}$ serves to avoid the spikes and keep the advantages of the Green’s function approach (see Fig. 4.1).

In order to allow fast real time fitting of observational data, the important quantities like the transfer function f and the emission angle θ_e are stored in a table. The 22 MB sized table contains values for combinations of 30 different spins from $-0.998 \leq a \leq +0.998$ and 20 inclination angles from $0^\circ \leq \theta_o \leq 89^\circ$. For a given parameter combination (a, θ_o) , the other parameters, namely r_e , θ_e , and g , are interpolated. Hereby the grid of the spin is not equally spaced, but has smaller steps for $a \rightarrow 0.998$, as the transfer function changes more rapidly in this direction. The actual choice of the (a, θ_o) -grid has been tested intensively to guarantee a correct interpolation for the whole parameter space. For each combination of (a, θ_o) , a logarithmic grid of 100 radii from the ISCO to $1000 r_g$ models the accretion disk. For providing a smooth line profile, the *relline* model interpolates from these values onto an intrinsic grid with 2500 radial bins.

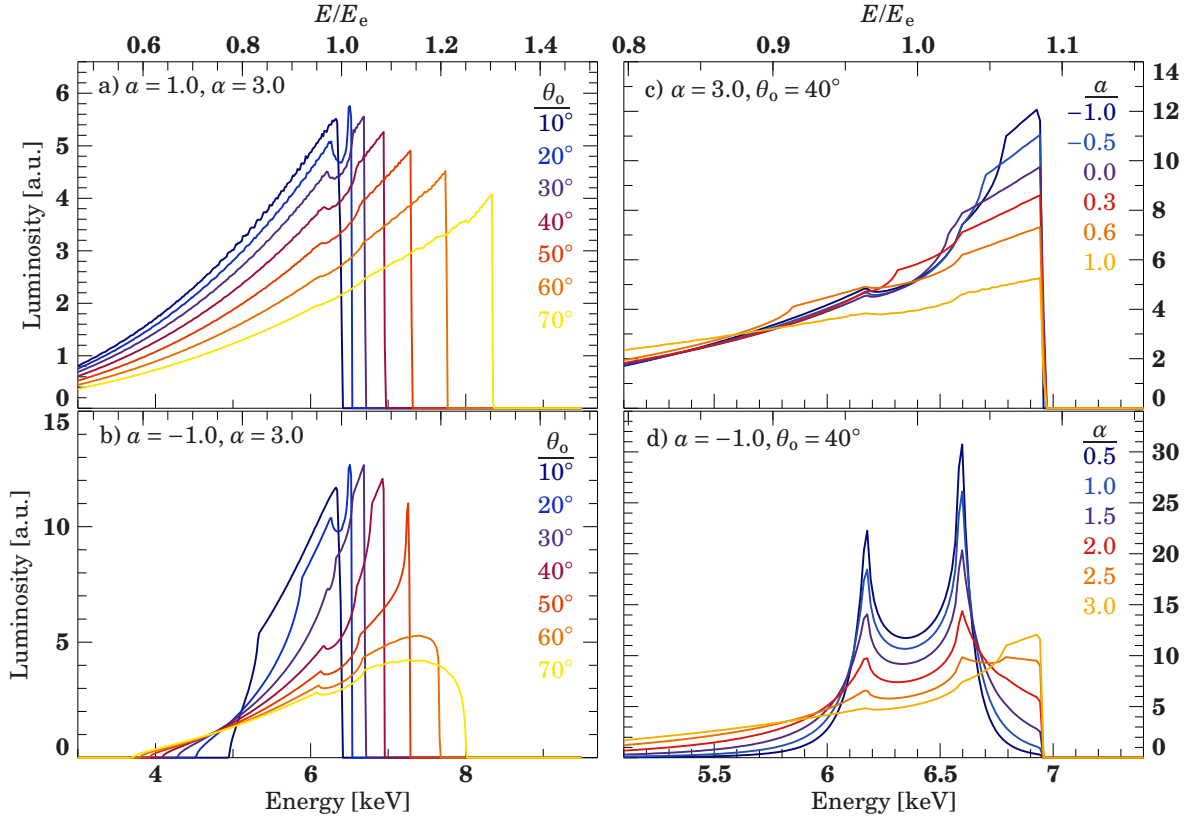


Fig. 4.1: Lines profiles for different combinations of inclination angles θ_o (a and b), spin a (c), and emissivity α (d) evaluated on a fine grid. The accretion disk truncates at $400r_g$, and the line energy is $E_e 6.4 \text{ keV}$. See the text for further details.

The emissivity of the emitted intensity is taken into account in form of a broken power law (similar to Dovčiak et al., 2004)

$$I \propto \begin{cases} r^{-\alpha_1} & \text{for } r \leq r_{\text{br}} \\ r^{-\alpha_2} & \text{for } r > r_{\text{br}} \end{cases} \quad (4.6)$$

This parametrization is used in all modern line models, but could be readily changed. Moreover, there are currently three angular directionality laws available: Isotropic emission, limb-darkening (Laor, 1991) and limb-brightening (Haardt, 1993). As explained above, our approach allows to take easily any other angular dependency into account. Finally the model integrates over all radii and returns the total intensity of the accretion disk.

Line profiles calculated with the `relline`-model for various parameter combinations are shown in Fig. 4.1. No spikes are visible at all, despite the highly resolved energy grid. Hence, the above described integration technique efficiently calculates the line without numerical divergences. Besides tiny wiggles in large red wings (Fig. 4.1a), the line shape is very smooth for the whole parameter range. These results show that by using special interpolation techniques, the small table covers the whole parameter range sufficiently in order to calculate profiles even much smoother than required for data analysis.

Figure 4.1a shows a typical case for maximal spin and $\alpha = 3$. As the disk reaches very close to the black hole, large red wings are seen for all inclination angles. This case is especially

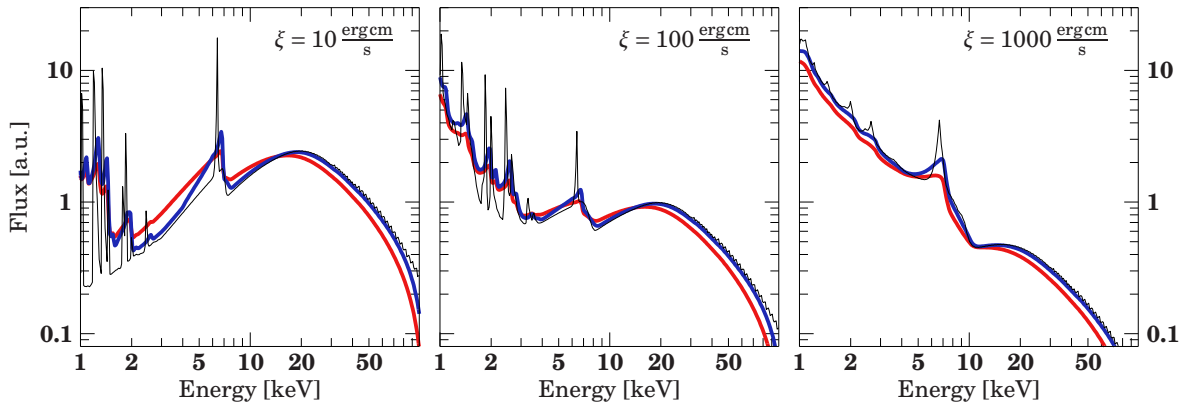


Fig. 4.2: *The reflionx-model (black) for $\xi = 10 \text{ erg cm/s}$ (left), $\xi = 100 \text{ erg cm/s}$ (middle), and $\xi = 1000 \text{ erg cm/s}$ (right) convolved for different ionizations ξ . The convolution of the reflected spectrum with the *relconv-model* is shown for spin $a = 0.998$ (red) and $a = -0.998$ (blue). A typical emissivity $\alpha = 3$ and inclination angle $\theta_o = 40^\circ$ are assumed.*

tough to calculate, as due to the focused emission from the inner parts and the strong redshift in this region each small ring of the accretion disk contributes at a different energy. The tiny steps that can be seen in the profiles, especially for low inclinations, originate from the fact that the accretion disk is made out of a finite amount of rings and therefore appear only in a highly resolved grid. This explanation can be justified in Fig. 4.1b, as in this case all parameters are the same, except that the spin of the black hole is now maximally negative. The resulting lines are narrower, which leads to profiles without any visible wiggles. Moreover, it can be nicely seen in the figure that by changing the inclination the overall line shape and not only the position of the peaks can be totally changed. In Fig. 4.1c the model is shown for the whole range of possible spins of the black hole. Again the shape is smooth and broadens as expected with increasing spin. Note that the sharp edges at the blue peak of the line are really expected (see Fig. 3.6). The effect of a changing emissivity law is illustrated in Fig. 4.1d, for maximal negative spin and an inclination of $\theta_o = 40^\circ$. It should demonstrate that the algorithm has no problems in describing the sharp peaks present for low emissivities. Additionally one can see how the line changes from a clearly double peaked structure to a very broad, asymmetric shape, only by changing the emissivity of the accretion disk.

4.2 USAGE IN DATA ANALYSIS

The model function *relline* explained above can be added to data analysis software such as ISIS (Houck & Denicola, 2000) or XSPEC (Arnaud, 1996). It can be downloaded from <http://www.sternwarte.uni-erlangen.de/research/relline/>. News such as bug fixes and recent developments can also be found there. In order to compile the model successfully, at least the XSPEC version 12.6e needs to be installed. This is mandatory, as the model is written in Fortran 90, which has only recently been supported by XSPEC. One specialty of the model is that the radius can be given in two units. For all radial parameters, negative and positive values are possible. Whereas a positive radius means it is given in units of r_g , a negative sign means the radius is in units of r_{ms} . In order to switch from one to the other parametrization, the hard limits have to be changed accordingly such that either all values are positive or negative. Otherwise the fitting algorithm might not work properly. Especially the radius in r_{ms} is useful

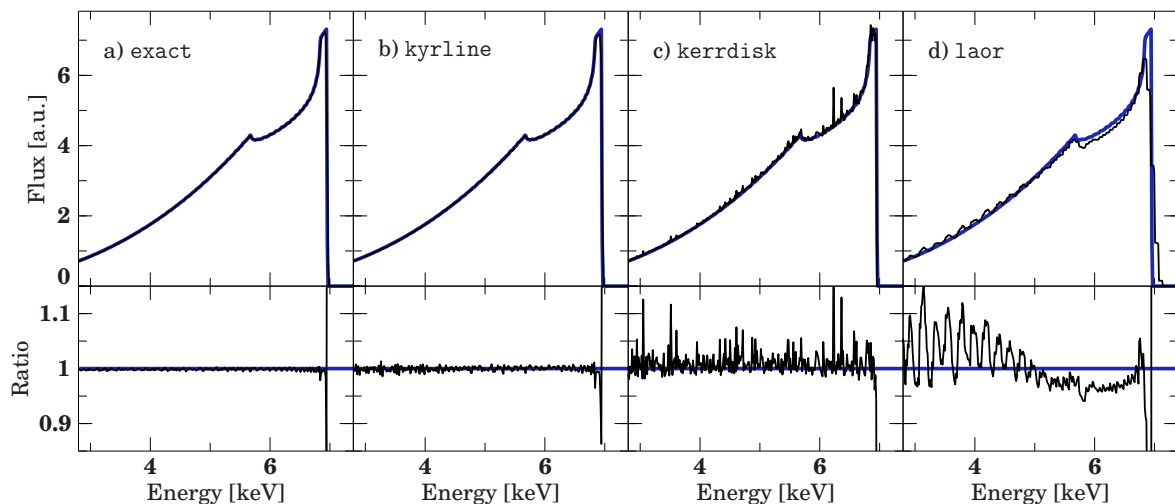


Fig. 4.3: Comparison of the *relline* model (blue) with (a) the exact line profile, (b) *kyrline*, (c) *kerrdisk*, and (d) the *laor* model for an emission line at $E = 6.4$ keV around a black hole with $a = +0.998$, an inclination angle of $\theta_0 = 40^\circ$, an emissivity r^{-3} , and an outer radius of $50 r_g$.

for fitting, as e.g. it restricts the inner radius of the accretion disk always to be at the ISCO when freezing $r_{\text{in}} = -1$, regardless if the spin parameter changes.

Additionally to the *relline* model, an implementation as a convolution model called *relconv* is provided. It is used for calculating the relativistic smearing of continuum components. This means it can be used together with models like *relionx* (Ross et al., 1999; Ross & Fabian, 2005), which predict the emitted spectrum from the accretion disk, including several elements and ionization stages.

Figure 4.2 shows the effect of the convolution for different ionizations of the accretion disk. The ionization parameter ξ parametrizes the disk from quasi-neutral ($\xi \approx 1$) to fully ionized ($\xi \approx 10^5$). The plot illustrates nicely that the general relativistic effects induce a blurring of the sharp emission lines. Moreover it shows that the spin of a black hole not only affects the peaks of the line, but also part of the continuum shape. For higher ionizations the peaks in the reflected spectrum get broader and therefore the relativistically convolved spectrum even more blurred.

Currently *relline* is already used by several astronomers. For example Egron et al. (2011) fitted the broad line of the neutron star MXB 1728–34. In this work it is used for $a = 0$, together with other line models. Moreover Duro et al. (in prep.) are analyzing the relativistic emission feature in Cygnus X-1 at the moment. In Sec. 6.1 it is shown how *relconv* together with *relionx* enables us to constrain the the spin by analyzing a simultaneous *XMM-Newton* and *RXTE* observation.

4.3 COMPARISON TO OTHER MODELS

Figure 4.3 shows a comparison of the *relline* model to other models for relativistic lines commonly used in X-ray astronomy. A comparison of the model with an exact numerical evaluation of Eq. 3.14 that does not make use of precalculated quantities and interpolation shows that there is no significant deviation between both approaches (Fig. 4.3a). In addition, for

$a \geq 0$ the produced shape is very similar to the *kyrline* model, which uses a table a factor 10 times larger and a Gaussian emission profile instead of a delta function (Fig. 4.3b). This result shows that for $a \geq 0$ and when it is sufficient to use the limb-darkening law of Laor (1991) or the limb-brightening law of Haardt (1993), both models can be used with confidence. Moreover, the *relline* model was compared to a non-public code from the *ky*-family, which allowed to plot line profiles for negatively spinning black holes. For all available and reasonable parameter space both models were in perfect agreement (Dovčiak, priv. comm.).

For completeness, Fig. 4.3c and Fig. 4.3d compare the exact profile to the *kerrdisk* and the *laor* model. As already explained above, the spikes in the former model are due to divergences in the integration of the transfer function. We note, however, that if the line is evaluated on an energy grid appropriate for a Silicon detector, these spikes will be averaged out and therefore have no effect on any of the published results. The *laor* model, on the other hand, shows strong deviations from the correct line shape, which are caused by the very coarse energy grid. Especially in the tail of the line these deviations are large enough that they could bias model fitting. For this reason, we caution against using this model in data analysis work.

CHAPTER 5

THE LAMP-POST GEOMETRY

The formalism for tracing photons in the vicinity of rotating black holes was extensively investigated in the previous chapters. We are able to trace the photons from the disk to the observer, even in the case of negatively spinning black holes. Simulating the shape of broad emission features, we have to assume an emissivity profile of the disk. The canonical value for a standard Shakura & Sunyaev (1973) disk is

$$I(r) \propto \frac{1}{r^3} \left(1 - \sqrt{\frac{r_{\text{in}}}{r}} \right) \quad , \quad (5.1)$$

which means that in the outer parts the emissivity is proportional to r^{-3} and gradually flattens towards the inner edge of the disk (r_{in}). In many observations (e.g., MCG–6-30-15, Wilms et al., 2001), the emissivity profile is observed to be extremely steep at the inner radii of the disk. Hence, a better model of the accretion disk emissivity itself or a different geometrical setup of the system is necessary to explain the prevailing physics properly. In addition to the spectral analysis, also variability studies of the broad iron lines pose a problem for standard models assuming a corona above the disk. In these studies, the time variability of the continuum flux, i.e., the primary hard X-ray radiation, is compared to the flux in the lines, which are produced by the reflected radiation. Hence, the connection between the primary and the reflected radiation is probed in this way. Measurements in sources such as MCG–6-30-15 (Martocchia et al., 2002a) and NGC 3516 (Iwasawa et al., 2004) show an anti-correlation in flux between the primary hard X-rays and the reflection in the lines. In contrast to that, one would expect the opposite behavior in the case of a corona illuminating the disk: A more luminous primary source produces more photons that irradiate the accretion disk and therefore induce a stronger reflection component (Martocchia & Matt, 1996). Martocchia et al. (2002a), Miniutti et al. (2003), and Vaughan & Fabian (2004) use the strong light bending in the “lamp-post” geometry to explain the observed anti-correlation in MCG–6-30-15. In this model, first mentioned by Martocchia & Matt (1996), the hard radiation is assumed to be emitted from a source on the rotational axis at height h above the black hole. For a schematic overview see Fig. 5.1. The anti-correlation between the continuum and the reflection component is explained in this model by the strong light bending: For a primary source very close to the black hole, most of the photons are focused on the accretion disk, producing a strong reflection component. Therefore less photons are left over to contribute to the continuum component, which is directly emitted towards the observer (Miniutti & Fabian, 2004). For an increasing height of the hard X-ray source the effect gets weaker and therefore more photons can escape, which strengthens the continuum radiation, but weakens the reflected flux (Miniutti, 2006).

In the following we will use the numerical methods developed in the previous chapters

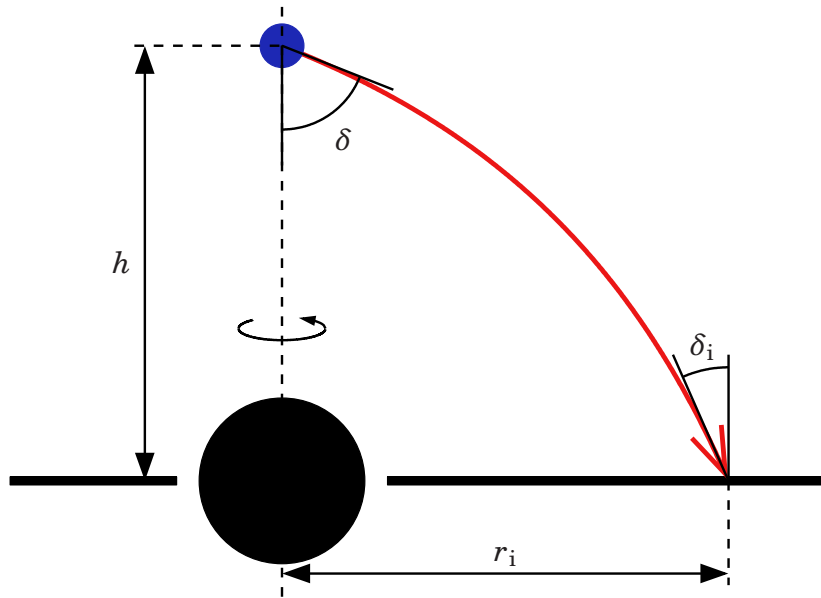


Fig. 5.1: Plot of the jet-base geometry, showing a photon track (red) emerging from the primary source (blue) at height h above the black hole. The photon hits the disk at distance r_i from the black hole under an angle of δ_i . Note that δ_i is measured in the rest frame of the accretion disk.

to investigate the irradiation of the accretion disk in the “lamp-post” geometry. As a good physical explanation of this hard X-ray source on the rotational axis is the base of a jet (Markoff & Nowak, 2004), we will also call this the “jet-base” geometry. This interpretation is encouraged by the fact that direct and reprocessed emission from such a jet base is equally capable in describing the observed X-ray broad-band spectrum as a corona above the accretion disk (Markoff et al., 2005). Moreover this geometry would allow to explain the correlation between observed radio and X-ray flares of Microquasars such as GX 339-4 (Corbel et al., 2000) or Cyg X-1 (Wilms et al., 2007). Additionally, Maitra et al. (2009) used this setup to successfully described the broadband spectrum (from radio throughout X-ray) of XTE J1118+480 and GX 339-4.

Relativistic photon trajectories in the lamp-post geometry have first been investigated by Martocchia & Matt (1996) in order to explain a very large equivalent width of the iron $K\alpha$ line in some sources. A more detailed discussion of effects in this geometry is presented by Martocchia et al. (2000), which includes overall spectra and dependencies on the spin. In his PhD thesis, Dovčiak (2004) further investigated this setup and included it in the XSPEC model KYLCR for fitting observational data (Dovčiak et al., 2004). As they cannot be found in the above mentioned references, the important equations and properties are derived in detail in the following section.

5.1 THE EQUATION OF MOTION

5.1.1 BASIC EQUATIONS

For all calculations presented in the following, we make use of the general equations derived in Sec. 2.2.2. In order to simplify the equations, all units containing a length scale are given in units of the gravitational radius r_g . Remembering that the equation of motion (Eq. 2.31) only has solutions for $V_\theta \geq 0$ and using the fact that each photon emitted by this source has to start

at the rotational axis ($\theta = 0$), leads to the constraint

$$V_\theta|_{\theta=0} = -\lambda^2 \stackrel{!}{\geq} 0 \implies \lambda = 0 \quad . \quad (5.2)$$

This means that we only have to consider photon trajectories with zero angular momentum. Hence the difference in the photon trajectories are determined by the remaining parameter q . Using similar considerations as in Sec. 3.1.1, we can calculate the emission angle δ (as defined in Fig. 5.1) corresponding to a certain q -parameter for an emission at height h by

$$\sin \delta = \frac{|p_{h,\parallel}|}{|p_h|} = \frac{(p_h)_\mu (n_h^{(\theta)})^\mu}{(p_h)_\nu (u_h)^\nu} = \frac{[\sqrt{V_\theta/\Sigma}]_{\theta=0}}{-u_h^t} = \frac{\sqrt{h^2 - 2h + a^2}}{h^2 + a^2} \sqrt{q^2 + a^2} \quad , \quad (5.3)$$

where $(n_h^{(\theta)})^\mu$ is the normal vector in θ -direction. In the above equation we used that

$$u_h^t = \sqrt{\frac{h^2 + a^2}{\Delta(h)}} \quad (5.4)$$

is the only non-zero component of the four-velocity here. Its value can be easily derived by using the normalization criterion

$$-1 \stackrel{!}{=} u_\mu u^\mu = (u_h^t)^2 g_{tt}(h) = -(u_h^t)^2 \frac{\Delta(h)}{h^2 + a^2} \quad . \quad (5.5)$$

As argued in Sec. 5.2, we are only interested in trajectories for which $q^2 > 0$. From Eq. 5.3, we can deduce that this condition means that all trajectories which fulfill

$$\sin \delta \geq \frac{|a|}{\sqrt{h^2 + a^2}} \sqrt{1 - \frac{2h}{h^2 + a^2}} \quad , \quad (5.6)$$

are reasonable solutions. Examining the last part of the square root closer leads to the fact the above condition is only defined for $h \geq 1 + \sqrt{1 - a^2}$. But this is just the requirement that $h \geq r_+$, i.e., the primary source has to be outside of the black holes event horizon. This condition is readily fulfilled for any astrophysical source of radiation.

The q -parameter for an arbitrary δ can be easily derived from Eq. 5.3 to be

$$q = \sqrt{\frac{\sin^2 \delta (h^2 - 2h + a^2)}{h^2 + a^2}} \quad (5.7)$$

A map of the q -parameter for combinations of the height of the primary source and the emission angle can be seen in Fig. 5.2. The black regions are combinations of (h, δ_i) , which do not have a solution, as Eq. 5.6 is not fulfilled. For $a = 0$ the q -parameter always satisfies Eq. 5.6, but with increasing spin the “forbidden region” is growing. For our purpose this region is not interesting, as these photons will never hit the accretion disk. Note that we only have to consider $a \geq 0$, as long as the system only consist of the black hole and the primary source. The meaning of a negative spin is not given until we consider parameters connected to the accretion disk, which would have to be counterrotating with respect to the black hole in this case.

The two extreme cases of a non-rotating BH (Fig. 5.2, left panel) and a maximally rotating BH (Fig. 5.2, middle panel) show a very similar behavior in q . In both cases q increases almost identically with both, emission angle δ and height h . The ratio (Fig. 5.2, right panel) proves this point, as the q -parameter differs only very close to the forbidden region. As even photon

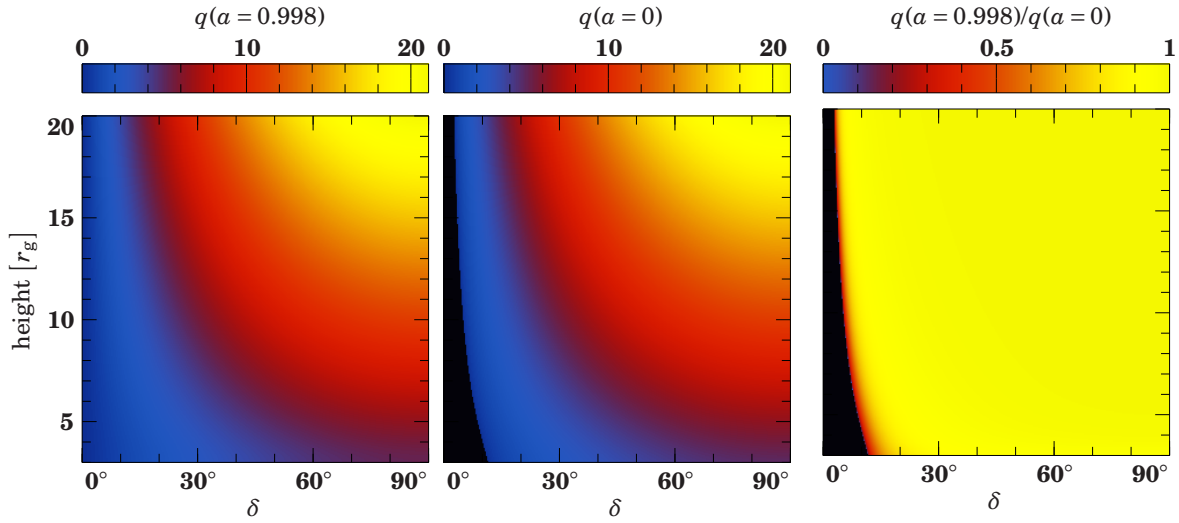


Fig. 5.2: The left and the middle panel show a 2d-map of the q -parameter for different combinations of (h, δ_i) for a non rotating black hole (left) and a maximally spinning black hole (middle). The panel to the right displays the ratio between the q -parameter for $a = 0.998$ and $a = 0$. The black areas in the plots mark the combinations of (h, δ_i) , which do not have a reasonable solution for q .

trajectories with q -parameters close to this region won't hit the accretion disk, these differences do only play a very minor role when considering the incident radiation on the accretion disk.

Assuming we already have solved the equation of motion and know the radius at which the photon hits the disk, we can derive more physically interesting parameters. One important quantity is the energy shift g_i the photon exhibits during its way. As the initial four-momentum together with the corresponding four-momentum on the accretion disk are known, the energy shift can be readily written down in analogy to Eq. 3.7:

$$g_i = \frac{E_d (p_d)_\mu u_d^\mu}{E_h (p_h)_\nu u_h^\nu} = \frac{u_d^t}{u_h^t} = \frac{(r_i \sqrt{r_i} + a) \sqrt{h^2 - 2h + a^2}}{\sqrt{r_i} \sqrt{r_i^2 - 3r_i + 2a \sqrt{r_i} \sqrt{h^2 + a^2}}} . \quad (5.8)$$

The second quantity of physical importance is the incident angle δ_i of the photon when it hits the accretion disk at radius r_i .

$$\cos \delta_i = \frac{p_\perp}{|p|} = \frac{(p_d)_\mu (n_d^{(\theta)})^\mu}{(p_d)_\nu (u_d)^\nu} \Big|_{\theta=\pi/2} = \frac{q}{r_i u_d^t(r_i, a)} \quad (5.9)$$

The incident angle is important for accretion disk models, as it determines which depth of a photon can reach. By assuming the same optical depth for all δ_i , the photon travels the same path in the disk, but clearly reaches different depths depending on the incident angle. Hence, regions with different incident angles might exhibit a different ionization structure, which has an impact on the reflected spectrum.

5.1.2 NUMERICAL METHODS

The value of q corresponding to a specific emission angle δ obtained by Eq. 5.9. Hence we can solve the equation of motion for a photon emitted under this angle from the primary source

$(h, 0)$ to any point (r, θ) . The equation of motion for this case then reads

$$\underbrace{\int_h^r \frac{dr'}{\sqrt{V_{r'}}}}_{\mathcal{I}_h^r} = \underbrace{\int_0^\theta \frac{d\theta'}{\sqrt{V_{\theta'}}}}_{\mathcal{I}_0^\theta} . \quad (5.10)$$

This equation is similar to the equation for trajectories from the accretion disk to the observer (Eq. 2.31), but the limits are different. Moreover, V_r and V_θ are now fully determined as we know both λ and q . This means in practice that by specifying θ , we can calculate the corresponding distance r , which has to be done numerically, since the equation of motion has no analytic solution. In detail the upper limit of the radial integration r is iteratively changed, until the two integrals are equal within a certain precision.

In order to calculate the integrals \mathcal{I}_h^r and \mathcal{I}_0^θ , I modified the routines INTGVR and INTGVT of the code provided by Speith et al. (1995, see also Chap. 3). The routine INTGVT calculates the integral $\mathcal{I}_{\pi/2}^\theta$. Thus the integral corresponding to any arbitrary angle θ is simply

$$\mathcal{I}_0^\theta = \mathcal{I}_{\pi/2}^\theta - \mathcal{I}_{\pi/2}^0 . \quad (5.11)$$

Moreover no turning points in the θ direction are present, as photons, which initially fly towards the disk, will not exhibit a turning point before crossing the equatorial plane and thus before hitting the accretion disk.

INTGVR is used to integrate the radial part of the equation of motion. Instead of calculating a trajectory to an observer at infinity like in Chap. 3, we now start at the primary source above the black hole. Following Speith et al. (1995), I transformed the integral to an integration over $R^2 = \pm(1/r - 1/r')$, where the upper sign is chosen for $r < h$ and the lower sign for $r > h$, respectively. In the case of $r < h$ this leads to

$$\mathcal{I}_h^r = \int_0^{\sqrt{\frac{1}{r} - \frac{1}{h}}} \frac{2R dR}{\sqrt{V_r(R)}} . \quad (5.12)$$

The additional integral when a turning point in r -direction occurs, is automatically calculated correctly by INTGVR, as this integration is the same, regardless of the geometry (see Speith et al., 1995, for details). Note that for emission angles $\delta > \pi/2$ the sign in front of the radial integration changes, as this implies that the photon initially moves away from the black hole.

5.2 PHOTON TRAJECTORIES

In this section we focus on the path the photon takes in curved spacetime. Therefore we use the above described routines to solve the equation of motion (Eq. 5.10), where the integral in θ -direction is determined with the function INTGVT according to Eq. 5.11 and the integral in r -direction with INTGVR (Eq. 5.12), respectively.

Figure 5.3 shows the photon trajectories for different heights of the primary source. As expected, it is clearly visible in both panels that the closer the photons get to the black hole, the more curved the trajectory is. Therefore the photons emitted from the primary source closer to the black hole are focused more strongly onto the accretion disk like already mentioned by Martocchia & Matt (1996). At height $h = 2.5r_g$, even photons that are emitted parallel

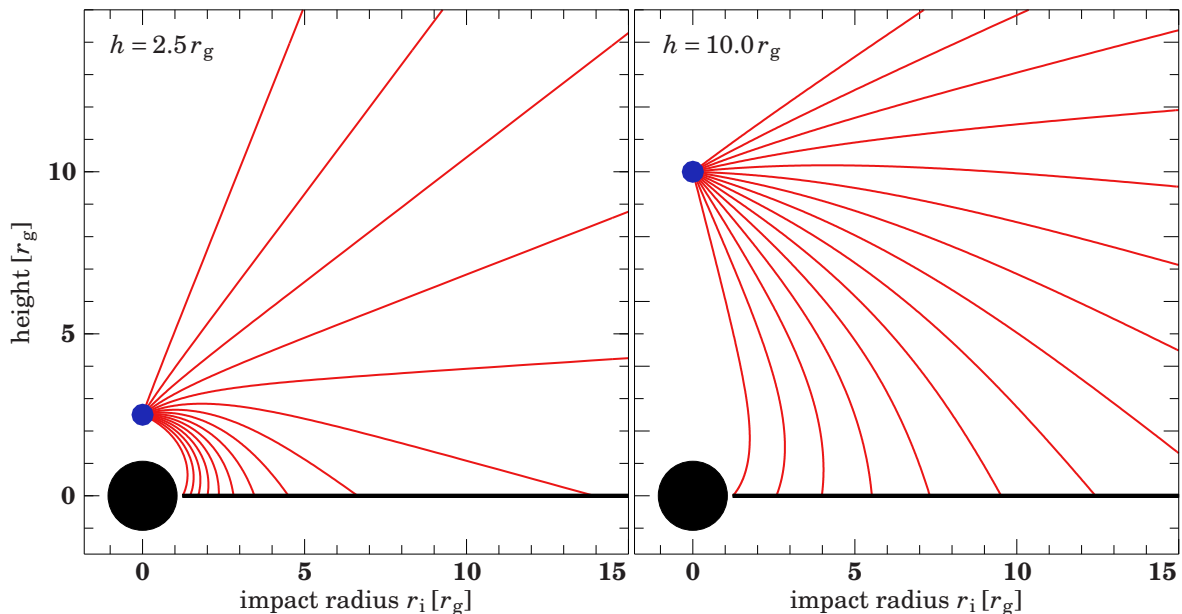


Fig. 5.3: The photon tracks (red) for photons emitted from the primary source (blue), which hit the accretion disk. The black hole, spinning with $a = 0.998$, is to scale.

to the accretion disk hit it closer than $5r_g$, i.e. still in the regime of extreme gravity. This configuration gives evidence to the observed anti-correlation in flux between continuum and line emission (see above): As most of the photons are focused onto the disk, the reflected flux is enhanced at costs of the continuum flux. On the contrary, this implies for a black hole with maximal negative spin that most of the emitted photons from such a primary source will not hit any part of the accretion disk, as the inner radius of its surrounding disk is larger than $9r_g$ (see Eq. 2.29). These photons are either caught by the black hole or contribute to the continuum radiation on the other side of the accretion disk. As the current model (Miniutti, 2006) does only account for a maximally rotating black hole, further analysis has to be done in order to estimate the importance of a different spin for the timing analysis. Nevertheless we can see from the above results that the inner radius, and therefore the black hole’s spin, should play a role when measuring and interpreting the fraction of reflected radiation.

The amount of reflected radiation is indeed crucial, as, e.g., the different reflection fractions can be attributed to certain processes like “Synchrotron dominated” or “Synchrotron-Self-Comptonization dominated” in jet models (Markoff & Nowak, 2004; Markoff et al., 2005). Note that although Sec. 3.4 explicitly presented the effects of a changing spin, it is also shown that apart from a larger inner radius of the accretion disk the changes are small. Therefore we would not expect that the photon trajectories change dramatically with spin, but only the inner edge of the accretion disk. This argumentation is strengthened by Fig. 5.2, which shows that the difference in the q -parameter, which totally characterizes a certain trajectory in the case of a lamp-post model, is small.

Moreover it should be noted that the coordinates in Fig. 5.3 are given in the Boyer-Lindquist coordinate system. As explained in Chap. 2, the observer is in a locally non-rotating frame and thus rotates with the black hole. The angle θ and the distance to the black hole r are used in this coordinate system to parametrize the basis vectors. Because of the complexity of space-time, the Cartesian coordinates of the photons at each point of the trajectory cannot be derived

from simple geometrical considerations, but are related to the Boyer-Lindquist coordinates by an elliptical transformation (see Eq. 2.2). Hence, for a large distance to the black hole ($r \gg a$) we recover our geometrical relationship from flat space, but close to the black hole there are differences. These differences also vanish for a slowly rotating black hole, which can be easily seen in Eq. 2.2 for $a \rightarrow 0$.

5.3 DISK ILLUMINATION

Having described the whole photon trajectory in the previous section, we will now focus on the point where the photon actually hits the accretion disk. The radial dependence of the irradiated intensity provides a crucial information for modeling the local physics of the disk. This intensity can be calculated by using the same numerical methods as described in Sec. 5.1.2. Therefore we simulate for equally spaced intervals of emission angles δ , i.e., for isotropic emission, the corresponding impact radii $r_i(\delta)$. As the intensity is directly proportional to the density of incoming photons, we can use the spacing between the impact points to derive

$$I_{\text{kerr}} \propto \frac{1}{r_i(\delta_{i+1}) - r_i(\delta_i)} \quad , \quad (5.13)$$

where δ_i is the i -th emission angle of the equidistant interval.

5.3.1 COMPARISON TO FLAT SPACE

In order to better understand the differences of the fully relativistic approach, we will first compare the simulated intensity to the same geometry, but assume flat space. For this case the intensity can be calculated analytically. If we concentrate on one photon emitted under δ at height h , we can express the impact point r_i by using the delta function $\delta(r_i/h - \tan \delta')$. This allows us to integrate over all angles and calculate the intensity on the disk for a certain r_i :

$$\begin{aligned} I_{\text{flat}}(r_i, h) &= \int_0^{2\pi} \delta[r_i/h - \tan \delta'] d\delta' \\ &= \int_0^{2\pi} \cos^2(\delta') \cdot \delta[\arctan(r_i/h) - \delta'] d\delta' \\ &= \frac{1}{1 + (r_i/h)^2} \end{aligned} \quad (5.14)$$

Before being able compare this to the simulated intensity, the normalization has to be done correctly. This is very crucial, as due to light bending, there might be more photons hitting the disk in curved spacetime than in flat space, although the primary source emits the same amount of photons. This can be easily understood, as the emission angles between the curved and the flat space for photons which ought to hit the same disk, are certainly different (see curved tracks in Fig. 5.3). Therefore the condition for a equally bright primary source translates to

$$\frac{1}{\Delta\delta_{\text{kerr}}} \int_{r_{\text{in}}}^{r_{\text{out}}} I_{\text{kerr}} dr \stackrel{!}{=} \frac{1}{\Delta\delta_{\text{flat}}} \int_{r_{\text{in}}}^{r_{\text{out}}} I_{\text{flat}} dr \quad , \quad (5.15)$$

where $\Delta\delta$ is the difference between the maximal and minimal emission angle corresponding to the outer and inner edge of the accretion disk.

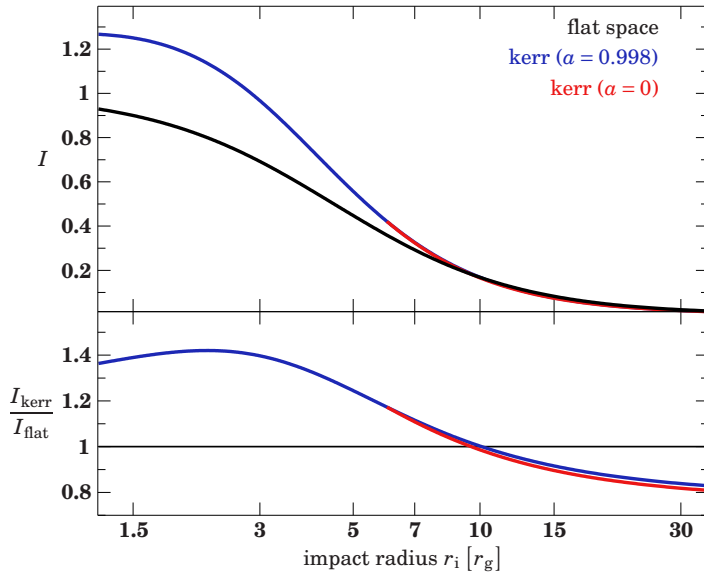


Fig. 5.4: Evolution of $I(r)$ in the different geometries for a height $h = 4.5r_g$ of the primary source above the black hole. It is visible that a different spin has almost no effect, except that the inner radius of the accretion disk must be at a larger radius for a non-rotating black hole.

The evolution of the intensities with r can be seen in Fig. 5.4. As already supposed from the almost constant q -parameter for different spin (Fig. 5.2), the intensity on the accretion disk does almost not depend on the spin of the black hole at all, although a primary source very close to the black hole ($h = 4.5r_g$) was used in the simulation. Clearly the inner radius of the accretion disk is much larger in the non-rotating case and therefore the expected total intensity irradiating the disk mainly depends on the inner radius of the disk. The ratio between the flat and the relativistic intensity can be seen in the lower panel of Fig. 5.4. Here it becomes obvious that a much larger fraction of the intensity irradiates the innermost parts of the disk. This is indeed interesting, as here most of the relativistic effects take place and hence this is where the shape of the spacetime is imprinted in the photon spectrum. Thus a higher intensity of photons irradiating these regions means that we obtain more information of the curved spacetime in the measured spectrum, as a larger fraction of the measured photons exhibits strong relativistic effects.

The two-dimensional map in Fig. 5.5 shows how the ratio $I_{\text{kerr}}/I_{\text{flat}}$ changes with height of the primary source. As the spin of the black hole has no large effect (see Figs. 5.2 and 5.4) apart from changing the radius of marginal stability, it was chosen to be maximal. Although the ratio quickly converges towards unity for an increasing height, it is remarkable that there is still an enhanced irradiation of the disk of roughly 10% at $h = 20$ visible in the $2d$ -map of Fig. 5.5. This rapid decrease would be indeed an interesting result, as the different geometries are mainly distinguished by the radial behavior of the emitted intensity and not by different normalizations. Hence, the shape of a fluorescent emission line should be sensitive for primary sources at low heights. In the case of MCG-6-30-15 this criterion would be fulfilled, as measurements suggest a height of $3-12r_g$ for the hard X-ray source (Martocchia et al., 2002a; Miniutti et al., 2003).

One way of getting closer to a simple description of the processes in the strong gravity regime, is trying to approximate the evolution of parameters in curved space by functions holding true in flat space. For large distances from the black hole, where space is almost flat, the former relativistic behavior has to converge towards the one of flat space. In the following

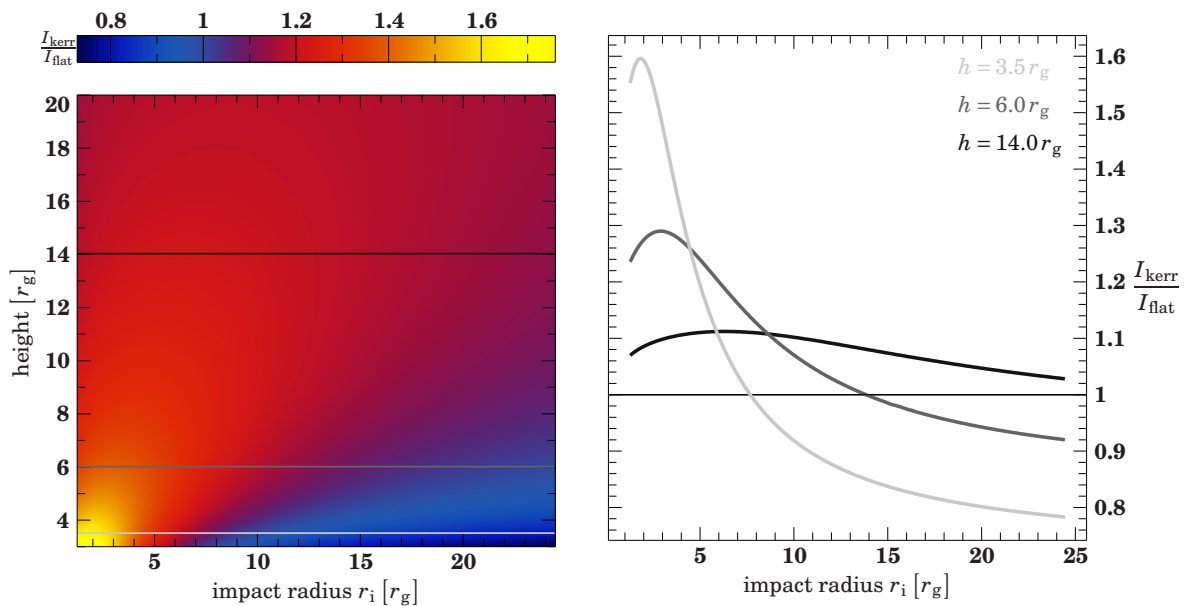


Fig. 5.5: Ratio of the intensity, I_{kerr} , for a spacetime around a maximally rotating black holes to the expected intensity in flat spacetime I_{flat} . Hence the plotted quantity is the same as in Fig. 5.4, but for a continuum of heights. The border between the red and the blue regions roughly marks the different areas where the intensity is enhanced by the Kerr metric and where it is reduced. In the right panel, the ratio for a height of $h = 3.5 r_g$, $h = 6 r_g$ and $h = 14 r_g$ of the primary source is plotted in detail.

we will try to approximate I_{kerr} (see Fig. 5.4) by the formula

$$I(r_i) = N \cdot \frac{1}{1 + (r_i/h)^\gamma}, \quad (5.16)$$

where we recover the evolution of the incident intensity in flat space from Eq. 5.14 for a normalization $N = 1$ and $\gamma = 2$. Now we use the simulated values of I_{kerr} and try to fit $I(r_i)$ of the above formula to $I_{\text{kerr}}(r_i)$. In order to do a proper χ^2 analysis, the uncertainty of the data points was (arbitrarily) defined to be $0.01\sqrt{I}$ and thus 1% of the Poisson noise. This means that the absolute value of χ_{red}^2 is not a useful quantity, but it is nevertheless a measure for the goodness of the fit. The main results can be seen in Fig. 5.6. By looking at the χ_{red}^2 -panel, one can clearly see that the fit improves a lot for growing height and thus a flatter space. This result proves the above statement that we recover the flat space behavior for large distances from the black hole. Moreover in the case of a low primary source, the best fit solution for a non-rotating black hole ($\gamma = 2.3$) is closer to flat space than for a maximally rotating one ($\gamma = 2.7$). The most important result of Fig. 5.6 is that the overall behavior of curved spacetime can be approximated by a larger γ , i.e. a steeper emissivity and hence more photons that are focused on the inner, highly relativistic regions of the accretion disk. Additionally, the deviations are strongest for low heights. Transformed to a measured spectrum, i.e., the shape of a broad emission line, this result implies that the asymmetry of the line profile should be a measure of the height of the primary source. The flux variability observations of MCG-6-30-15 indeed connect the very asymmetric line shape to a primary source of low height (Martocchia et al., 2002a; Miniutti et al., 2003; Vaughan & Fabian, 2004).

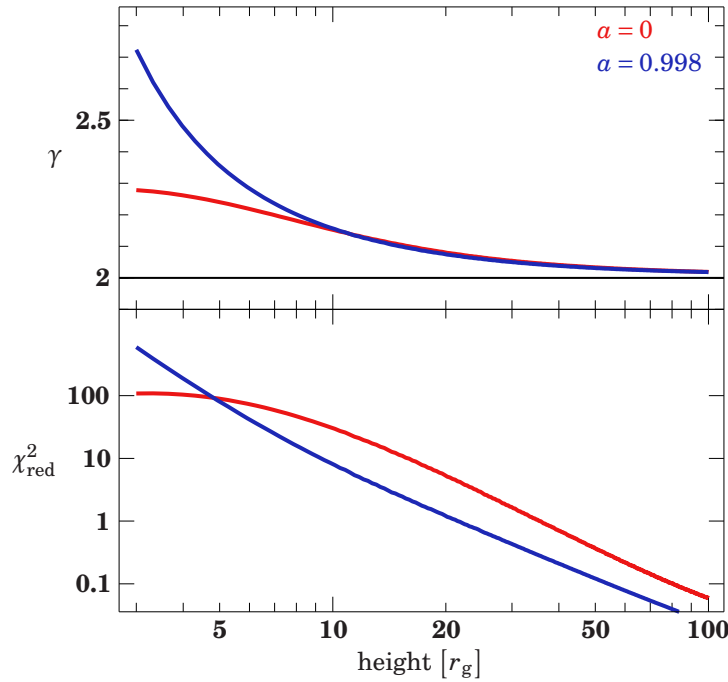


Fig. 5.6: The parameters of fits of the simulated intensity to the function $I = [1 + (r/h)^\alpha]^{-1}$. It is visible that for larger h , γ converges towards its value in flat space ($\gamma = 2$) and $I_{\text{kerr}} \rightarrow I_{\text{flat}}$, as χ_{red}^2 decreases.

5.3.2 THE ENERGY SHIFT

Due to the effects of strong gravity, the energies of the emitted spectrum will be shifted depending on the photon's trajectory. Thus we would expect the incident spectrum to change for different radii r_i . As an incident photon can only contribute to fluorescent emission if it has an energy above the ionization energy of a certain element, a change in spectral shape also implies a change in the amount of fluorescent emission. Hence, the strength of the fluorescent emission line depends on the incident spectrum of the accretion disk.

Figure 5.7 shows the energy shifts $g = E_i/E$ of photons emitted at different heights, when they hit the disk at r_i . The color scheme indicates the direction of the energy shift: Blue means that the photons gains energy, whereas the red color implies that it loses energy. Most of the image is yellow, indicating that for most incident radii and heights there is only a minor energy shift. The most remarkable region is the narrow blue part at very low radii. Almost regardless of the height of the primary source, a photon hitting the disk at $r_i < 3r_g$ is shifted between three and eight times of its energy. A larger height slightly enhances this effect.

This extreme blue-shift of energies for low radii introduces a strong change of the incident spectrum with r . In the simplest case, this implies that at low radii the amount of energetic photons is larger than at higher radii. As the strength of a fluorescent emission line is proportional to the number of photons above the ionization edge, this blue-shift has direct consequences on the emissivity profile of the disk: An extreme blue-shift means that a larger number is above the edge and thus the fluorescent emission is enhanced for these regions, additionally to the geometrical effects discussed in Sec. 5.3.1. Thus the emitted spectrum at the primary source needs to be taken into account and shifted according to r_i and h . As the change of the spectrum due to such a large energy shift is certainly not negligible in all cases, this result shows that a fully relativistic treatment is necessary, although the intensity could be described fairly well by a larger γ -parameter, as determined in Sec. 5.3.1.

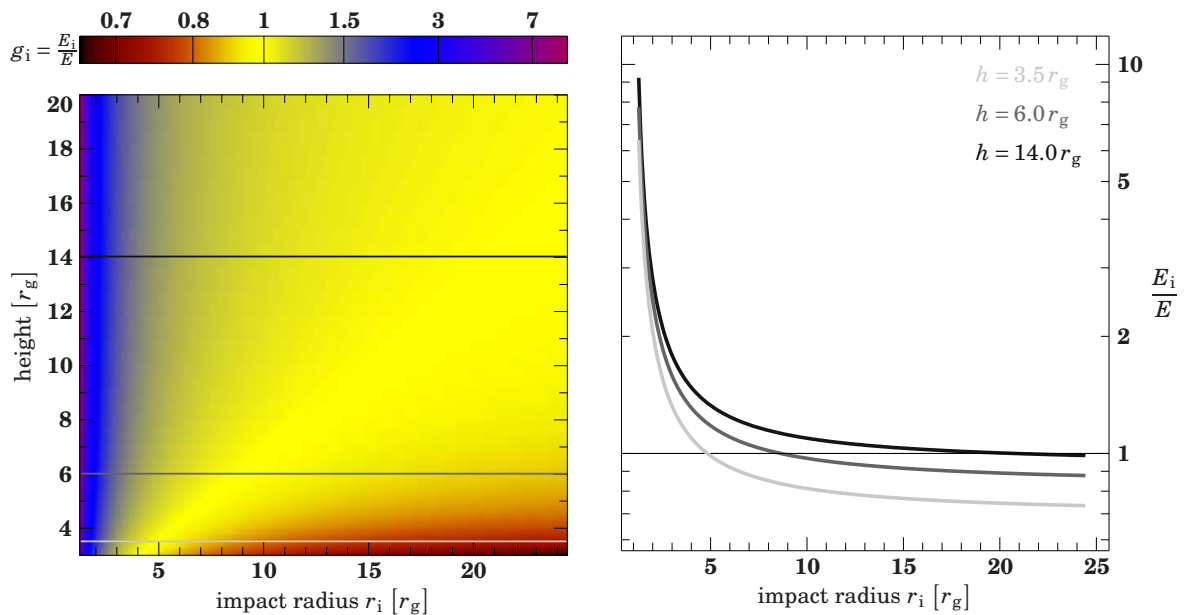


Fig. 5.7: The energy shift $g = E_i/E$ for photons, emitted at a certain height, when they hit the disk around a maximally spinning black hole ($a = 0.998$), indicated by the color scheme: Blue means that the photon has a higher energy when hitting the disk, whereas red implies a lower energy, respectively. On the right panel the detailed evolution for the heights $h = 3.5 r_g$, $h = 6 r_g$ and $h = 14 r_g$ can be seen. These cases are indicated in the 2d-plot by the same colors.

5.3.3 THE INCIDENT ANGLE

An additional quantity important for any realistic ionization model is the incident angle δ_i of the photon in the rest frame of the accretion disk (see Fig. 5.1 for the definition of δ_i). This is easily convincing in a simple geometrical picture: A photon hitting the disk perpendicular can reach much deeper layers of the accretion disk than a photon on an almost parallel trajectory to the disk, when assuming the same optical depth in both cases. Hence, we would expect that the reflected spectrum and therefore the line strength depend on the incident angle.

The incident angle for various combinations of heights and radii is plotted in Fig. 5.8. Note that this angle is measured in the rest frame of the accretion disk and therefore not equal to the tangent on the photon trajectory in Fig. 5.3 at the incident radius. Although for a stationary observer in Boyer-Lindquist coordinates¹, the photon hits the disk perpendicular (i.e. $\delta_i = 0$), the incident angle will always be greater zero in the rest frame of the disk due to the motion of the disk.² This introduces a “minimal incident angle” for a certain height, which can be seen in Fig. 5.8, marked by the white line in the 2d-plot. A more thorough look at trajectories close to this minimum reveals that it separates the trajectories which exhibited a turning point in r -direction (trajectories closer to the black hole) from the ones which do not. Following the blue part to larger heights, it can be seen that this minimal angle gets lower and eventually reaches zero for a primary source at an infinitely large distance from the compact object.

¹Note that a stationary observer means that (s)he is at a fixed point in (r, θ) -space, which implies that (s)he is rotating with an angular velocity according to Eq. 2.4 (see Sec. 2.1.2 for details).

²For illustration purposes this can be compared to a ball dropped onto a carousel from a point not on the rotational axis: An outside observer will see it hitting the floor perpendicular, whereas an observer sitting in the carousel will never measure the ball to hit the floor perpendicular (M. Böck & M. Hanke, priv. comm.).

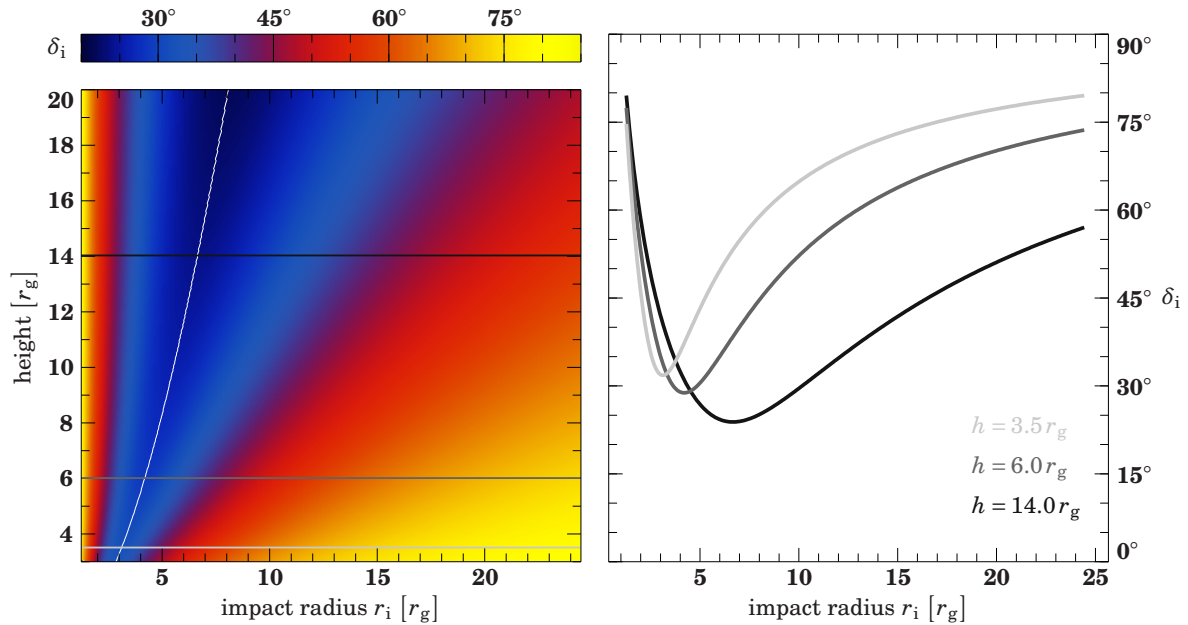


Fig. 5.8: The incident angle δ_i (see Fig. 5.1 for the definition) when the photon hits the accretion disk. Again the detailed evolution for the heights $h = 3.5 r_g$, $h = 6 r_g$ and $h = 14 r_g$ is displayed on the right panel and these cases are indicated in the 2d-plot by the same colors. The narrow white line in the left panel marks the minimal incident angle for each height.

The distribution of emission angles reveals that the majority of the emission angles is relatively large. It evolves from large values at the innermost few gravitational radii of the disk to a region of low values ($\delta_i < 45^\circ$), which grows in size with increasing height. For even larger radii r_i , δ_i increases again towards $\delta_i = 90^\circ$ for $r_i \rightarrow \infty$. This behavior is what one would expect in flat space and thus meets the requirement that the simulated parameter converges towards its value in flat space for large distances.

As shown in the previous Sec. 5.3.2, the innermost radii are the most important for line diagnostics. Therefore the fact that photons tend to hit this part of the accretion disk at high inclination angles, implies that the induced change to the ionization in these region influences the line profile most.

CHAPTER 6

CONCLUSIONS, ONGOING AND FUTURE WORK

6.1 THE BROAD EMISSION LINE IN CYGNUS X-1

The 17.4 ksec *XMM-Newton* observation (Obs-Id: 0202760301) of Cygnus X-1 on 20th and 21th of November 2004 belongs to the observations with the highest signal to noise ratio of a broad emission line obtained for a Galactic source. During the observation the source was caught in an intermediate state. See, e.g., Remillard & McClintock (2006) for more information on states of black hole binaries. In order to achieve such a high data quality in the region of the strong Fe reflection feature (4–8 keV), the EPIC-pn detector was operated in the “modified timing mode” (Kendziorra et al., 2004). For bright sources such as Cyg X-1, the limiting factor for a *XMM-Newton* observation is the telemetry limit. In order to stay below this limit, the MOS1 and MOS2 camera are turned off and only the counts in the region of interest are transmitted. As the modified timing mode is suited to analyze the iron region, which is around 4–8 keV in the spectrum, only counts above an energy threshold of 2.8 keV are transmitted. Due to calibration issues of the modified timing mode, only data from 4–9.5 keV were used for the analysis. As this narrow energy band does not allow to model the continuum well, we use two simultaneous *RXTE* observations with an exposure of 2.0 ksec (Obs-Id: 90104-01-02-01) and 1.0 ksec (Obs-Id: 90104-01-02-00), respectively. The PCA and the HEXTE instrument onboard the satellite cover an energy band from 4–40 keV and 20–120 keV, sufficient to constrain the parameters of the continuum well. We are investigating the above described data set and it will be published soon in form of a letter (Duro et al., in prep.). In the following, the current status of the analysis is presented.

We describe the overall continuum of the spectrum with an exponentially cut off power law (Sunyaev & Trümper, 1979) and the thermal emission of the accretion disk with the model `diskbb`, using a fixed inner temperature of 0.5 keV. Additionally a narrow emission line originating from neutral iron reported, e.g., by Hanke et al. (2009) and Torrejón et al. (2010) was taken into account. The reflection feature, which still cannot be described by the above components, was modeled with the `relionx-model` (Ross et al., 1999; Ross & Fabian, 2005) and convolved with `relconv-model` in order to account for the general relativistic effects (see Sec. 4.2). In order to compensate the apparent charge transfer inefficiency (CTI) over-correction in the *XMM-Newton* data, we had to apply a gainshift to the energy bins of the form $E = E_0/1.02$.

Table 6.1 shows the important parameters, which resulted from fitting the data with the above described model. For this fit we obtained a total $\chi^2/\text{d.o.f}$ of 297/260, corresponding to $\chi^2_{\text{red}} = 1.26$. Figure 6.1 shows the data and the best fit obtained with the above presented

..... cutoffpl	
Index Γ	$1.75^{+0.03}_{-0.02}$
E_{fold} [keV]	280^{+50}_{-30}
norm _{pl}	$1.59^{+0.09}_{-0.10}$
..... reflionx	
Abundance Fe/solar	$2.0^{+0.1}_{-0.3}$
Ionization ζ [erg cm/s]	550^{+60}_{-40}
norm _{refl}	$(5.0^{+0.9}_{-0.8}) \times 10^{-5}$
..... relconv	
Emissivity α	$4.1^{+0.5}_{-0.4}$
Spin a	$0.86^{+0.03}_{-0.04}$
Inclination θ_0 [deg]	44^{+3}_{-2}

Tab. 6.1: Simultaneous fits to EPIC-pn, PCA and HEXTE data sets with a model consisting of an exponentially cut off power law, disk black body emission and a relativistically convolved reflection. The total $\chi^2/\text{d.o.f}$ is 297/260, corresponding to $\chi^2_{\text{red}} = 1.26$.

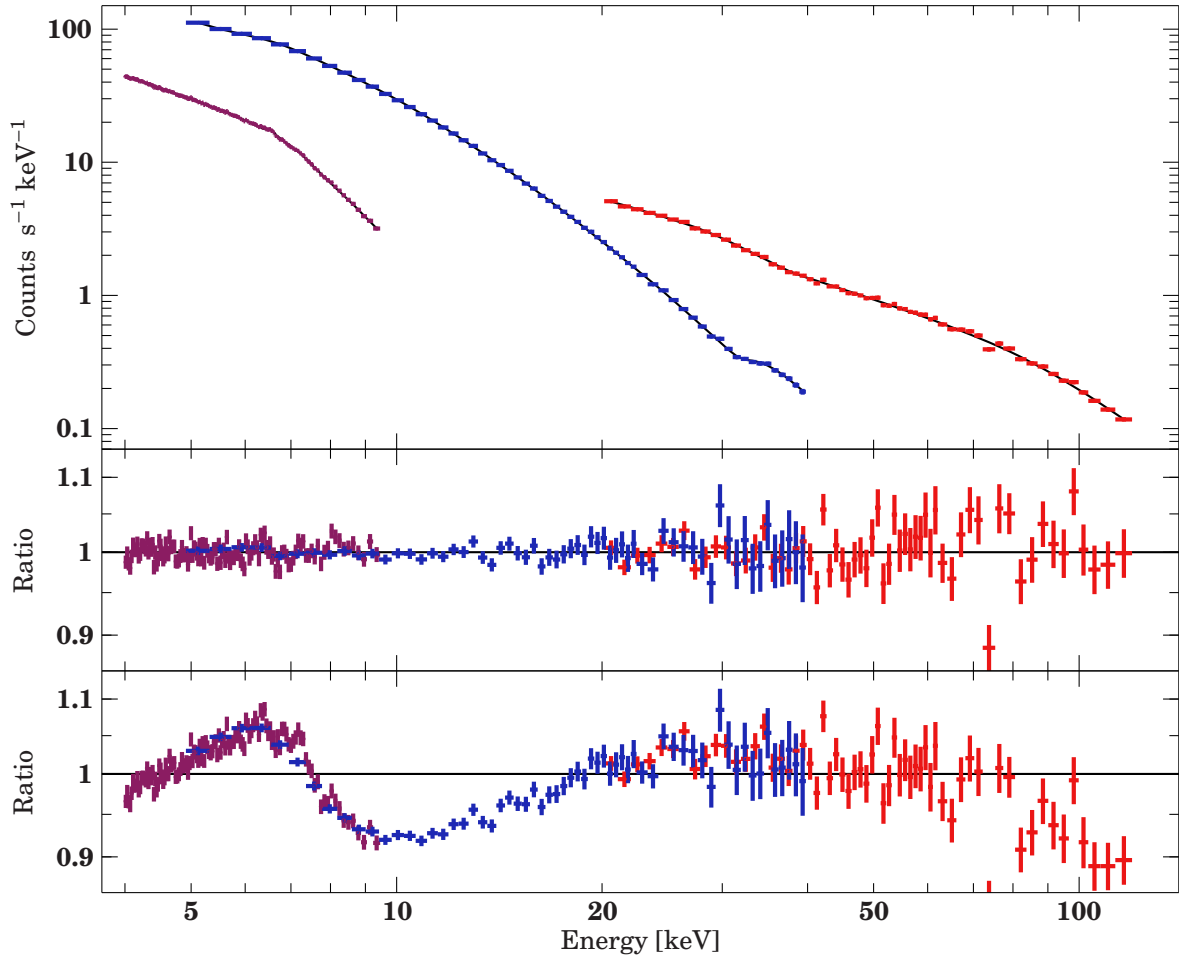


Fig. 6.1: Data of the simultaneous Cyg X-1 observation, consisting of data from the the EPIC-pn camera (purple), the PCA (blue), and the HEXTE (red). The data and the best fit model (black line) from Tab. 6.1 are shown in the upper panel. The middle panel shows the ratio between the model and the data. In order to illustrate the effect of the reflected component, the ratio between data and model is plotted without the reflection component in the lower panel.

model.

Based on the preliminary results shown above, first conclusions are presented in the following. First, the ionization parameter of $\xi = 550 \text{ erg cm/s}$ for the reflection points at a moderately ionized disk, which differs to the measurements by Miller et al. (2009) of $\xi \approx 10^4$. The emissivity index of $\alpha = 4.1_{-0.4}^{+0.5}$ is in agreement with the first analysis of this data set (Wilms et al., 2006). Moreover the inclination of $\theta_0 = 44_{-2}^{+3^\circ}$ of the accretion disk is consistent with the reported inclination between 32° and 50° of the orbit of the system (Ninkov et al., 1987). Note that there is no strong constraint that the accretion disk and the orbit of the system have to be aligned. Nevertheless, we would expect similar values, as these systems are expected to evolve towards the equilibrium state of aligned disk and orbit. The most interesting of the fit parameters is the spin of Cygnus X-1, which is found to be relatively high with $a = 0.86_{-0.04}^{+0.03}$. This result is in contrast to Miller et al. (2009), who measure a non-spinning black hole with the method of fitting the thermal continuum. Although our uncertainties on the spin are probably underestimated and require additional analysis for including systematic effects, the result obtained for the spin seems to exclude a non-spinning black hole. Clearly this preliminary statement has to be quantified and the analysis has to be extended to the three other observations of Cyg X-1 with similar quality and simultaneous *RXTE* coverage.

6.2 CONSTRAINING NEGATIVE SPIN

A main issue of this thesis was the phenomena of a negatively spinning black hole. Not only the resulting line profiles were presented, but the stability (King et al., 2005) and hints from AGN (Volonteri et al., 2005) and GBH (Brandt & Podsiadlowski, 1995) evolution give strong evidences for their existence and the necessity to consider negative spin (Dauser et al., 2010). We have shown that lines from counterrotating disks are narrower than those from Schwarzschild black holes, since the marginally stable orbit moves outwards as the black hole's angular momentum decreases. Since these lines still have a slightly asymmetric shape, they are still expected to be observable (see Sec. 3.4 and Dauser et al., 2010). Hence future observations should explicitly test for negative spin. Therefore we provided a new model for data analysis (Chap. 4). It was shown that our model has a more flexible scheme for the calculation of line profiles for black holes of all possible angular momenta and for arbitrary emissivity and limb-darkening laws, which has a significantly smaller footprint in terms of the amount of pre-calculation required. Comparison showed that its results are in agreement with the modern relativistic line model of Dovčiak et al. (2004).

6.3 BROAD EMISSION LINES AS A PROBE FOR BLACK HOLE SPIN

In conclusion, it was shown in this work that the predictive capabilities of broad emission features are enormous. It was shown that this method is in principle capable of measuring intrinsic parameters of the system like the spin of the black hole, the size of the accretion disk and the accretion geometry. Additionally, quantities like the inclination of the system can be inferred as well.

Because of the above reasons, the analysis of broad emission lines gives us deeper insight into the black hole system and not only allows to measure the spin. But as could be seen in Fig. 1.5, there are much less spin measurements with this method than by fitting the thermal

disk component (see Sec. 1.3.1). Nevertheless, the great advantage of line measurements is that the shape does not at all depend on the mass of the black hole, which is usually only roughly known. Moreover the broad emission line is always present at the same energy and therefore is in principle the same in GBH and AGN systems. Hence, with a more physically motivated modeling of the reflection features, similarities and differences between these two systems could be investigated.

Reducing the number of independently varying parameters would be a simple step towards a more successful modeling. For example the inclination can be estimated or at least limited by other observations, e.g., when eclipses are seen in the light curve. Most of the other parameters are not accessible directly by measurements, and may even reach unphysical values in data analysis. One example is the emissivity, which is assumed to be in the form of a phenomenological power law in all available models. Observations of MCG–6-30-15, e.g., lead to unphysically high emissivities (Wilms et al., 2001; Miniutti et al., 2007). Hence, either we do not understand the physical implications of the current model, or a different approach has to be chosen to parametrize the emissivity, ideally with more physical parameters. A step in this direction was already made in Sec. 5 for the jet-base geometry. There we have chosen a geometry and showed how the incident radiation onto the disk depends on the height of the primary source above the black hole. Assuming we know the connection between the incident and the reflected spectrum, e.g., by using the XSTAR-code (Kallman & McCray, 1982; Kallman & Bautista, 2001, see below), this allows us to parametrize the former unphysical emissivity by the height and the spectrum of the primary source. Additionally the spectrum of the hard X-ray source is thought to be in form of a power law (Sunyaev & Trümper, 1979) and therefore we are only left to determine the index. In case of a jet-base geometry, this index is connected to jet models (see, e.g., Markoff & Nowak, 2004; Markoff et al., 2005) and hence allows to find out more about the whole system and establish a connection to radio measurements.

Speaking of the connection between the incident and the reflected spectrum above brings us to another issue which requires a better physical description in the modeling process. In data analysis, like for the AGN MCG–6-30-15 (Tanaka et al., 1995; Wilms et al., 2001; Miniutti et al., 2007), mostly a single emission line with variable energy is chosen to describe this connection. While working well for AGN, this approach is usually more complicated in GBHs, as the accretion disk has a higher temperature and hence the ionization structure of the disk changes. An advanced approach can be chosen, by using models like *reflionx* (Ross et al., 1999; Ross & Fabian, 2005), which predict the reflected spectrum depending on the ionization of the disk. This can be convolved with relativistic line models like *relconv* (Dauser et al., 2010) to calculate the correct relativistic smearing. Still, in this approach the emissivity does not have any connection to the incident hard X-ray radiation either, although it is obvious that there has to exist a physical connection. In a rough estimate, an incident photon is able to induce the fluorescent emission of a $K\alpha$ photon, if its able to completely remove an electron from the K-shell of the atom. Hence its energy has to lie above the ionization energy of this electron, i.e., it has an energy higher than edge of the considered element. The Fe edge, e.g., is at 7.1 keV (Ross et al., 1996). Therefore the part of the incident spectrum above the edge in the rest frame of the disk gives an estimation of the reflected intensity and especially its radial dependence. Due to energy shifts close to the black hole, the incident spectrum can deviate strongly from the emitted spectrum, depending on the location and geometry of the hard X-ray source. As the line profiles show that the shape is very sensitive to the emissivity index, changes are good to get a better idea of the geometry of the system by analyzing this closer.

Although the above model offers a connection between the incident and the reflected emission, it still lacks an important physical process, as hard X-rays obviously influence the ion-

ization structure of the accretion disk. Therefore a proper modeling has to simulate the radial dependent effects induced by the incident photons. This could even serve to constrain the inner edge of the disk. As explained in Sec. 3.4, the inner edge of the disk probed by analyzing fluorescent emission features might not be the physical boundary of the accretion disk: If the inner regions are fully ionized, no electrons remain to produce fluorescent emission and therefore we would measure a larger effective inner radius of the accretion disk. Modeling the radial dependent ionization structure of the accretion disk would quantify this effect.

Summarizing the above thought implies that we need to do self-consistent calculations assuming a certain geometry (e.g., the lamp-post geometry) and then model the physics and simulate the observed spectrum. Only in this way are able to understand these systems, including components like the relation to the formation of relativistic jets.

6.4 A SELF-CONSISTENT MODEL

As motivated above, the great goal for analyzing broad emission lines is to construct a self-consistent model, which calculates the complete reflected spectrum of the accretion disk from the spectrum of the primary source, using physically motivated parameters of the system. In a first step this can be solved by using the irradiated spectrum on the disk, which can be readily simulated by the techniques presented in Chap. 5, and estimating the fluorescent emission by the fraction of the spectrum above the ionization edge of Fe $K\alpha$. The *relline* model could then simulate the observed spectrum, with the differences that the emissivity used in the model is not only a fitting parameter, but depends on the incident spectrum, which is a more physical quantity. Nevertheless, the accretion disk consists of several elements and therefore one would require a more thorough treatment for a real self-consistent model. This could be achieved by using the *XSTAR*-code (Kallman & McCray, 1982; Kallman & Bautista, 2001), which takes all ionization states from H to Si into account. Hence, the reflected spectrum can in principle be calculated from the incident radiation. The actual observed spectrum is then easily calculated by taking the light bending and energy shifts on the way the the observer into account, e.g., with the *relline*-code.

Being equipped with a better understanding of the system itself is crucial for constraining the source dependent parameters better. Hence, the systematic errors present in spin measurements could be reduced, which would decrease the apparent scatter in its values (see Fig. 1.5) and therefore increase the reliability of a single measurement. Furthermore, also the search for negatively spinning black holes is facilitated by smaller uncertainties. High signal to noise data for many AGN sources, which would be provided by future X-ray mission such as *IXO*, together with an analysis providing reasonable uncertainties, statistics of the spin of SMBH could be formulated. As there are already AGN with broad emission features found at high redshifts, the evolution of the spin with time could also be analyzed, which would allow to draw conclusions about galaxy evolution.

ACKNOWLEDGMENTS

At first, I would like to thank my supervisor Jörn Wilms for introducing me to the fascinating world of astronomy and astrophysics and for giving me the possibility to do my diploma thesis at the Remeis observatory. Moreover I owe him thanks for supporting me in traveling and connecting me with international scientists that work on similar subjects.

Secondly I want to thank everybody of the Remeis crew for making each day at the observatory so pleasant and letting me know that working is not the only reason to make the journey from Erlangen to Bamberg. Moreover my thanks go to the X-ray group, for inspiring me in my work in discussions in the weekly group-meeting or privately. I want to emphasize my colleagues in the office, Manfred Hanke and Moritz Böck, whom I thank for the nice atmosphere, many discussions and an endless amount of (more or less useful) ideas. Additionally I want to thank Refiz Duro for the joint work on the Cyg X-1 observation. One person who deserves special thanks is Manfred Hanke, who had always time to answer my endless questions and who is responsible for a great part of my knowledge about software like `slang/ISIS`, `Perl`, `GIT`, `LATEX` and `Ubuntu`.

For financial support necessary for traveling to international conferences, I want to thank the Leonardo Kolleg of the University Erlangen-Nuremberg and the European Commission under contract ITN 215212 "Black Hole Universe". Additionally I would like to thank the Max Weber-Programm Bayern for the ideological support, e.g. in form of a language course.

There are also people outside the observatory I would like to thank: First of all I owe thanks to my collaborators Christopher Reynolds and Laura Brenneman for new ideas and corrections concerning the publication about negatively spinning black holes that is also presented in this work. And I also want to thank Jiri Svoboda, Michal Dovčiak and Valdír Karas for fruitful discussions about relativistic iron lines during my stay in Prague. Moreover I would like to thank Roland Speith for writing a very nice Diploma thesis and a well documented code that allowed me to begin working in the field easily. And my thanks to John Davis for providing the `SLXfig` module, which was used to prepare the figures in this work.

Then I would like to thank people reading my thesis: Thanks to Moritz Böck and Cornelia Müller for helpful comments on part of the work and a lot of thanks to Julia Schmid and Manfred Hanke for thoroughly reading the complete thesis.

Last but not least I deeply want to thank my parents for supporting and encouraging me during my studies and this work.

LIST OF FIGURES

1.1	Artist's impression of a GBH and an AGN	5
1.2	Geometries for the hard X-ray source	6
1.3	Monte Carlo simulation of a reflected spectrum	7
1.4	Best signal to noise observations of broad emission lines	9
1.5	Compilation of published spin measurements	10
2.1	Surfaces in the Kerr geometry for $a = 0.99$ in the x - z - plane	15
2.2	Plot of the important surfaces in the Kerr metric	18
3.1	Drawing to clarify the volume of the phase space in GR	22
3.2	$2d$ -map of an accretion disk showing the energy shift of the photons	24
3.3	Drawing of a BH system to clarify the impact parameters α and β	25
3.4	Redshift image of the accretion disk with $\theta_o = 80^\circ$	28
3.5	$2d$ -map of emission angles of an accretion disk	29
3.6	Line profiles to understand the line formation	31
3.7	Line profiles for different spin with fixed $r_{in} = 9r_g$	33
3.8	Map of the difference in energy shift between $a = 0.998$ and $a = -0.998$	34
3.9	Broad emission lines for different spins with $r_{in} = r_{ms}$	35
3.10	Confidence contours for an <i>IXO</i> observation of MCG-6-30-15	36
3.11	Comparison of models with different θ_o	37
3.12	Popular line models for different α	38
4.1	Line profiles for different combinations of a , θ_o and α	41
4.2	Convolution of a reflected spectrum with <i>relconv</i> for different ionizations	42
4.3	Comparison of the <i>relline</i> model to other models	43
5.1	Drawing of the jet-base geometry	46
5.2	$2d$ -map of the q -parameter	48
5.3	Photon tracks from the primary source to the accretion disk	50
5.4	The incident intensity $I(r)$ for $h = 4.5r_g$	52
5.5	$2d$ -map of I_{kerr}/I_{flat}	53
5.6	Fit of I_{flat} to I_{kerr}	54
5.7	$2d$ -plot of the energy shift	55
5.8	$2d$ -map of the incident angle	56
6.1	Model and data of the full Cyg X-1 observation	58

REFERENCES

- Arnaud K.A., 1996, In: G. H. Jacoby & J. Barnes (ed.) *Astronomical Data Analysis Software and Systems V*, Vol. 101. Astronomical Society of the Pacific Conference Series, p.17
- Bardeen J.M., Press W.H., Teukolsky S.A., 1972, *ApJ* 178, 347
- Beckwith K., Done C., 2004, *MNRAS* 352, 353
- Begelman M.C., Volonteri M., Rees M.J., 2006, *MNRAS* 370, 289
- Blum J.L., Miller J.M., Fabian A.C., et al., 2009, *ApJ* 706, 60
- Bolton C.T., 1972, *Nat* 235, 271
- Bowyer S., Byram E.T., Chubb T.A., Friedman H., 1965, *Science* 147, 394
- Boyer R.H., Lindquist R.W., 1967, *Journal of Mathematical Physics* 8, 265
- Braes L.L.E., Miley G.K., 1971, *Nat* 232, 246
- Brandt N., Podsiadlowski P., 1995, *MNRAS* 274, 461
- Brenneman L.W., Reynolds C.S., 2006, *ApJ* 652, 1028
- Caballero-García M.D., Miller J.M., Díaz Trigo M., et al., 2009, *ApJ* 692, 1339
- Cackett E.M., Miller J.M., Bhattacharyya S., et al., 2008, *ApJ* 674, 415
- Cackett E.M., Miller J.M., Homan J., et al., 2009, *ApJ* 690, 1847
- Carroll S.M., 2004, *Spacetime and geometry. An introduction to general relativity*, Addison Wesley
- Carter B., 1968, *Phys. Rev.* 174, 1559
- Carter B., 1971, *Physical Review Letters* 26, 331
- Chandrasekhar S., 1983, *The mathematical theory of black holes*, Clarendon Press and Oxford Univ. Press
- Comastri A., Brusa M., Civano F., 2004, *MNRAS* 351, L9
- Corbel S., Fender R.P., Tzioumis A.K., et al., 2000, *A&A* 359, 251
- Corral A., Page M.J., Carrera F.J., et al., 2008, *A&A* 492, 71
- Cunningham C.T., 1975, *ApJ* 202, 788
- Cunningham J.M., Bardeen C.T., 1973, *ApJ* 183, 237
- Dauser T., Wilms J., Reynolds C.S., Brenneman L.W., 2010, *MNRAS* 409, 1534
- di Salvo T., D’Ai A., Iaria R., et al., 2009, *MNRAS* 398, 2022
- Dolan J.F., 1970, *Space Sci. Rev.* 10, 830
- Done C., Diaz Trigo M., 2010, *MNRAS* 407, 2287
- Dovčiak M., 2004, Ph.D. thesis, Charles University Prague, Institute of Theoretical Physics & Astronomical Institute
- Dovčiak M., Karas V., Yaqoob T., 2004, *ApJ Suppl.* 153, 205
- Duro R., Dauser T., Jörn W., 2011, *A&A* in prep.
- Egron E., Di Salvo T., Burderi L., et al., 2011, *A&A* submitted
- Einstein A., 1916, *Annalen der Physik* 354, 769
- Einstein A., 1936, *Science* 84, 506
- Fabian A.C., Rees M.J., Stella L., White N.E., 1989, *MNRAS* 238, 729
- Fabian A.C., Sanders J.S., Etori S., et al., 2000, *MNRAS* 318, L65
- Fabian A.C., Zoghbi A., Ross R.R., et al., 2009, *Nat* 459, 540
- Falcke H., Melia F., Agol E., 2000, *Astrophys. J., Lett.* 528, L13
- Fender R.P., Gallo E., Russell D., 2010, *MNRAS* 406, 1425
- Ferrarese L., Merritt D., 2000, *Astrophys. J., Lett.* 539, L9
- Frank J., King A., Raine D.J., 2002, *Accretion Power in Astrophysics*, Cambridge, UK: Cambridge University Press
- Garofalo D., 2009, *ApJ* 699, 400
- Garofalo D., Evans D.A., Sambruna R.M., 2010, *MNRAS* 406, 975
- Giacconi R., Murray S., Gursky H., et al., 1972, *ApJ* 178, 281
- Haardt F., 1993, *ApJ* 413, 680
- Hanke M., Wilms J., Nowak M.A., et al., 2009, *ApJ* 690, 330
- Hjellming R.M., Wade C.M., 1971, *Astrophys. J., Lett.* 168, L21
- Hollywood J.M., Melia F., 1997, *ApJS* 112, 423
- Houck J.C., Denicola L.A., 2000, In: Manset N., Veillet C., Crabtree D. (eds.) *Astronomical Data Analysis Software and Systems IX*. ASP Conf. Ser. 216, p. 591
- Iwasawa K., Miniutti G., Fabian A.C., 2004, *MNRAS* 355, 1073
- Jaroszynski M., 1997, *Acta Astronomica* 47, 399
- Kallman T., Bautista M., 2001, *ApJS* 133, 221

- Kallman T.R., McCray R., 1982, *ApJS* 50, 263
- Kataoka J., Reeves J.N., Iwasawa K., et al., 2007, *PASJ* 59, 279
- Kendziorra E., Wilms J., Haberl F., et al., 2004, In: G. Hasinger & M. J. L. Turner (ed.) *Society of Photo-Optical Instrumentation Engineers (SPIE) Conference Series*, Vol. 5488. Presented at the Society of Photo-Optical Instrumentation Engineers (SPIE) Conference, p.613
- Kerr R.P., 1963, *Phys. Rev. Lett.* 11, 237
- King A.R., Lubow S.H., Ogilvie G.I., Pringle J.E., 2005, *MNRAS* 363, 49
- King A.R., Pringle J.E., Hofmann J.A., 2008, *MNRAS* 385, 1621
- Krolik J.H., 1999, *Active galactic nuclei: from the central black hole to the galactic environment*, Princeton Univ. Press, Princeton
- Laor A., 1991, *ApJ* 376, 90
- Longinotti A.L., de La Calle I., Bianchi S., et al., 2008, *Memorie della Societa Astronomica Italiana* 79, 259
- Luminet J., 1979, *A&A* 75, 228
- Maitra D., Markoff S., Brocksopp C., et al., 2009, *MNRAS* 398, 1638
- Markoff S., Nowak M.A., 2004, *ApJ* 609, 972
- Markoff S., Nowak M.A., Wilms J., 2005, *ApJ* 635, 1203
- Martocchia A., Karas V., Matt G., 2000, *MNRAS* 312, 817
- Martocchia A., Matt G., 1996, *MNRAS* 282, L53
- Martocchia A., Matt G., Karas V., 2002a, *A&A* 383, L23
- Martocchia A., Matt G., Karas V., et al., 2002b, *A&A* 387, 215
- McClintock J.E., Narayan R., Gou L., et al., 2010, In: *AIP Conf. Series*, Editors: A. Comastri, L. Angelini, & M. Cappi, Vol. 1248., p.101
- McClintock J.E., Shafee R., Narayan R., et al., 2006, *ApJ* 652, 518
- Miller J.M., 2007, *Annual Review of Astronomy & Astrophysics* 45, 441
- Miller J.M., Fabian A.C., Reynolds C.S., et al., 2004, *ApJ* 606, L131
- Miller J.M., Fabian A.C., Wijnands R., et al., 2002, *ApJ* 578, 348
- Miller J.M., Reynolds C.S., Fabian A.C., et al., 2009, *ApJ* 697, 900
- Miniutti G., 2006, *Astronomische Nachrichten* 327, 969
- Miniutti G., Fabian A.C., 2004, *MNRAS* 349, 1435
- Miniutti G., Fabian A.C., Anabuki N., et al., 2007, *PASJ* 59, 315
- Miniutti G., Fabian A.C., Goyder R., Lasenby A.N., 2003, *MNRAS* 344, L22
- Misner C.W., Thorne K.S., Wheeler J.A., 1973, *Gravitation*, W.H. Freeman and Co.
- Murdin P., Webster B.L., 1971, *Nat* 233
- Nandra K., O'Neill P.M., George I.M., Reeves J.N., 2007, *MNRAS* 382, 194
- Ninkov Z., Walker G.A.H., Yang S., 1987, *ApJ* 321, 425
- Novikov I.D., Thorne K.S., 1973, *Astrophysics of black holes.*, Gordon and Breach: Paris
- Oda M., Gorenstein P., Gursky H., et al., 1971, *Astrophys. J., Lett.* 166, L1
- Rees M.J., 1984, *ARA&A* 22, 471
- Reeves J.N., Fabian A.C., Kataoka J., et al., 2006, *Astronomische Nachrichten* 327, 1079
- Remillard R.A., McClintock J.E., 2006, *ARA&A* 44, 49
- Reynolds C.S., 1996, Ph.D. Thesis, University of Cambridge
- Reynolds C.S., Fabian A.C., 2008, *ApJ* 675, 1048
- Reynolds C.S., Garofalo D., Begelman M.C., 2006, *ApJ* 651, 1023
- Reynolds C.S., Nowak M.A., 2003, *Phys. Rep.* 377, 389
- Richards G.T., Strauss M.A., Fan X., et al., 2006, *AJ* 131
- Riffert H., Herold H., 1995, *ApJ* 450, 508
- Ross R.R., Fabian A.C., 2005, *MNRAS* 358, 211
- Ross R.R., Fabian A.C., 2007, *MNRAS* 381, 1697
- Ross R.R., Fabian A.C., Brandt W.N., 1996, *MNRAS* 278, 1082
- Ross R.R., Fabian A.C., Young A.J., 1999, *MNRAS* 306, 461
- Schnittman J.D., 2006, *ArXiv Astrophysics e-prints*
- Schwarzschild K., 1916, *Abh. Konigl. Preuss. Akad. Wissenschaften Jahre 1906,92*, Berlin, 1907 189–196
- Shakura N.I., Sunyaev R.A., 1973, *A&A* 24, 337
- Shaposhnikov N., Titarchuk L., Laurent P., 2009, *ApJ* 699, 1223
- Shipman H.L., 1975, *Astrophysical Letters* 16, 9
- Speith R., Riffert H., Ruder H., 1995, *Computer Physics Communications* 88, 109
- Springel V., White S.D.M., Jenkins A., et al., 2005, *Nat* 435, 629
- Streblyanska A., Hasinger G., Finoguenov A., et al., 2005, *A&A* 432, 395
- Sunyaev R.A., Trümper J., 1979, *Nat* 279, 506
- Svoboda J., Dovčiak M., Goosmann R., Karas V., 2009a, *A&A* 507, 1
- Svoboda J., Dovčiak M., Goosmann R.W., Karas V., 2009b, *ArXiv e-prints*
- Tanaka Y., Nandra K., Fabian A.C., et al., 1995, *Nat* 375, 659

References

- Thorne K.S., 1974, *ApJ* 191, 507
Titarchuk L., Hua X., 1995, *ApJ* 452, 226
Torrejón J.M., Schulz N.S., Nowak M.A., Kallman T.R., 2010, *ApJ* 715, 947
Vaughan S., Fabian A.C., 2004, *MNRAS* 348, 1415
Volonteri M., Madau P., Quataert E., Rees M.J., 2005, *ApJ* 620, 69
Webster B.L., Murdin P., 1972, *Nat* 235, 37
Wilms J., Kendziorra E., Nowak M.A., et al., 2006, In: A. Wilson (ed.) *The X-ray Universe 2005*, Vol. 604. ESA Special Publication, p.217
Wilms J., Pottschmidt K., Pooley G.G., et al., 2007, *Astrophys. J., Lett.* 663, L97
Wilms J., Reynolds C.S., Begelman M.C., et al., 2001, *MNRAS* 328, L27
Wise M.W., McNamara B.R., Nulsen P.E.J., et al., 2007, *ApJ* 659, 1153
Yamada S., Makishima K., Uehara Y., et al., 2009, *ApJ* 707, L109
Zeldovich Y.B., Novikov I.D., 1971, *Relativistic astrophysics. Vol.1: Stars and relativity*, Chicago: University of Chicago Press

DECLARATION

Hiermit erkläre ich, dass ich die Arbeit selbstständig angefertigt und keine anderen als die angegebenen Hilfsmittel verwendet habe.

Bamberg, 20.12.2010

Thomas Dauser